2006

Velocity-pressure coupling in finite difference formulations for the Navier-Stokes equations

Bashar Zogheib
University of Windsor

VELOCITY-PRESSURE COUPLING IN FINITE DIFFERENCE FORMULATIONS FOR THE NAVIER-STOKES EQUATIONS

by
Bashar Zogheib

A Dissertation
Submitted to the Faculty of Graduate Studies and Research
through Mathematics
in Partial Fulfillment of the Requirement for the
Degree of Doctor of Philosophy
at the University of Windsor

Windsor, Ontario, Canada
2006

Your file Votre référence
ISBN: 978-0-494-17134-9
Our file Notre référence
ISBN: 978-0-494-17134-9

Abstract

A new numerical algorithm for solving the two-dimensional, steady, incompressible, laminar, viscous flow equations on a staggered grid is presented in this thesis. The proposed methodology is finite difference based, but essentially takes advantage of the best features of two well-established numerical formulations, the finite difference and finite volume methods. Some weaknesses of the finite difference approach are removed by exploiting the strengths of the finite volume method. In particular, the issue of velocity-pressure coupling is dealt with in the proposed finite difference formulation by developing a new pressure correction equation in a manner similar to the SIMPLE (Semi-Implicit Method for Pressure Linked Equations) approach commonly used in finite volume formulations. However, since this is purely a finite difference formulation, numerical approximation of fluxes is not required. Results obtained from the present method are based on the first-order upwind differencing scheme for the convective terms, but the methodology can easily be modified to accommodate higher order differencing schemes. Comparison with exact solutions for flow in a straight duct is made. The new formulation is also validated against experimental and other numerical data for well-known benchmark problems, namely the lid-driven cavity and backward-facing step flows. For curvilinear domains, the proposed method is validated against numerical results for a complex channel flow and compared to experimental results for the flow over a scour hole. For further validation, some of the results from the present method are compared to results obtained by FLUENT.

ACKNOWLEDGEMENTS

I would like to deeply thank my supervisor, Dr. R.M. Barron who was my inspiration for this project. Thank you for your encouragement and support.

I would also like to extend my very special thanks to Dr. O. Chandna for all his support.

I extend my deepest gratitude to Dr. N. Zamani, Dr. R. Balachandar, Dr. S. Kocabiyik and Dr. L. Corkum who kindly agreed to be in my committee.

Special thanks to Dr. Ahmed, the Head of the Department, and to the staff, (Dina, Christine and Marija).

I would like to thank Prof. Z. Zhang for his help with FLUENT.

I would also like to acknowledge my parents' contribution to my academic success. Their confidence in my privileged education has been central to my ability to pursue graduate studies. I owe them a lot of gratitude for their unwavering faith in my ability.

Lots of thanks to my sisters, Hanadi and Elham; my brothers, Salah, Alaa, and Hamoudi; my brother-in-law, Ali. They never once questioned the fact that they were there to lift me up when my load became too heavy.

TABLE OF CONTENTS

LIST OF TABLES

LIST OF FIGURES

NOMENCLATURE

u, v	velocity components
p	pressure
ρ	density
x, y	Cartesian coordinates
υ	kinematic viscosity
dx, dy	differential element in Cartesian coordinates
Δx , Δy	increments in Cartesian coordinates
P, Q	control functions for grid generation
ξ , η	curvilinear coordinates
J	transformation Jacobian
D	channel width
Re	Reynolds number
c	constant pressure gradient
I, J	maximum number of nodes
h	step height
L	length of backward-facing step channel
ω	vorticity
$\Delta\xi$, $\Delta\eta$	increments in curvilinear coordinates
τ	artificial compressibility
a	pseudo-speed of sound
S	source term

Subscripts

i, j	coordinate indices, grid point indices
P	value at a calculation point
E	value at the east side of P
W	value at the west side of P
N	value at the north side of P
S	value at the south side of P

nb	value at neighbour nodes
u	terms in the *u*-momentum equation
v	terms in the *v*-momentum equation
old	previous iteration
new	new value

Superscripts

*	iterated values
'	corrected values
int	coefficients at interior nodes
S	coefficients near south boundary
N	coefficients near north boundary
E	coefficients near east boundary
W	coefficients near west boundary

CHAPTER I

INTRODUCTION AND LITERATURE REVIEW

1.1 Introduction

Generally speaking, incompressible fluid flow equations may be expressed in two different formulations based on the dependent variables used. First is the primitive variable formulation, in which the equations of motion are expressed in terms of the pressure and velocity. The second form of the equations is the so-called vorticity-streamfunction formulation, which is derived from the Navier-Stokes equations by incorporating the definitions for the vorticity and streamfunction.

There are many papers devoted to the numerical solution of the incompressible Navier-Stokes equations. While there are finite difference, finite element and finite volume methods available, most of the important research work in this field has been based on the finite volume methodology. The popularity of the finite volume approach is evidenced by the fact that most commercial Computational Fluid Dynamics (CFD) codes, such as STARCD and FLUENT, are based on finite volume formulations.

Since this thesis is based on a finite difference formulation and the primary objective is to exploit the advantages of the finite volume SIMPLE (Semi-Implicit Method for Pressure Linked Equations) algorithm within a finite difference context, the literature review will concentrate only on finite volume and finite difference formulations.

1.2 Vorticity-Streamfunction Formulation

In the earliest work on solutions of the two-dimensional Navier-Stokes equations, many of the solution techniques were based on the use of the vorticity and the streamfunction as the dependent variables.

The vorticity-streamfunction formulation has the major advantages of avoiding the explicit appearance of the pressure and not having to solve the continuity equation directly. One of the major reasons for the success of the above formulation in predicting both steady and unsteady incompressible flow fields is that, by definition, the continuity equation is satisfied identically for all values of streamfunction, as mentioned by Currie [1]. Furthermore, the pressure is eliminated by an appropriate combination of the differentiation of the momentum equations, so the velocity field can be determined without having to calculate the pressure field.

For incompressible flows, the streamfunction and vorticity equations can be derived for either steady or unsteady flows. In this thesis we only deal with steady incompressible laminar flows. However, from a CFD perspective, steady flows can be computed as the steady-state limit of an unsteady flow simulation. In this case, the unsteady flow equations are marched in time until the solution becomes time-invariant. In fact, such an unsteady method is akin to an iterative solution of the steady flow equations in which each iteration is analogous to a time step. A pioneering work in the category of unsteady methods applied to the vorticity-streamfunction formulation is the one developed at Imperial College in the late 1960's, as described by Gosman et al [2]. Other important works are those of Briley [3], Bozeman and Dalton [4], Napolitano and Walters [5] and Osswald et al [6]. Gosman et al [2] used a segregated approach, where the vorticity

transport equation was solved separately from the Poisson equation for the streamfunction. Osswald et al [6] also used a segregated approach but adopted the Strongly Implicit Procedure of Stone [7] for solving the vorticity equation, together with a block Gaussian elimination technique, as described by Ghia et al [8], for the streamfunction equation, as opposed to the simple point Gauss-Siedel method used by Gosman et al [2]. Napolitano and Walters [5] used a linearized block-ADI method for the simultaneous solution of the vorticity and streamfunction equations.

There are, however, a number of serious difficulties encountered when solving the equations in the vorticity-streamfunction formulation. Aside from the fact that these coupled equations are non-linear, one of the major difficulties is that the values of vorticity on no-slip boundaries and at outlets are not known a priori, while these values are needed to solve the discretized problem. While it is possible to overcome most of the difficulties, perhaps the most damaging restriction is that it is awkward to define the streamfunctions for three-dimensional flows, and there are three components of vorticity. Thus vorticity-streamfunction analyses are essentially limited to two-dimensional flows.

As indicated earlier, the pressure is eliminated as a variable in the vorticity-streamfunction formulation. If the pressure field is required, an equation for pressure must be obtained and solved subject to appropriate boundary conditions. The usual approach is to derive a Poisson equation for pressure by summing the x-derivative of the u-momentum equation and the y-derivative of the v-momentum equation. The right hand side of the pressure equation is expressed in terms of velocity components, which are known from the solution of the vorticity and streamfunction equations. As a mathematical problem, the Poisson equation for pressure is an elliptic partial differential

equation defined on a bounded domain. For the problem to be well-posed, a set of boundary conditions must be imposed on the entire boundary of the domain. For most fluid flow problems, physical boundary conditions for pressure are not available. Hence, it is common practice to introduce numerical boundary conditions, such as using the momentum equations to specify derivatives of pressure normal to boundaries. These numerical boundary conditions can lead to instabilities and additional loss of accuracy in the solution.

1.3 Primitive Variable Formulation

Since the early 1970's there has been a noticeable shift of interest from the vorticity-streamfunction formulations of the incompressible Navier-Stokes equation to the primitive variables u, v, p formulations.

The main difficulty with the primitive variable formulation for incompressible flows is that, even though there are three equations for the three unknowns u, v, p, there is no explicit equation which can be used for pressure. The usual procedure followed by most researchers is to treat the u-momentum equation as an elliptic equation for u and the v-momentum equation as an elliptic equation for v. These non-linear equations are coupled, and must be solved simultaneously, or iteratively using a segregated solver. The main problem lies in the determination of pressure which, in a sense, is only weakly coupled to the velocity, through the pressure gradients in the momentum equations. During the solution process, these pressure gradients are treated as known source terms in the momentum equations, having been computed from some appropriate pressure equation.

One of the primary distinctions between finite difference and finite volume approaches lies in the methods used to determine the pressure field, i.e., the treatment of the velocity-pressure coupling problem. These methods are discussed in the next two sections.

1.3.1 Finite Difference Formulation

Finite difference primitive variable formulations have been used with success by different researchers such as Chorin [9] and Kim and Moin [10]. Generally speaking, for finite difference formulations, two procedures have been developed for this purpose. The first is to derive a Poisson equation for pressure, similar to that used in vorticity-streamfunction formulations. This is achieved by differentiating the u-momentum equation with respect to x, the v-momentum with respect to y and summing the results. However, the continuity equation is still not explicitly satisfied if a primitive variable formulation is retained. This equation serves as a constraint on the velocity field, and some additional numerical "tricks" must be introduced to ensure conservation of mass [11]. A serious disadvantage of this approach is the complexities associated with approximating the Laplacian operator near a boundary. In particular, the pressure outside the domain may be needed to calculate pressure one grid line inside the boundaries. In general, no physical specification of pressure exists so, as in vorticity-streamfunction formulations, the boundary conditions employed in numerical simulations are usually Neumann-type, in this case obtained from the momentum equations.

The second approach is the introduction of artificial compressibility into the continuity equation, as suggested by Chorin [12]. This approach is outlined in Chapter 2.

For the case of the incompressible Navier-Stokes equations written in primitive variable formulation, the steady-state solution can be obtained either by taking an unsteady

solution to the limit of large time, or by "directly" solving the steady equations. Unsteady methods devised to compute steady flows include the work of Chorin [12] and the fractional step method of Kim and Moin [10]. The fractional step method is a two step method. In the first step velocity is calculated from the momentum equation without a pressure gradient. In this step only discretization of time is considered. In the next step, velocity is corrected by using the pressure gradient and the transient term. From this equation a Poisson equation for pressure is derived. The resulting pressure is then used to correct the velocity. Even though these algorithms have shown sufficient accuracy and efficiency, the main body of recent work has been in the development of methods for the solution of the steady-state equations directly. In general, steady methods for the primitive variable formulation solve the governing equations using some form of a relaxation solution algorithm.

1.3.2 Finite Volume Formulation

Patankar and Spalding [13] solved the parabolized Navier-Stokes equations using a finite volume approach. The most significant contribution of their research was the development of the SIMPLE (Semi-Implicit Method for Pressure Linked Equations) algorithm to resolve the velocity-pressure coupling problem. This algorithm and subsequent modifications have become the standard in CFD community. The first widely used finite volume scheme for the steady incompressible Navier-Stokes equations was the one introduced by Caretto et al [14], based on the SIMPLE algorithm. The work of Caretto et al [14] was a milestone in that it resulted in the production of computer codes which allowed for the solution of the equations in primitive variable form for many

practical problems without the necessity of rewriting the computer code for each new problem.

The SIMPLE algorithm [15] uses a segregated solution technique in which the pressure field and velocity fields are solved for separately within an iteration cycle (i.e. a complete sweep of the flow field). The necessary pressure-velocity coupling for the satisfaction of mass conservation is attained through the solution of a pressure correction equation, derived from the finite volume discretization of the continuity equation by means of certain simplifying assumptions. A new algorithm was later introduced by Patankar [15], called SIMPLER. SIMPLER uses a more accurate pressure correction equation and the velocity field is guessed initially instead of the pressure field. This new procedure reduced the level of under-relaxation required, resulting in an increased convergence rate and, consequently, in less computer time. This improvement was carried further by variations of SIMPLER, like SIMPLEC, SIMPLEX and FIMOSE. The major difference among all these different algorithms is in the way the pressure-velocity coupling is achieved. (For an evaluation of these different algorithms, see the papers of Van Doormaal and Raithby [16] and Latimer and Pollard [17].) All the above algorithms require the determination of optimum relaxation factors in order to attain an optimal convergence rate.

A wealth of different pressure-velocity coupling algorithms were developed in the wake of the relative success of the SIMPLE procedure. All of these algorithms use a finite volume discretization procedure and a segregated solution technique, but differ in the often arbitrary way that the velocity and pressure fields are corrected in order to satisfy mass conservation. This class of solutions is typified by investigations such as the works

of Raithby and Schneider [18], Briley [19], and Pratap and Spalding [20]. Raithby and Schneider [18] proposed a scheme that does not require the solution of a second correcting equation for the pressure, as required by SIMPLER. It is referred to as the PUMPIN method and is based on averaging the pressures obtained by integrating the momentum equations between a reference point and each point in the grid, along several different paths.

Most of the research works mentioned above used a staggered grid arrangement to prevent the checkerboard problem [21]. Thiart [22], Miller and Schmidt [23] and Barton and Kirby [24] solved the flow equations on a non-staggered or colocated grid. Thiart [22] prevented the pressure checkerboarding through a differencing scheme that incorporated the influence of pressure on velocity gradients. Barton and Kirby [24] prevented it by applying fourth-order dissipation to the pressure field. The methods of Thiart [22] and Barton and Kirby [24] were implemented in a SIMPLE type algorithm. Miller and Schmidt [23] used a pressure weighted interpolation method for the solution of the equations and his method was implemented in a SIMPLEC type algorithm. Peric et al [25] presented a comparison of two finite volume solution methods for two-dimensional incompressible fluid flows, one with staggered and the other with colocated grids. They concluded that the computational effort and accuracy are almost identical for both solution methods.

Karki and Patankar [26] and Shyy et al [27] investigated solutions for the flow equations on curvilinear grids. Karki and Patankar [26] developed a finite volume scheme for a generalized nonorthogonal coordinate system with a staggered grid. They selected the physical covariant velocity components to be the dependent variables in the momentum

equations and coupled velocity and pressure by using the SIMPLER algorithm. Shyy et al [27] developed a similar finite volume scheme where coupling is effected using the SIMPLE algorithm. Reggio and Camarero [28] solved the equations in an arbitrary domain using a non-staggered grid. Peric [29] analyzed the effect of reducing the computational stencil obtained in curvilinear domains, from a 9-point computational stencil in a two-dimensional case to 5 or 7 points.

The finite volume method is relatively easy to implement in rectangular domains because the fluxes across cell faces can be calculated with very little effort. The main advantage of the finite volume method is that it can be used on an unstructured mesh. However, all finite volume formulations require flux calculations, and it is difficult to calculate the fluxes across irregular faces of the mesh. Also, the finite volume approach requires more approximations of the original flow equations. In particular, the approximation of integrals over a control volume is not required in a finite difference formulation. It may also be difficult to apply the boundary conditions on irregular boundaries.

1.4 Differencing Schemes

Beyond the pressure-velocity coupling, another source of differences among various algorithms for segregated solution techniques is in the treatment of the derivatives of the convective terms. The diffusion term contains second order derivatives, and the second order central differencing scheme is most appropriate to discretize this term. However, because convection has an inseparable connection with diffusion, the diffusion and convection terms should be handled as one unit. The discretization of the convection-diffusion terms is one of the major difficulties in numerical solutions of the governing equations for fluid flow and heat transfer.

Many discretization schemes for convection-diffusion equations have been proposed and studied. In this chapter, only a few main schemes are reviewed. A natural idea for discretization of the convection and diffusion terms is to use the second order central difference scheme for both. However, the numerical results will be unrealistic if any coefficient in the discretized equation is negative, and the other coefficients are positive. It is well-known that the second order central difference scheme is prone to oscillations if the cell Reynolds number exceeds 2. According to Shyy et al [30], this generally accepted critical cell Reynolds number for the central difference scheme may not be a reliable indicator of the performance of this scheme. Oscillations in the solution, which are expected while using this scheme for high cell Reynolds numbers, may not occur.

One proposed remedy for the difficulty encountered with the second order central difference scheme is to apply a first order upwind difference scheme. The basic idea of this scheme is that the discretization of the diffusion term is left unchanged, but the convection term is discretized based on the assumption that the value of the dependent variable at the nodal point of interest depends on the value of the dependent variable at the point on the upwind side of the cell face only [21]. One of this scheme's shortcomings is that its truncation error order is relatively low, i.e., of first order. The diffusion term is calculated from a linear profile and thus overestimates diffusion at high Peclet numbers (ratio of the strengths of convection and diffusion). The hybrid scheme has been put forward to overcome these difficulties. This scheme combines the merits of the central difference scheme and the first order upwind scheme, and avoids their defects [15]. It is identical with the central difference scheme for the Peclet number range between -2 and

2. Outside this range it reduces to the first order upwind scheme in which the diffusion is set equal to zero.

Methods for testing a differencing scheme should be mentioned here. Usually, in order to test a scheme, a steady one-dimensional situation is considered in which only the convection and diffusion terms are present. The governing equation reduces to a second order ordinary differential equation, which has an exact solution provided the boundary conditions at the two ends of the domain (interval) are given. It has been found that the departure of the hybrid scheme from the exact solution in the one-dimensional case is rather large at Peclet number of ± 2. Also, it is premature to set the diffusion effects equal to zero as soon as the absolute value of the cell Reynolds number exceeds 2. A better approximation to the exact solution is given by the power-law scheme. It is more complicated than the hybrid scheme, but is not particularly expensive to compute. The hybrid scheme and the power-law scheme are now widely used in solving practical problems of fluid flow and heat transfer. In some cases, even the first order upwind scheme behaves not too badly if the grid is fine enough. As a matter of fact, the scheme closest to the exact solution for the one-dimensional case is the exponential scheme. When it is used for the steady one-dimensional problem, this scheme is guaranteed to produce the exact solution for any number of grid points. Nevertheless, this scheme is not widely used because (1) exponential functions are expensive to compute, and (2) the scheme will not produce the exact solutions for two- or three-dimensional situations, equations with non-zero sources, etc. The extra expense of computing exponentials does not seem to be justified and the exponential scheme behaves well only for a constant source term. For non-constant source terms, Wong and Raithby [31] proposed a

correction to the exponential scheme, referred to as the Locally Analytic Differencing Scheme (LOADS). Although the expressions for the LOADS are more complex, the error from the source terms is reduced and the accuracy of the results is greatly improved.

Another alternative to the first order upwind differencing scheme is to use a second order upwind differencing scheme. Unlike the first order upwind scheme, the value in the second order upwind scheme at a node depends on the values at two upstream nodes rather than just the value at one node. This scheme can be shown to have second order accuracy. The Skew Upstream Differencing Scheme (SUDS) [32] and the quadratic upstream differencing scheme (its full name is Quadratic Upwind Interpolation of Convective Kinematics, or QUICK) [33] have been suggested as alternates to the first order differencing scheme. In the SUDS, either the first order upwind differencing or the hybrid scheme is used, but it is applied along the skewed streamline passing through the cell face (interface). Thus, upwinding is used in a vector sense rather than along the resolved flow directions. The SUDS is useful when both convection and diffusion are primarily responsible for the spatial distribution of the dependent variable. In the QUICK scheme, instead of using linear interpolation for the convection terms as used in standard one-sided differencing schemes, a three-point upstream weighted quadratic interpolation is used. This scheme has the desirable property of high accuracy (third order spatial truncation error) and is based on a conservative control volume integral formulation. However, the QUICK scheme has also been found to be less stable than the upwind and hybrid schemes because it can occasionally generate both negative and positive influence coefficients. Pollard and Siu [34] developed a new form of the QUICK scheme called QUICKER (QUICK Extended and Revised). In the QUICKER scheme, the influence

coefficients are rearranged in such a way that they are always positive and the source terms are revised to avoid the negative value of the denominator in the discretized equation.

Although they have several attractive properties, both the QUICK and QUICKER schemes produce unphysical overshoots and a few oscillations for highly convective simulation of step profiles. To overcome this difficulty, Leonard [35] proposed the SHARP (Simple High-Accuracy Resolution Program) scheme which is based on an explicit, conservative, control volume flux formulation. In the SHARP scheme, the convective flux is modified by expressing the normalized convective flux value on a control volume face as a function of the normalized adjacent upstream node value. This results in a non-linear functional relationship between the normalized variables, whereas standard methods are all linear in this sense.

1.5 Present Work

1.5.1 Introduction

In CFD, finite difference methods begin with the differential equation form of the Navier-Stokes equations, while an integral form is used for finite volume methods. Nevertheless, these two approaches exhibit some common features. For example, both methods ultimately lead to a set of finite difference equations and, for both methods, there is no explicit equation for pressure. Generally speaking, the two methods depart from one another in the procedures devised to couple the velocity and pressure. Also, since this is purely a finite difference formulation, numerical approximation of fluxes is not required, thereby removing the difficulty of calculating fluxes associated with finite volume formulations. This is especially advantageous when the flow domain is non-rectangular

and fluxes must be calculated across highly skewed cell faces. Furthermore, an approximation for integrals and derivatives is needed in the finite volume method, while in the proposed method only an approximation for derivatives is needed.

The proposed method is a fundamental new approach to solving the incompressible Navier-Stokes equations that relies on the basic concepts of finite differences.

1.5.2 Objectives of the Present Work

This thesis proposes a new numerical method for solving the two-dimensional, steady, incompressible, laminar, viscous flow equations on a staggered grid. The primary objective of this study is to develop and implement the proposed procedure so as to establish confidence in its ability to calculate a wide range of fluid flows, rather than attempting to solve a few complicated individual flow problems. In this thesis, no attempt will be made to achieve high accuracy, or to optimize the solution algorithm.

1.5.3 Organization of the Present Work

In Chapter II, the flow equations are derived on a Cartesian mesh, the velocity-pressure coupling is explained and the pressure correction equation is analyzed. In Chapter III three benchmark applications are considered. In Chapter IV, the equations and procedure are formulated on a general nonorthogonal curvilinear mesh and in Chapter V the method is applied to three flow problems to validate the suitability of the proposed method.

CHAPTER II

DISCRETIZED FLOW EQUATIONS ON A STAGGERED CARTESIAN GRID

2.1 Introduction

The Navier-Stokes equations for two-dimensional, steady, incompressible, viscous flow in terms of Cartesian coordinates, in the non-conservative dimensional form, are

$$u_x + v_y = 0 \tag{2.1}$$

$$\begin{aligned} uu_x + vu_y + \frac{1}{\rho} p_x &= \upsilon(u_{xx} + u_{yy}) \\ uv_x + vv_y + \frac{1}{\rho} p_y &= \upsilon(v_{xx} + v_{yy}) \end{aligned} \tag{2.2}$$

where u and v are velocity components in the x and y directions respectively, p is the pressure, ρ is the constant density and υ is the viscosity.

The system of equations (2.1) and (2.2) is classified as elliptic, and the unknowns in these equations are velocity and pressure. The numerical solution of this set of equations is hindered by the fact that there is no direct link for the pressure between the continuity and momentum equations. To establish a connection some mathematical manipulations must be introduced. Generally speaking, for finite difference formulations, two procedures have been developed for this purpose. The first is to derive a Poisson equation for pressure. This is achieved by differentiating the u-momentum equation with respect to x, the v-momentum with respect to y and summing the results. However, the continuity equation is still not explicitly satisfied if a primitive variable formulation is retained, and some additional numerical "tricks" are usually introduced to ensure conservation of mass [11]. A serious disadvantageous of this approach is that pressure outside the domain is

needed to calculate pressure one grid line off the boundaries. However, in general, no physical specification of pressure exists. Boundary conditions for pressure employed in numerical simulations are usually Neumann-type, obtained from the momentum equations. The second approach is the introduction of artificial compressibility into the continuity equation, as suggested by Chorin [12]. He modified the continuity equation by introducing a time-dependent term. The continuity equation becomes

$$\frac{\partial p}{\partial t}+\frac{1}{\tau}\left(\frac{\partial u}{\partial x}+\frac{\partial v}{\partial y}\right)=0$$

where τ is the artificial compressibility of the fluid. Using the "equation of state", the compressibility can be related to a pseudo-speed of sound and to artificial density by the relations $\tau=\frac{1}{a^2}$ and $a^2=\frac{p}{\rho}$.

Thus, in Chorin's approach, the steady incompressible Navier-Stokes equations are expressed in a pseudo-transient non-dimensional form as

$$\frac{\partial p}{\partial t}+a^2\left(\frac{\partial u}{\partial x}+\frac{\partial v}{\partial y}\right)=0$$

$$\frac{\partial u}{\partial t}+\frac{\partial}{\partial x}\left(u^2+p\right)+\frac{\partial}{\partial y}(uv)=\frac{1}{\mathrm{Re}}\left(u_{xx}+u_{yy}\right)$$

$$\frac{\partial v}{\partial t}+\frac{\partial}{\partial y}\left(v^2+p\right)+\frac{\partial}{\partial x}(uv)=\frac{1}{\mathrm{Re}}\left(v_{xx}+v_{yy}\right)$$

where *Re* is the Reynolds number, defined as $\frac{UL}{\upsilon}$.

In Chorin's procedure, an artificial viscosity (damping terms) must be added to the discretized equations to overcome any possible instability in the solution.

Another way to deal with pressure is to express the Navier-Stokes equations in terms of the vorticity and streamfunction. In this formulation, the system is composed of the vorticity transport equation and the streamfunction equation. One of the advantages of this formulation is that the pressure term does not appear explicitly in either of the equations. Therefore, the system of equations is solved to provide the velocity field. If the pressure field is required as well, then the Poisson equation for the pressure is subsequently solved. A major disadvantage of this formulation is the specification of the boundary conditions on the vorticity, due to the lack of physical boundary conditions for vorticity. Therefore, numerical boundary conditions for the vorticity must be derived. Moreover, it is awkward to define the streamfunctions for three-dimensional flows, and there are three components of vorticity, thus essentially limiting the analysis to two-dimensional flows.

In this thesis, the new methodology presented is finite difference based, but essentially takes advantage of the best features of the two well-established numerical formulations, the finite difference and finite volume methods. Weaknesses of the finite difference approach are removed by exploiting the strengths of the finite volume method. In particular, the problems associated with the determination of pressure in a finite difference approach are resolved by implementing a SIMPLE-type algorithm to handle the velocity-pressure coupling.

2.2 Finite Differencing on a Staggered Grid

Let us consider a two-dimensional rectangular domain such as that shown in Figure 2.1. The domain has been discretized using a regular Cartesian mesh. For the sake of clarity, let us assume that Δx and Δy are constant, i.e., the mesh is uniform in each of the x and y

directions. The derivatives of the dependent variables appearing in the partial differential equations are approximated by finite differences.

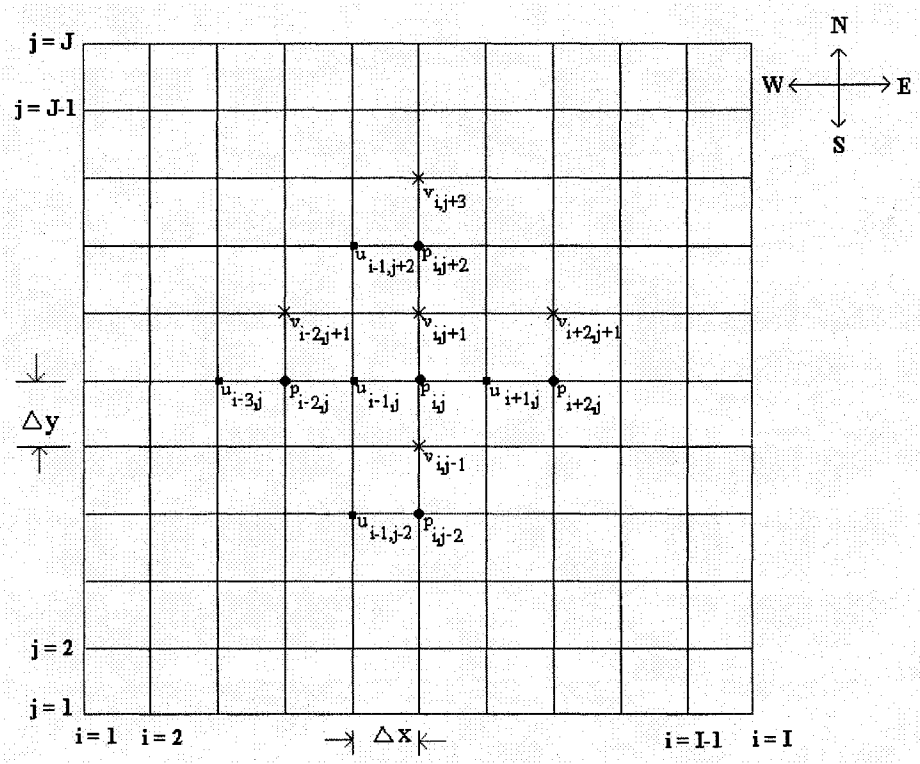

Figure 2.1 Staggered grid arrangement

A staggered grid is used to store the velocity components u and v and the pressure p. As indicated in Figure 2.1, the values of u and v are stored at the $i\text{-}1,j$ and $i,j+1$ locations respectively and p is stored at i,j. The advantages of using the staggered grid over a non-staggered grid are twofold. First, the continuity equation can be written at node i,j with second order accurate central differences without interpolation of the relevant velocity components. Second, it prevents odd-even coupling or what is known as checkerboarding between the pressure field and the velocity fields [21].

In this dissertation, the *u*-momentum equation is discretized at node *i*-1,*j*, the *v*-momentum equation is discretized at *i*,*j*+1, and the continuity equation is discretized at *i*,*j*.

The first order backward difference of the *x* derivative, used in the convective terms of the flow equations, are given by

$$u_x\big|_{i-1,j} \approx \frac{u_{i-1,j} - u_{i-3,j}}{2\Delta x}$$

$$v_x\big|_{i,j+1} \approx \frac{v_{i,j+1} - v_{i-2,j+1}}{2\Delta x}.$$

The second order central difference of the y derivative for the convective terms of the flow equations are given by

$$u_y\big|_{i-1,j} \approx \frac{u_{i-1,j+2} - u_{i-1,j-2}}{4\Delta y}$$

$$v_y\big|_{i,j+1} \approx \frac{v_{i,j+3} - v_{i,j-1}}{4\Delta y}.$$

Note that the differences are carried out on locations where the variables are calculated and stored. For example, $u_x\big|_{i-1,j}$ is approximated by *u* at *i-1,j* and *i-3,j* instead of being approximated using the value at *i-2,j* since *u* is not stored there.

The diffusion terms in the momentum equations are represented using second order accurate central differences, given by

$$u_{xx}\big|_{i-1,j} \approx \frac{u_{i-3,j} - 2u_{i-1,j} + u_{i+1,j}}{4\Delta x^2}$$

$$u_{yy}\big|_{i-1,j} \approx \frac{u_{i-1,j+2} - 2u_{i-1,j} + u_{i-1,j-2}}{4\Delta y^2}$$

$$v_{xx}\big|_{i,j+1} \approx \frac{v_{i-2,j+1} - 2v_{i,j+1} + v_{i+2,j+1}}{4\Delta x^2}$$

$$v_{yy}\big|_{i,j+1} \approx \frac{v_{i,j+3} - 2v_{i,j+1} + v_{i,j-1}}{4\Delta y^2}.$$

The pressure gradients are approximated by a second order accurate central difference approximation using the locations where p is defined. Since $\frac{\partial p}{\partial x}$ and $\frac{\partial p}{\partial y}$ appear in the u-momentum and v-momentum respectively, we take

$$p_x\big|_{i-1,j} \approx \frac{p_{i,j} - p_{i-2,j}}{2\Delta x}$$

$$p_y\big|_{i,j+1} \approx \frac{p_{i,j+2} - p_{i,j}}{2\Delta y}.$$

2.3 Discretization of the Momentum Equations

2.3.1 Discretized Equations at Interior Nodes

The discrete u-and v-momentum equations at interior nodes may be written respectively as

$$\begin{aligned} a_P^{\text{int}} u_{i-1,j} + a_N^{\text{int}} u_{i-1,j+2} + a_S^{\text{int}} u_{i-1,j-2} + a_W^{\text{int}} u_{i-3,j} + a_E^{\text{int}} u_{i+1,j} &= \frac{\hat{p}_{i-2,j} - \hat{p}_{i,j}}{2\rho\Delta x} \\ b_P^{\text{int}} v_{i,j+1} + b_N^{\text{int}} v_{i,j+3} + b_S^{\text{int}} v_{i,j-1} + b_W^{\text{int}} v_{i-2,j+1} + b_E^{\text{int}} v_{i+2,j+1} &= \frac{\hat{p}_{i,j} - \hat{p}_{i,j+2}}{2\rho\Delta y} \end{aligned} \tag{2.3}$$

where

$$a_P^{\text{int}} = \frac{\hat{u}_{i-1,j}}{2\Delta x} + \upsilon\left(\frac{1}{2\Delta x^2} + \frac{1}{2\Delta y^2}\right)$$

$$a_N^{\text{int}} = \frac{\hat{v}_{i-1,j}}{4\Delta y} - \frac{\upsilon}{4\Delta y^2}$$

$$a_S^{\text{int}} = -\frac{\hat{v}_{i-1,j}}{4\Delta y} - \frac{\upsilon}{4\Delta y^2}$$

$$a_W^{\text{int}} = -\frac{\hat{u}_{i-1,j}}{2\Delta x} - \frac{\upsilon}{4\Delta x^2}$$

$$a_E^{\text{int}} = -\frac{\upsilon}{4\Delta x^2},$$

and

$$b_P^{\text{int}} = \frac{\hat{u}_{i,j+1}}{2\Delta x} + \upsilon\left(\frac{1}{2\Delta x^2} + \frac{1}{2\Delta y^2}\right)$$

$$b_N^{\text{int}} = \frac{\hat{v}_{i,j+1}}{4\Delta y} - \frac{\upsilon}{4\Delta y^2}$$

$$b_S^{\text{int}} = -\frac{\hat{v}_{i,j+1}}{4\Delta y} - \frac{\upsilon}{4\Delta y^2}$$

$$b_W^{\text{int}} = -\frac{\hat{u}_{i,j+1}}{2\Delta x} - \frac{\upsilon}{4\Delta x^2}$$

$$b_E^{\text{int}} = -\frac{\upsilon}{4\Delta x^2}.$$

The notation used here closely follows that traditionally used in finite volume formulations. For example, the sub-index "*E*" in the coefficient a_E^{int} means that the coefficient is evaluated at the east neighbour of the *u*-node and "int" means at interior nodes, i.e., away from the boundaries. The same notation follows for the other coefficients. The caret above a variable indicates quantities that will be calculated at the previous iteration.

Because of the use of a staggered grid, the values of *v* in the *u*-momentum equation and *u* in the *v*-momentum equation, appearing as coefficients of the convective derivatives, are

not available at the desired points. Therefore, these velocities are computed to second order accuracy using the four surrounding grid points at which they are stored, i.e.

$$u\big|_{i,j+1} \approx \frac{u_{i+1,j} + u_{i+1,j+2} + u_{i-1,j} + u_{i-1,j+2}}{4}$$

$$v\big|_{i-1,j} \approx \frac{v_{i,j-1} + v_{i,j+1} + v_{i-2,j-1} + v_{i-2,j+1}}{4}.$$

In general, the u-momentum and v-momentum equations may be written respectively as

$$\begin{aligned} a_P u_P &= \sum_{nb} a_{nb} u_{nb} + \frac{1}{\rho} \frac{\hat{p}_{i-2,j} - \hat{p}_{i,j}}{2\Delta x} \\ b_P v_P &= \sum_{nb} b_{nb} v_{nb} + \frac{1}{\rho} \frac{\hat{p}_{i,j} - \hat{p}_{i,j+2}}{2\Delta y} \end{aligned} \tag{2.4}$$

Here, nb refers to the neighbours of the nodes where u_P and v_P are to be calculated.

Table 2.1 shows the difference between the u-momentum equation coefficients at interior nodes using finite difference and finite volume formulations. It is interesting to note that, for the finite difference formulation

$$a_p = -\sum a_{nb},$$

while, for the finite volume formulation

$$a_p = -\sum a_{nb} + \left[\frac{u_{i,j} - u_{i-2,j}}{2\Delta x} + \frac{v_{i-1,j+1} - v_{i-1,j-1}}{2\Delta y} \right].$$

This property of the finite difference formulation, that $a_p = -\sum a_{nb}$, means that the coefficient matrix is always diagonally dominant. Hence, iterative solution of the matrix equation will be stable. For the finite volume formulation, this feature only holds when the continuity equation is satisfied, in which case the term is the square bracket is identically zero.

The difference between these coefficients arises from the fact that the upwind differencing in a finite volume formulation is different from that in the finite difference formulations.

Formulation / Coefficient	Finite Difference	Finite Volume
a_P^{int}	$\frac{\hat{u}_{i-1,j}}{2\Delta x}+\upsilon\left(\frac{1}{2\Delta x^2}+\frac{1}{2\Delta y^2}\right)$	$\upsilon\left(\frac{1}{2\Delta x^2}+\frac{1}{2\Delta y^2}\right)+\frac{1}{2\Delta x}\hat{u}_{i,j}$ $+\frac{1}{4\Delta y}\left(\hat{v}_{i-1,j+1}-\hat{v}_{i-1,j-1}\right)$
a_W^{int}	$-\frac{\hat{u}_{i-1,j}}{2\Delta x}-\frac{\upsilon}{4\Delta x^2}$	$-\frac{\upsilon}{4\Delta x^2}-\frac{\hat{u}_{i-2,j}}{2\Delta x}$
a_E^{int}	$-\frac{\upsilon}{4\Delta x^2}$	$-\frac{\upsilon}{4\Delta x^2}$
a_N^{int}	$\frac{\hat{v}_{i-1,j}}{4\Delta y}-\frac{\upsilon}{4\Delta y^2}$	$\frac{\hat{v}_{i-1,j+1}}{4\Delta y}-\frac{\upsilon}{4\Delta y^2}$
a_S^{int}	$-\frac{\hat{v}_{i-1,j}}{4\Delta y}-\frac{\upsilon}{4\Delta y^2}$	$-\frac{\hat{v}_{i-1,j-1}}{4\Delta y}-\frac{\upsilon}{4\Delta y^2}$

Table 2.1 Comparison of FD and FV coefficients of the *u*-momentum equation

2.3.2 Discretized Equations at the Boundaries

Special attention must be given to the way the equations are discretized at nodes adjacent to the boundaries. This special treatment is explained separately for each type of boundary commonly encountered in computational fluid dynamics simulations.

2.3.2.1 Equations at a Wall Boundary

The derivatives in the u-and v-momentum equations may require special treatment at a wall boundary. The wall boundary could be an east, west, south or north boundary depending on the particular problem to be solved. Consider, for example, the case of a south wall boundary. The variable u is stored one node off that boundary, i.e., at $j = 2$ as shown in Figure 2.2. For this reason, to approximate derivatives of u in the y direction, a central difference with unequally spaced grid points is used, where the convective term is approximated using a second order accurate expression and the diffusion term by using a first order accurate expression. Thus,

$$\left.\frac{\partial^2 u}{\partial y^2}\right|_{i-1,2} \approx \frac{2u_{i-1,4} - 6u_{i-1,2} + 4u_{i-1,1}}{6\Delta y^2}$$

$$\left.\frac{\partial u}{\partial y}\right|_{i-1,2} \approx \frac{u_{i-1,4} + 3u_{i-1,2} - 4u_{i-1,1}}{6\Delta y}.$$

Then, the u-momentum equation along $j = 2$ will become

$$a_P^S u_{i-1,2} + a_N^S u_{i-1,4} + a_W^S u_{i-3,2} + a_E^S u_{i+1,2} = \frac{\hat{p}_{i-2,2} - \hat{p}_{i,2}}{2\rho\Delta x} + \left(\frac{2\upsilon}{3\Delta y^2} + \frac{2v_{i-1,2}}{3\Delta y}\right) u_{i-1,1}$$

where

$$a_P^S = \frac{\hat{u}_{i-1,2}}{2\Delta x} + \frac{\hat{v}_{i-1,2}}{2\Delta y} + \upsilon\left(\frac{1}{2\Delta x^2} + \frac{1}{\Delta y^2}\right)$$

$$a_N^S = \frac{\hat{v}_{i-1,2}}{6\Delta y} - \frac{\upsilon}{3\Delta y^2}$$

$$a_W^S = -\frac{\hat{u}_{i-1,2}}{2\Delta x} - \frac{\upsilon}{4\Delta x^2}$$

$$a_E^S = -\frac{\upsilon}{4\Delta x^2}.$$

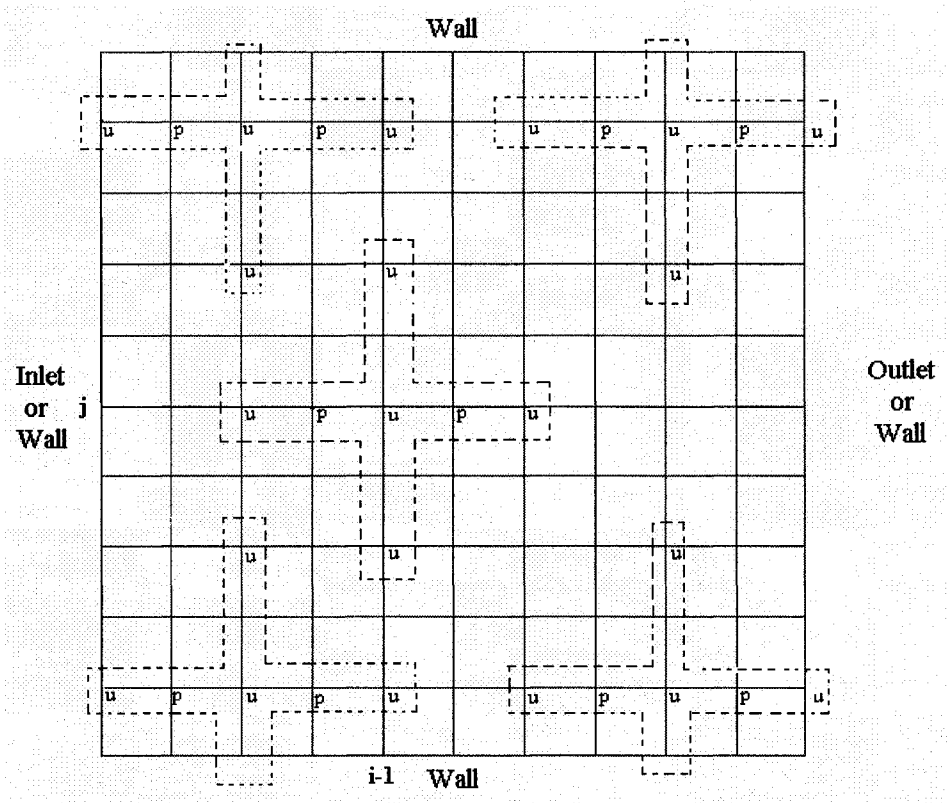

Figure 2.2 Stencils for the *u*-momentum equation

The values of u in the last term on the right hand side of the discretized equations are known from prescribed wall boundary conditions on $j = 1$. For example, if the south boundary is a stationary wall, then $u_{i-1,1} = 0$. If it is a moving wall, then $u_{i-1,1} \neq 0$.

The *v*-momentum equation at the south boundary will be the same as for interior points, i.e., equation (2.3), except that $v_{i,1}$ is known from the boundary condition. None of the terms in the *v*-momentum equation requires special treatment.

Now, if the north boundary ($j = J$) is a wall, a similar discussion as above follows for both the u and v equations, and the discretized *u*-momentum equation at i-1,J-1 becomes

$$a_P^N u_{i-1,J-1} + a_S^N u_{i-1,J-3} + a_W^N u_{i-3,J-1} + a_E^N u_{i+1,J-1} = \frac{\hat{p}_{i-2,J-1} - \hat{p}_{i,J-1}}{2\rho\Delta x} + u_{i-1,J}\left(\frac{2\upsilon}{3\Delta y^2} - \frac{2v_{i-1,J}}{3\Delta y}\right)$$

where

$$a_P^N = \frac{\hat{u}_{i-1,J-1}}{2\Delta x} - \frac{\hat{v}_{i-1,J-1}}{2\Delta y} + \upsilon\left(\frac{1}{2\Delta x^2} + \frac{1}{\Delta y^2}\right)$$

$$a_S^N = -\frac{\hat{v}_{i-1,J-1}}{6\Delta y} - \frac{\upsilon}{3\Delta y^2}$$

$$a_W^N = -\frac{\hat{u}_{i-1,J-1}}{2\Delta x} - \frac{\upsilon}{4\Delta x^2}$$

$$a_E^N = -\frac{\upsilon}{4\Delta x^2}.$$

Note here that J is the maximum number of nodes in the y direction.

A similar discussion follows if the west and east boundaries are walls, in which case the x derivatives receive special treatment.

2.3.2.2 Equations at an Inlet Boundary

The inlet boundary could be an east, west, south or north boundary. In the case of a west inlet boundary, v is stored one node off that boundary, i.e., at $i = 2$ as shown in Figure 2.3. For this reason, a central difference with unequally spaced grid points will be used to approximate the derivative of v normal to the inlet boundary, with the convective term approximated by a second order accurate expression and the diffusion term by a first order accurate expression. Thus,

$$\left.\frac{\partial^2 v}{\partial x^2}\right|_{2,j+1} \approx \frac{v_{4,j+1} - 3v_{2,j+1} + 2v_{1,j+1}}{3\Delta x^2}$$

$$\left.\frac{\partial v}{\partial x}\right|_{2,j+1} \approx \frac{v_{4,j+1} + 3v_{2,j+1} - 4v_{1,j+1}}{6\Delta x}.$$

Then, for v-nodes adjacent to the west inlet boundary, the v-momentum equation can be written as

$$b_P^W v_{2,j+1} + b_N^W v_{2,j+3} + b_S^W v_{2,j-1} + b_E^W v_{4,j+1} = \frac{\hat{p}_{2,j} - \hat{p}_{2,j+2}}{2\rho\Delta y} + \left(\frac{2u_{2,j+1}}{3\Delta x} + \frac{2\upsilon}{3\Delta x^2} \right) v_{1,j+1}$$

where

$$b_P^W = \frac{2\hat{u}_{2,j+1}}{3\Delta x} + \upsilon\left(\frac{1}{\Delta x^2} + \frac{1}{2\Delta y^2} \right)$$

$$b_N^W = \frac{\hat{v}_{2,j+1}}{4\Delta y} - \frac{\upsilon}{4\Delta y^2}$$

$$b_S^W = -\frac{\hat{v}_{2,j+1}}{4\Delta y} - \frac{\upsilon}{4\Delta y^2}$$

$$b_E^W = \frac{u_{2,j+1}}{6\Delta x} - \frac{\upsilon}{3\Delta x^2}.$$

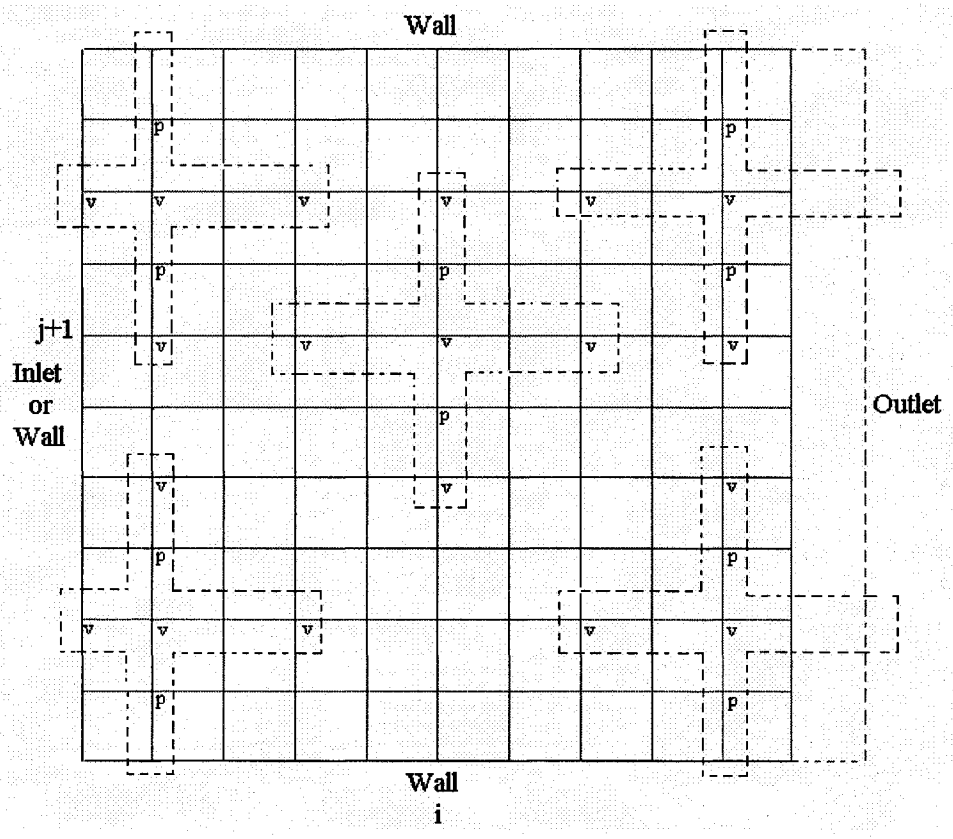

Figure 2.3 Stencils for the *v*-momentum equation

The value of $v_{1,j+1}$ in the last term on the right hand side of the discretized equations is known from the given inlet boundary conditions.

The *u*-momentum equation at the west side will remain the same as in equation (2.3), except that the value of $u_{1,j}$ is known.

A similar discussion as above follows if the inlet is at the east, north or south boundary, where the velocity components are specified on these boundaries.

2.3.2.3 Equations at an Outlet Boundary

The outlet boundary could be an east, west, south or north boundary. However, for several of the examples considered in the present work, the east boundary is the outlet boundary. The outlet boundary condition is taken as $\frac{\partial u}{\partial x} = 0$, $\frac{\partial v}{\partial x} = 0$. In discretized form,

the outlet flow boundary condition on u, applied at the east boundary (i = I), is approximated to first order by $u_{I,j} = u_{I-2,j}$. Applying this condition, the discretized u-momentum equation at I-2,j will be

$$a_P^E u_{I-2,j} + a_N^E u_{I-2,j+2} + a_S^E u_{I-2,j-2} + a_W^E u_{I-4,j} = \frac{\hat{p}_{I-3,j} - \hat{p}_{I-1,j}}{2\rho\Delta x}$$

where

$$a_P^E = \frac{\hat{u}_{I-2,j}}{2\Delta x} + \upsilon\left(\frac{1}{4\Delta x^2} + \frac{1}{2\Delta y^2}\right)$$

$$a_N^E = \frac{\hat{v}_{I-2,j}}{4\Delta y} - \frac{\upsilon}{4\Delta y^2}$$

$$a_S^E = -\frac{\hat{v}_{I-2,j}}{4\Delta y} - \frac{\upsilon}{4\Delta y^2}$$

$$a_W^E = -\frac{\hat{u}_{I-2,j}}{2\Delta x} - \frac{\upsilon}{4\Delta x^2}.$$

In the case of the v-momentum equation, the same type of boundary condition applies, so that $v_{I+1,j+1} = v_{I-1,j+1}$. Applying this condition, the discretized v-momentum at I-1,j+1 will become

$$b_P^E v_{I-1,j+1} + b_N^E v_{I-1,j+3} + b_S^E v_{I-1,j-1} + b_W^E v_{I-3,j+1} = \frac{\hat{p}_{I-1,j} - \hat{p}_{I-1,j+2}}{2\rho\Delta y}$$

$$a_P^E = \frac{\hat{u}_{I-1,j+1}}{2\Delta x} + \upsilon\left(\frac{1}{4\Delta x^2} + \frac{1}{2\Delta y^2}\right)$$

$$b_N^E = \frac{\hat{v}_{I-1,j+1}}{4\Delta y} - \frac{\upsilon}{4\Delta y^2}$$

$$b_S^E = -\frac{\hat{v}_{I-1,j+1}}{4\Delta y} - \frac{\upsilon}{4\Delta y^2}$$

$$b_W^E = -\frac{\hat{u}_{I-1,j+1}}{2\Delta x} - \frac{\upsilon}{4\Delta x^2}.$$

2.3.2.4 Equations at the West South and West North Corners

The discretized *u*-momentum equation developed at south and north boundaries can be used at these corners respectively, since no changes take place at the west boundary. The discretized *v*-momentum equation derived at the west boundary can be used at these corners, with velocities known at the south and north wall boundaries.

2.3.2.5 Equations at the East South and East North Corners

The discretized *u*-momentum equation obtained at south and north boundaries can be used at these corners, with the central coefficient modified by applying the boundary condition at the east side. The discretized *v*-momentum equation used at the east side will be used at these corners, with velocities known at the south and north wall boundaries.

2.4 Discretization of the Continuity Equation

The continuity equation is discretized at the points *i,j* where the pressure is defined, as illustrated in Figure 2.4. The discrete continuity equation, using second order accurate approximations, is written as

$$\frac{u_{i+1,j} - u_{i-1,j}}{2\Delta x} + \frac{v_{i,j+1} - v_{i,j-1}}{2\Delta y} = 0 \qquad (2.5)$$

which can also be written in the form

$$\frac{u_E - u_W}{2\Delta x} + \frac{v_N - v_S}{2\Delta y} = 0. \qquad (2.6)$$

The link between *u*, *v* and *p* will be discussed in detail in the next section.

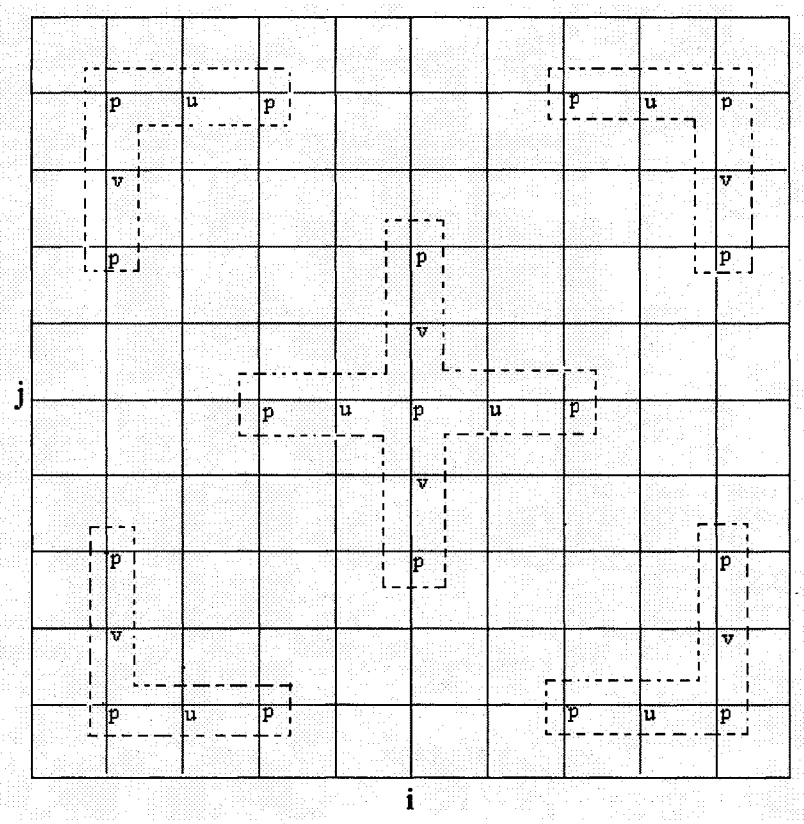

Figure 2.4 Stencils for the continuity equation

2.4.1 Velocity-Pressure Coupling

SIMPLE (Semi-Implicit Method for Pressure Linked Equations) is a primitive variable based method widely used in finite volume algorithms for the incompressible Navier-Stokes equations [15]. The primary idea behind SIMPLE is to create a discrete equation for pressure (or alternatively, a related quantity called the pressure correction) from the discrete continuity equation. Since the continuity equation contains discrete velocities, some way is needed to relate these discrete velocities to the discrete pressure field. The SIMPLE algorithm uses the discrete momentum equations to derive this coupling.

Let u^* and v^* be the discrete u and v fields resulting from a solution of the discrete u- and v-momentum equations. Let p^* represent the discrete pressure field which is used in the solution of the momentum equations. Thus, equations (2.3) can be written as

$$a_{i-1,j}u^*_{i-1,j} = \sum_{nb} a_{nb}u^*_{nb} + \frac{1}{\rho}\frac{p^*_{i-2,j} - p^*_{i,j}}{2\Delta x}$$
$$b_{i,j+1}v^*_{i,j+1} = \sum_{nb} b_{nb}v^*_{nb} + \frac{1}{\rho}\frac{p^*_{i,j} - p^*_{i,j+2}}{2\Delta y}. \tag{2.7}$$

If the pressure field p^* is only a guess or a prevailing iterate, the discrete u^* and v^* obtained by solving the momentum equations will not, in general, satisfy the discrete continuity equation (2.5).

In the SIMPLE approach, a correction is proposed to the starred velocity field such that the corrected values satisfy equation (2.5), i.e., we write

$$u = u^* + u'$$
$$v = v^* + v' \tag{2.8}$$

where u' and v' are corrections.

Correspondingly, the existing pressure field p^* is corrected with

$$p = p^* + p'. \tag{2.9}$$

Subtracting equation (2.7) from equation (2.4), we obtain

$$a_{i-1,j}u'_{i-1,j} = \sum_{nb} a_{nb}u'_{nb} + \frac{1}{\rho}\frac{p'_{i-2,j} - p'_{i,j}}{2\Delta x}$$
$$b_{i,j+1}v'_{i,j+1} = \sum_{nb} b_{nb}v'_{nb} + \frac{1}{\rho}\frac{p'_{i,j} - p'_{i,j+2}}{2\Delta y}. \tag{2.10}$$

Equations (2.10) represent the dependence of the velocity corrections u' and v' on the pressure correction p'. In effect, they tell us how the velocity field will respond when the pressure gradient is increased or decreased.

We now make a simplification, which is central to the SIMPLE method. Equations (2.10) are approximated as

$$a_{i-1,j}u'_{i-1,j} \approx \frac{1}{\rho}\frac{p'_{i-2,j} - p'_{i,j}}{2\Delta x}$$
$$b_{i,j+1}v'_{i,j+1} \approx \frac{1}{\rho}\frac{p'_{i,j} - p'_{i,j+2}}{2\Delta y}. \qquad (2.11)$$

So, equations (2.8) become

$$u_{i-1,j} = u^*_{i-1,j} + \frac{p'_{i-2,j} - p'_{i,j}}{2\rho\Delta x a_{i-1,j}}$$
$$v_{i,j+1} = v^*_{i,j+1} + \frac{p'_{i,j} - p'_{i,j+2}}{2\rho\Delta y b_{i,j+1}}. \qquad (2.12)$$

It is important to realize that because we are solving for the pressure correction rather than the pressure itself, the omission of the terms $\sum_{nb} a_{nb}u'_{nb}$ and $\sum_{nb} a_{nb}v'_{nb}$ in deriving the pressure correction equation is of no consequence as far as the final converged results are concerned, since all of these terms become zero.

Now consider the discrete continuity equation. The starred velocities u^* and v^*, obtained by solving the momentum equations using the prevailing pressure field p^*, do not satisfy the discrete continuity equation. Thus

$$\frac{u^*_{i+1,j} - u^*_{i-1,j}}{2\Delta x} + \frac{v^*_{i,j+1} - v^*_{i,j-1}}{2\Delta y} \neq 0$$

We require the corrected velocities, given by equations (2.12), to satisfy the continuity equation (2.5). Thus,

$$\frac{\left\{u^*_{i+1,j}+\frac{1}{\rho}\frac{p'_{i,j}-p'_{i+2,j}}{2\Delta x a_{i+1,j}}\right\}-\left\{u^*_{i-1,j}+\frac{1}{\rho}\frac{p'_{i-2,j}-p'_{i,j}}{2\Delta x a_{i-1,j}}\right\}}{2\Delta x}$$
$$+\frac{\left\{v^*_{i,j+1}+\frac{1}{\rho}\frac{p'_{i,j}-p'_{i,j+2}}{2\Delta y b_{i,j+1}}\right\}-\left\{v^*_{i,j-1}+\frac{1}{\rho}\frac{p'_{i,j-2}-p'_{i,j}}{2\Delta y b_{i,j-1}}\right\}}{2\Delta y}=0$$

Rearranging terms, we can write an equation for the pressure correction as

$$c_P^{\text{int}}p'_{i,j}+c_E^{\text{int}}p'_{i+2,j}+c_W^{\text{int}}p'_{i-2,j}+c_N^{\text{int}}p'_{i,j+2}+c_S^{\text{int}}p'_{i,j-2}=\frac{u^*_{i-1,j}-u^*_{i+1,j}}{2\Delta x}-\frac{v^*_{i,j+1}-v^*_{i,j-1}}{2\Delta y} \qquad (2.13)$$

where

$$c_P^{\text{int}}=\frac{1}{4\rho\Delta x^2 a_{i+1,j}}+\frac{1}{4\rho\Delta x^2 a_{i-1,j}}+\frac{1}{4\rho\Delta y^2 b_{i,j+1}}+\frac{1}{4\rho\Delta y^2 b_{i,j-1}}$$

$$c_E^{\text{int}}=-\frac{1}{4\rho\Delta x^2 a_{i+1,j}}$$

$$c_W^{\text{int}}=-\frac{1}{4\rho\Delta x^2 a_{i-1,j}}$$

$$c_N^{\text{int}}=-\frac{1}{4\rho\Delta y^2 b_{i,j+1}}$$

$$c_S^{\text{int}}=-\frac{1}{4\rho\Delta y^2 b_{i,j-1}}.$$

2.4.2 Pressure Correction Equation at the Boundaries

The discretized continuity equation at node *i,j* is given by

$$\frac{u_{i+1,j}-u_{i-1,j}}{2\Delta x}+\frac{v_{i,j+1}-v_{i,j-1}}{2\Delta y}=0. \tag{2.5}$$

Based on the specific boundary information, the pressure correction equation will have different forms on different boundaries.

Suppose, for example, that the velocity component v is known at the south and north boundaries and u is known at the west boundary.

2.4.2.1 Pressure Correction Equation at the West Boundary

Assuming u is known on the west boundary ($i = 1$), the discretized continuity equation at $i = 2$ will be

$$\frac{u_{3,j}}{2\Delta x}+\frac{v_{2,j+1}-v_{2,j-1}}{2\Delta y}=\frac{u_{1,j}}{2\Delta x}$$

where the right hand side is known. Following the same procedure as in section 2.4.1, the pressure correction equation for nodes adjacent to the west boundary becomes

$$c_P^W p'_{2,j}+c_E^{\text{int}} p'_{4,j}+c_N^{\text{int}} p'_{2,j+2}+c_S^{\text{int}} p'_{2,j-2}=\frac{u_{1,j}-u^*_{3,j}}{2\Delta x}-\frac{v^*_{2,j+1}-v^*_{2,j-1}}{2\Delta y}$$

where

$$c_P^W=\frac{1}{4\rho\Delta x^2 a_{3,j}}+\frac{1}{4\rho\Delta y^2 b_{2,j+1}}+\frac{1}{4\rho\Delta y^2 b_{2,j-1}}$$

and all other coefficients are the same as defined at the interior nodes.

2.4.2.2 Pressure Correction Equation at the South Boundary

The discretized continuity equation near the south wall boundary (i.e., at $j = 2$) is written as

$$\frac{u_{i+1,2} - u_{i-1,2}}{2\Delta x} + \frac{v_{i,3}}{2\Delta y} = \frac{v_{i,1}}{2\Delta y}.$$

In this case, the pressure correction equation will become

$$c_P^S p'_{i,2} + c_E^{\text{int}} p'_{i+2,2} + c_W^{\text{int}} p'_{i-2,2} + c_N^{\text{int}} p'_{i,4} = \frac{u^*_{i-1,2} - u^*_{i+1,2}}{2\Delta x} - \frac{v^*_{i,3} - v_{i,1}}{2\Delta y}$$

where

$$c_P^S = \frac{1}{4\rho\Delta x^2 a_{i+1,2}} + \frac{1}{4\rho\Delta x^2 a_{i-1,2}} + \frac{1}{4\rho\Delta y^2 b_{i,3}}$$

and all other coefficients are the same as defined at the interior nodes.

2.4.2.3 Pressure Correction Equation at the North Boundary

The discretized continuity equation at a north wall boundary (i.e., at $j = J$-1) is written as

$$\frac{u_{i+1,J-1} - u_{i-1,J-1}}{2\Delta x} - \frac{v_{i,J-2}}{2\Delta y} = -\frac{v_{i,J}}{2\Delta y}.$$

Therefore, the pressure correction equation becomes

$$c_P^N p'_{i,J-1} + c_E^{\text{int}} p'_{i+2,J-1} + c_W^{\text{int}} p'_{i-2,J-1} + c_S^{\text{int}} p'_{i,J-3} = \frac{u^*_{i-1,J-1} - u^*_{i+1,J-1}}{2\Delta x} - \frac{v_{i,J} - v^*_{i,J-2}}{2\Delta y}$$

where

$$c_P^N = \frac{1}{4\rho\Delta x^2 a_{i+1,J-1}} + \frac{1}{4\rho\Delta x^2 a_{i-1,J-1}} + \frac{1}{4\rho\Delta y^2 b_{i,J-2}}$$

and all other coefficients are the same as defined at the interior nodes.

2.4.2.4 Pressure Correction Equation at the East Boundary

If the east boundary ($i = I$) is an outlet, the velocity is not known there, and is not corrected by means of pressure corrections. Hence, in the discretized pressure correction equation, the link to the outlet boundary side is suppressed by setting $c_E = 0$ [21]. Therefore the pressure correction equation at the east boundary is given by

$$c_P^{\text{int}} p'_{I-1,j} + c_W^{\text{int}} p'_{I-3,j} + c_N^{\text{int}} p'_{I-1,j+2} + c_S^{\text{int}} p'_{I-1,j-2} = \frac{u^*_{I-2,j} - u_{I,j}}{2\Delta x} - \frac{v^*_{I-1,j+1} - v^*_{I-1,j-1}}{2\Delta y}$$

where all coefficients are the same as those at the interior nodes.

2.5 Overall Solution Algorithm

The overall solution procedure is the following:

1. Guess the pressure field p^* and initialize u and v.
2. Solve the discretized momentum equations (2.3) for u and v using the guessed value p^*. Call these solutions the u^* and v^* fields.
3. Solve the pressure correction equation (2.13).
4. Correct the pressure field using equation (2.9).
5. Evaluate u' and v' using equation (2.11).
6. Correct the velocity fields using equations (2.8).
7. Solve the momentum equations (2.3) for u and v, using the new pressure field, and the corrected velocities in the coefficients.
8. If the solution is converged, stop. Else go to step 3.

The system of discretized equations is solved by applying the TDMA (Tri-Diagonal Matrix Algorithm) [21]. This algorithm gives a direct non-iterative solution in the one-dimensional case. The TDMA is applied line by line to solve for u, v and p. In this case,

the solution is iterative. The algorithm sweeps once from left to right across the grid to solve for u, v and p. Solutions obtained are then used as old solutions to sweep again, and this process continues until a converged solution is obtained.

2.6 Analysis of the Pressure Correction Equation

In order to determine the dominant error term of the finite difference equations obtained using the proposed method, analysis given by Hirt [36] can be used. In this method, the terms of the finite difference equations are expanded in a Taylor series in order to develop a continuum partial differential equation. The differential equation obtained is known as the modified partial differential equation.

The modified partial differential equation will be derived for pressure correction only, since the pressure correction equation obtained in this work is of a new form. The u and v equations will not be considered because their form is similar to ones found in the literature.

Consider the discretized continuity equation in Cartesian coordinates

$$\frac{u_{i+1,j}-u_{i-1,j}}{2\Delta x}+\frac{v_{i,j+1}-v_{i,j-1}}{2\Delta y}=0. \tag{2.5}$$

This equation, as shown in Section 2.4.1, can be used to derive an equation for the pressure correction:

$$c_P^{\text{int}} p'_{i,j}+c_E^{\text{int}} p'_{i+2,j}+c_W^{\text{int}} p'_{i-2,j}+c_N^{\text{int}} p'_{i,j+2}+c_S^{\text{int}} p'_{i,j-2}=\frac{u^*_{i-1,j}-u^*_{i+1,j}}{2\Delta x}-\frac{v^*_{i,j+1}-v^*_{i,j-1}}{2\Delta y}. \tag{2.13}$$

Now evaluate each term of equation (2.13) by expanding in a Taylor series about (i,j). For example, expansion of $u^*_{i+1,j}$ gives

$$u^*_{i+1,j}=u^*_{i,j}+\frac{\partial u^*_{i,j}}{\partial x}\Delta x+\frac{\partial^2 u^*_{i,j}}{\partial x^2}\frac{\Delta x^2}{2}+O(\Delta x^3).$$

After substituting all expanded terms into equation (2.13), the so-called modified partial differential equation can be written as

$$\left(-\frac{1}{a_{i+1,j}}+\frac{1}{a_{i-1,j}}\right)p_x^{'}+\frac{\Delta x}{\Delta y}\left(-\frac{1}{b_{i,j+1}}+\frac{1}{b_{i,j-1}}\right)p_y^{'}+\Delta x\left(-\frac{1}{a_{i+1,j}}-\frac{1}{a_{i-1,j}}\right)p_{xx}^{'}$$
$$+\Delta x\left(-\frac{1}{b_{i,j+1}}-\frac{1}{b_{i,j-1}}\right)p_{yy}^{'}+O\left(\Delta x^4,\Delta y^3\Delta x\right)=-2\rho\Delta x\left(u_x^*+v_y^*\right)-\frac{1}{3}\rho\frac{\partial^3 u^*}{\partial x^3}\Delta x^3 \quad (2.14)$$
$$-\frac{1}{3}\rho\frac{\partial^3 v^*}{\partial y^3}\Delta x\Delta y^2+O\left(\Delta x^5,\Delta y^4\Delta x\right).$$

Note that the coefficients in equation (2.14) can be expanded as follows:

$$\frac{1}{a_{i+1,j}}=-\frac{4\Delta x^2}{\upsilon}$$

$$\frac{1}{a_{i-1,j}}=\frac{2\Delta x^2}{\upsilon\left(1+\beta^2\right)}\left[1+\frac{\hat{u}_{i-1,j}}{\upsilon\left(1+\beta^2\right)}\Delta x\right]^{-1}$$

$$=\frac{2\Delta x^2}{\upsilon\left(1+\beta^2\right)}-\frac{2\hat{u}_{i,j}}{\upsilon^2\left(1+\beta^2\right)^2}\Delta x^3+O\left(\Delta x^4\right) \quad (2.15)$$

$$\frac{1}{b_{i,j+1}}=\frac{2\Delta x^2}{\upsilon\left(1+\beta^2\right)}-\frac{2\hat{u}_{i,j}}{\upsilon^2\left(1+\beta^2\right)^2}\Delta x^3+O\left(\Delta x^4,\Delta x^3\Delta y\right)$$

$$\frac{1}{b_{i,j-1}}=-\frac{4\Delta y^2}{\upsilon}+\frac{4\hat{v}_{i,j}}{\upsilon^2}\Delta y^3+O\left(\Delta y^4\right)$$

where $\beta=\frac{\Delta x}{\Delta y}$.

Substituting equations (2.15) in (2.14), the modified partial differential equation becomes

$$\frac{2}{\upsilon}\Delta x^2\left(\frac{1+2\beta^2}{1+\beta^2}\right)p_{xx}^{'}+\frac{2}{\upsilon}\Delta y^2\left(\frac{2+\beta^2}{1+\beta^2}\right)p_{yy}^{'}+\frac{2}{\upsilon}\Delta x\left(\frac{3+2\beta^2}{1+\beta^2}\right)p_x^{'}-\frac{2}{\upsilon}\Delta y\left(\frac{2+3\beta^2}{1+\beta^2}\right)p_y^{'}$$
$$-\frac{2\hat{u}_{i,j}}{\upsilon^2\left(1+\beta^2\right)^2}\Delta x^2 p_x^{'}+\frac{2\beta\hat{u}_{i,j}}{\upsilon^2\left(1+\beta^2\right)^2}\Delta x^2 p_y^{'}+\frac{4\hat{v}_{i,j}}{\upsilon^2}\Delta y^2 p_y^{'}= \quad (2.16)$$

$$-2\rho\left(u_x^* + v_y^*\right) - \frac{1}{3}\rho\left(\frac{\partial^3 u^*}{\partial x^3}\Delta x^2 + \frac{\partial^3 v^*}{\partial y^3}\Delta y^2\right) + O\left(\Delta x^3, \Delta y^3\right)$$

If we set $\Delta x = \Delta y$, then equation (2.16) becomes

$$\begin{aligned} &2\rho\left(u_x^* + v_y^*\right) + \frac{5}{\upsilon}\left(p_x' - p_y'\right)\Delta x + \left[\frac{3}{\upsilon}\nabla^2 p' - \frac{u^*}{2\upsilon^2}\left(p_x' - p_y'\right) + \frac{4v^*}{\upsilon^2}p_y'\right]\Delta x^2 \\ &-\frac{1}{3}\rho\left(\frac{\partial^3 u^*}{\partial x^3} + \frac{\partial^3 v^*}{\partial y^3}\right)\Delta x^2 + O\left(\Delta x^3\right) = 0 \end{aligned} \tag{2.17}$$

The leading order terms in equation (2.17) are

$$2\rho\left(u_x^* + v_y^*\right) + \frac{5}{\upsilon}\left(p_x' - p_y'\right)\Delta x + O\left(\Delta x^2, \Delta y^2\right) = 0$$

Strictly speaking, this equation should not be referred to as the modified partial differential equation for p', since there is no partial differential equation for pressure correction to compare it to. However, this first order equation for p' has some interesting features. The $O(\Delta x)$ terms involving pressure correction on the left hand side will be zero when the solution converges since p' is zero at convergence, and the zeroth order terms are the divergence of velocity, so when the solution converges these terms become zero. Similar methods have been described in CFD textbooks, for example, Chung [37], Tannehill et al [38], Anderson [39], and Ferziger and Peric [40]. However, these methods are generally formulated for unsteady flows, and express the pressure correction in terms of the time derivative of velocity. In the notation of this thesis, Chung [37], for example, proposed the correction $u'_{i-1,j} = \frac{\Delta t}{\rho}\frac{p'_{i-2,j} - p'_{i,j}}{2\Delta x}$. This correction is different from the one proposed in this thesis, i.e., $u'_{i-1,j} = \frac{1}{\rho}\frac{p'_{i-2,j} - p'_{i,j}}{2a_{i-1,j}\Delta x}$. Following the same steps as above,

the finite difference equation for the pressure correction proposed by Chung [37] can be written in the form

$$\frac{\left\{u^*_{i+1,j}+\frac{\Delta t}{\rho}\frac{p'_{i,j}-p'_{i+2,j}}{2\Delta x}\right\}-\left\{u^*_{i-1,j}+\frac{\Delta t}{\rho}\frac{p'_{i-2,j}-p'_{i,j}}{2\Delta x}\right\}}{2\Delta x}$$
$$+\frac{\left\{v^*_{i,j+1}+\frac{\Delta t}{\rho}\frac{p'_{i,j}-p'_{i,j+2}}{2\Delta y}\right\}-\left\{v^*_{i,j-1}+\frac{\Delta t}{\rho}\frac{p'_{i,j-2}-p'_{i,j}}{2\Delta y}\right\}}{2\Delta y}=0$$

which leads to an equation similar to equation (2.13), but with different coefficients. The modified partial differential equation for this formulation can be written as

$$\nabla^2 p' = \frac{\rho}{\Delta t}\left(\frac{\partial u^*}{\partial x}+\frac{\partial v^*}{\partial y}\right).$$

This equation is a Poisson equation for the pressure correction, different from equation (2.17).

CHAPTER III

APPLICATIONS ON A CARTESIAN GRID

3.1 Introduction

In this chapter, the algorithm developed in Chapter 2 is applied to three well-established benchmark problems, namely, the developing flow in a rectangular duct, flow over a backward-facing step and flow in a lid-driven cavity. These problems are considered to be important validation test cases for any numerical model.

The developing flow in a rectangular duct is one of the few problems that have exact solution in the downstream region and moreover, it is a good test to check the algorithm for mass conservation. The backward-facing step is one of the most fundamental geometries causing flow separation. The fluid motion in a lid-driven cavity is an example of closed streamline problems that are of theoretical importance because they exhibit the primary features of a broad class of steady, separated flows. Despite its simple geometry, the lid-driven cavity flow retains a rich fluid flow physics manifested by multiple counter-rotating recirculating regions in the corners of the cavity depending on the Reynolds number.

3.2 Developing Flow in a Rectangular Duct

In general the problem of finding exact solutions of the Navier-Stokes equations presents significant and nearly insurmountable mathematical difficulties. However, it is possible to find exact solutions in certain particular cases. One of the simplest problems is that of parallel flow.

A flow is called parallel if only one velocity component is different from zero, so that all fluid particles move in one direction. If, in the two-dimensional flow equations, the velocity component v is taken to be zero everywhere, it follows from the continuity equation that

$$\frac{\partial u}{\partial x} = 0.$$

Thus, for a parallel flow we have

$$u = u(y), v = 0.$$

From the v-momentum equation it is clear that

$$\frac{\partial p}{\partial y} = 0.$$

All the convective terms vanish in the u-momentum equation. Hence

$$\frac{dp}{dx} = \rho \upsilon \frac{d^2 u}{dy^2}.$$

Since $\frac{\partial p}{\partial y} = 0$ and u is a function of y only, this equation implies that the pressure gradient in the direction of flow is constant, say c.

This is the basis for the Poiseuille flow in a straight two-dimensional duct aligned with the x-axis. Considering a duct of width D, and imposing the boundary conditions $u = 0$ for $y = 0$ and $y = D$, the analytical solution is $u = -\frac{c}{2\rho\upsilon} y(D - y)$.

Now consider flow development in a straight two-dimensional channel. The length L of the channel is taken to be ten times the width D, and we take $D = 1$. At the entrance of the channel a uniform flow, $u = 1$, is specified as the inlet velocity profile. The transverse velocity is set equal to zero at the inlet. A parallel flow condition is specified at the outlet

i.e. $\frac{\partial u}{\partial x} = 0$. The no-slip condition is applied at the lower and upper walls. As the fluid enters the channel, the wall boundary conditions distort the uniform flow as boundary layers grow on the walls. The flow develops along the channel for some distance, referred to as the "development length", until it becomes fully developed. At this point, the flow field is that described by Poiseuille flow.

3.2.1 Results and Discussion

The numerical model has been verified against alternative numerical predictions and the analytical solution which is formed at the outlet after the solution becomes fully developed. To implement the numerical method proposed in this work, a 201x41 rectangular mesh is created. The predicted, fully developed streamwise velocity profile for Re = 50, is compared with the analytical solution. The agreement between the two is excellent, as seen in Figure 3.1.

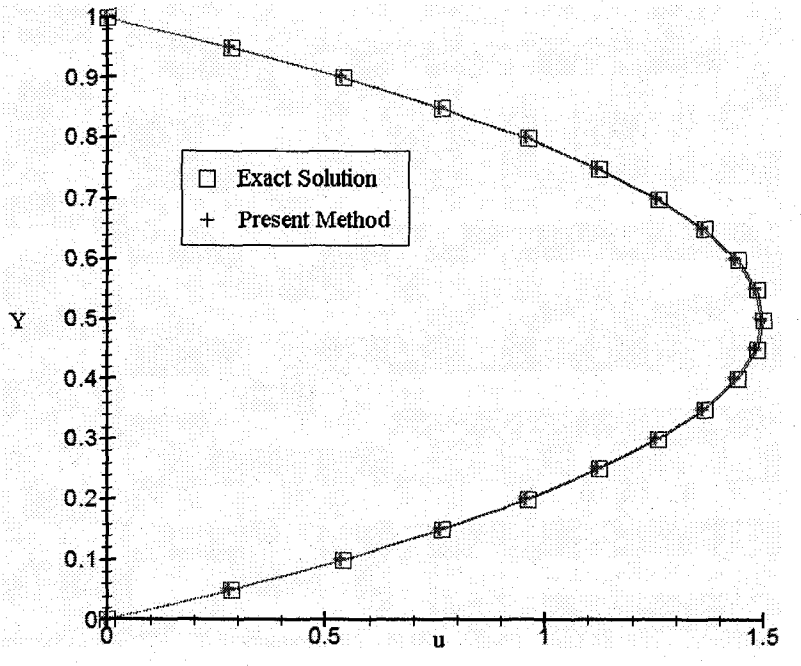

Figure 3.1 Fully developed velocity profile

The centreline velocity as a function of the distance from the inlet is plotted in Figure 3.2. At this *Re*, the parabolic profile starts to form at about $x = 2$, which agrees with the results of Schlichting [41]. The result obtained are more accurate than those obtained by Reggio and Camarero [28] where the parabolic profile starts further downstream, around $x = 4$. Reggio and Camarero's method underpredicts the centreline velocity, even in the fully developed region. Their results are based on the finite volume method. This demonstrates the ability of the present method to conserve the mass flow. Numerical calculations show that the pressure becomes uniform in the transverse direction and the streamwise pressure gradient is constant once the fully developed region is reached.

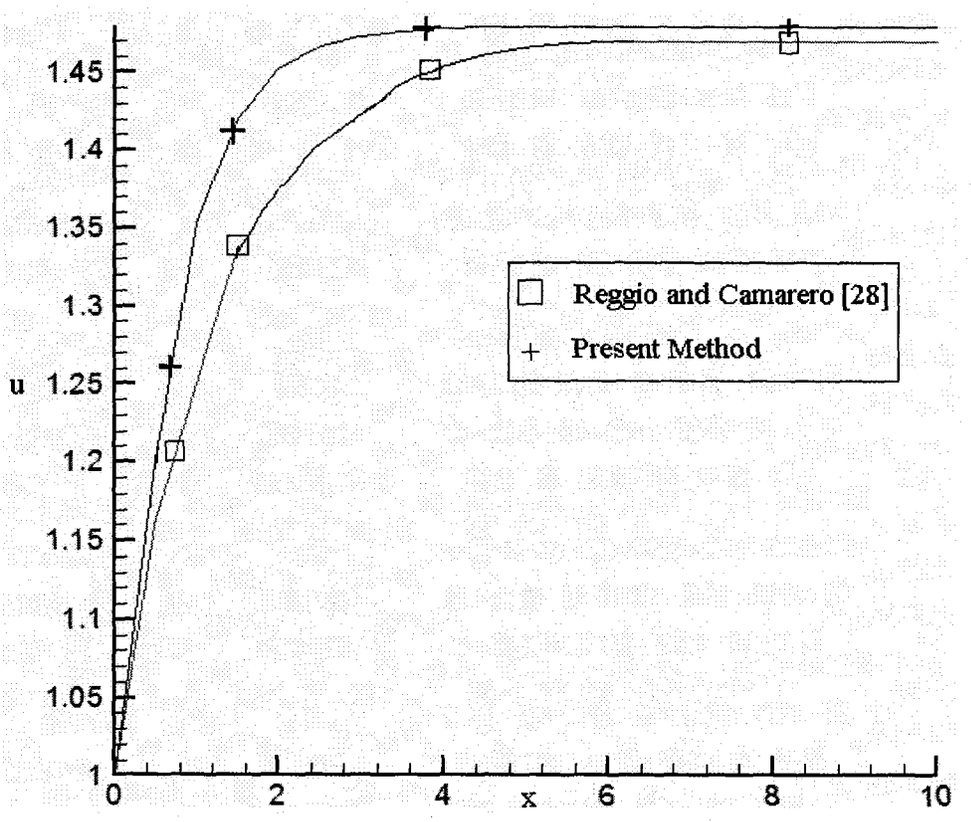

Figure 3.2 Centreline velocity, *Re* = 50

3.3 Flow over a Backward-facing Step

The backward-facing step is one of the most fundamental geometries causing flow separation and is an important validation test case for any numerical model. Much of the literature on separated flows over a backward-facing step deals with the turbulent regime. For turbulent flows, typical experimental studies such as those reported by Kim [42] and O'Malley et al [43] and numerical solutions presented by Hackman et al [44] found that reattachment occurs at a fixed position downstream of the step, irrespective of the Reynolds number. The distance was reported to be between five and eight step heights from the separation point.

In contrast, experiments conducted in the laminar regime reveal that the reattachment length is not constant, but increases with Reynolds number. Experiments in this regime have been carried out for various geometries. For example, Goldstein et al [45] considered laminar flow over a downstream facing step adjacent to a free stream. Thangam and Knight [46] studied flow through a duct with an expansion ratio (ratio of step height to channel height) of 0.75. In addition, computational predictions have been reported by numerous authors, including Ghoniem and Gagnon [47], Guj and Stella [48] and Barton [49].

At low Reynolds number the flow separates at the sharp corner of the step and then reattaches itself to the lower boundary further downstream, forming a single primary recirculating eddy. As discussed by Barton [49], the reattachment length increases almost linearly with Reynolds number, which is based on twice the step height and the average velocity $\left(Re = \frac{U_{av} 2h}{\upsilon} \right)$, the slight non-linear trend being attributed to viscous drag along the upper boundary. This increase occurs up to a Reynolds number of approximately

1200. A further increase in Reynolds number causes the velocity fluctuations to increase, indicating the beginning of transition to turbulent flow (Armaly et al [50]). However, at the higher Reynolds numbers in the laminar regime ($400 \le Re < 1200$), the adverse pressure gradient along the upper boundary is strong enough to promote a secondary recirculation zone attached to the upper wall, which causes a reduction in the growth of the lower eddy. At this value of Reynolds number, measurements and predictions start to deviate from each other. The deviations are explainable by the inherent three-dimensionality of the experimental flow for $Re \ge 400$ (Armaly et al [50]).

3.3.1 Problem Specification and Boundary Conditions

The intention in this problem is to test the new approach described in Chapter 2 for solving the flow equations and predicting separation. For this reason, as shown in Figure 3.3, the standard step geometry was simplified by excluding the channel upstream of the step. The flow is assumed to be fully developed when it reaches the step. The downstream channel was defined to have height 2h, with a step height and upstream inlet equal to h. In this work, we have taken $2h = 1$. The length L from the step to the end of the calculation domain depends on *Re*. This length must be chosen to ensure that the reattachment length is independent of the length of the calculation domain.

The inlet condition is obtained from steady Poiseuille flow, given by the equation

$$\frac{d^2u}{dy^2} = -\frac{c}{\rho\upsilon} \quad \text{and } v = 0 \tag{3.1}$$

where $c = -\frac{dp}{dx}$ is the constant pressure gradient.

Integrating equation (3.1), and applying the no-slip conditions at the walls, $u(y = 0.5) = 0$ and $u(y = 1) = 0$, we get

$$u = \frac{c}{2\rho\upsilon} y(1.5 - y) - \frac{c}{4\rho\upsilon}. \tag{3.2}$$

The boundary conditions for the step geometry include the usual no-slip velocity specification $u = 0$ and $v = 0$ for all solid surfaces as shown in Figure 3.3. The outflow boundary condition is obtained by assuming the outflow is parallel to the x-axis, that is $\frac{\partial u}{\partial x} = 0$ and $\frac{\partial v}{\partial x} = 0$.

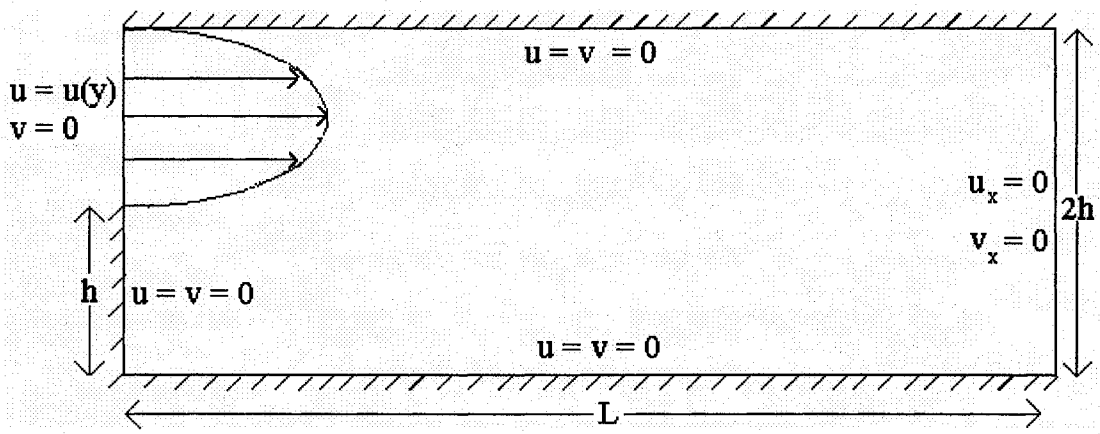

Figure 3.3 Backward-facing step

3.3.2 Results and Discussion

The numerical model was validated against experimental and alternative numerical predictions of steady laminar flow past a backward-facing step. Results for Re = 50, 100, 200, 400, 500 are compared with those obtained by Armaly et al [50], Barton [49], and Barber and Fonty [51]. The commercial computational fluid dynamics code CFD-ACE+ [52] results, based upon a primitive variable finite volume solution, are included to provide additional validation of the proposed method (Barber and Fonty [51]). FLUENT has also been used to validate the results. Table 3.1 shows the number of iterations for

convergence, spatial step and mesh sizes used in the simulations for different Reynolds number. Table 3.2 gives a comparison of the reattachment lengths predicted by the present method with other numerical simulations and the experimental work of Armaly et al. [50]. Reattachment lengths obtained by using two different convergence criteria, $|u_{new} - u_{old}| < 10^{-8}$ and $\frac{\sum |u_{new} - u_{old}|}{\sum u_{new}} < 10^{-3}$ are identical, but are not very close to the results reported in the literature for $Re < 200$. The results showed in Table 3.1 are based on the criteria $|u_{new} - u_{old}| < 10^{-9}$ for Re = 50, 100, 200 and $|u_{new} - u_{old}| < 10^{-8}$ for Re = 400 and 500. These results agree very well with those found in the literature.

	$Re = 50$	$Re = 100$	$Re = 200$	$Re = 400$	$Re = 500$
Mesh size IxJ	101x41	201x41	301x41	961x81	1201x81
Δy	0.025	0.025	0.025	0.0125	0.0125
Δx	0.025	0.025	0.025	0.0125	0.01
Iterations	1283	4028	9403	2750	3251

Table 3.1 Number of iterations, spatial step and mesh sizes

Re	Armaly et al [50] Experimental	Barber & Fonty [51] Numerical	ACE-CFD [51] Numerical	Present Method Numerical
50	0.90	1	1	1
100	1.40	1.50	1.50	1.50
200	2.50	2.6	2.59	2.59
400	3.75	5.15	5.1	5.47
500	4.4	6.65	6.6	6.34

Table 3.2 Reattachment length as a function of *Re*

Figures 3.4 and 3.5 show the streamlines of $Re = 50$ and $Re = 200$.

To confirm that the results obtained are independent of grid resolution, the case of $Re = 100$ is considered. In this case, the mesh size first considered is 201x41. Another mesh of twice the resolution (401x81) has also been used. The reattachment lengths and number of iterations obtained using these two meshes are almost identical.

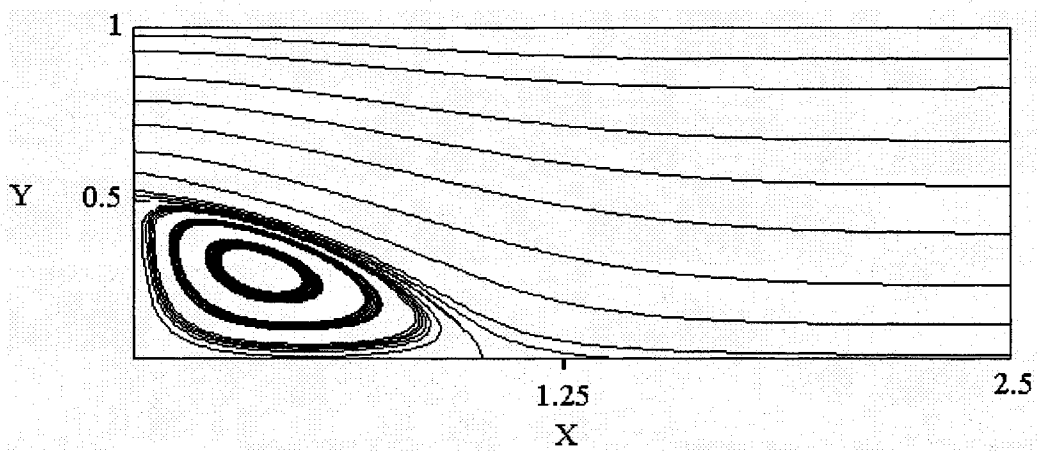

Figure 3.4 Streamlines for $Re = 50$

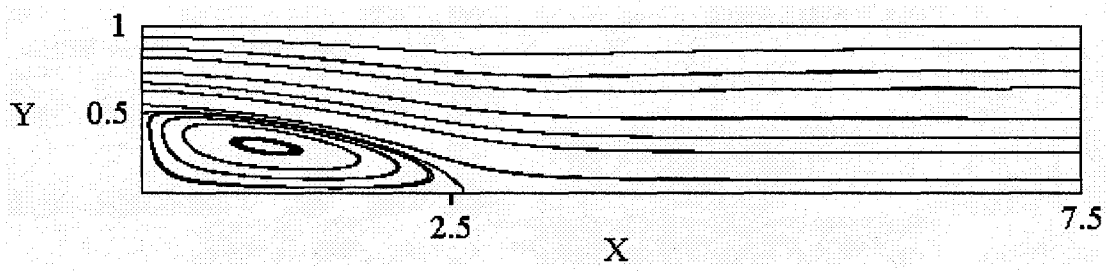

Figure 3.5 Streamlines for $Re = 200$

Another case for $Re = 50$ was also considered to validate the present method. In this case, the expansion ratio E (ratio of step height to channel height) is 0.75, as illustrated in Figure 3.6. The number of iteration required for convergence on a 201x41 mesh with $\Delta x = 0.025$ and $\Delta y = 0.025$ is 5321. The reattachment length is 1.92. The reattachment reported by Thangam and Knight [46] for this case is 2.2.

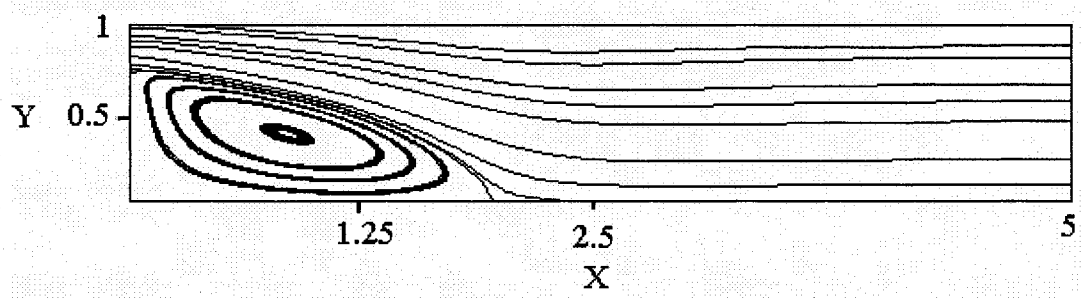

Figure 3.6 Streamlines for $Re = 50$, $E = 0.75$

Results obtained for $Re = 200$ are also compared in more detail to those obtained using FLUENT. The reattachment length obtained using FLUENT is 2.47. Figures 3.7 and 3.8 show the u and v velocity, respectively, along the vertical line $x = 1.2$, which lies in the recirculation zone (see Figure 3.5). Figure 3.9 shows the u velocity downstream of the reattachment point, at $x = 5$.

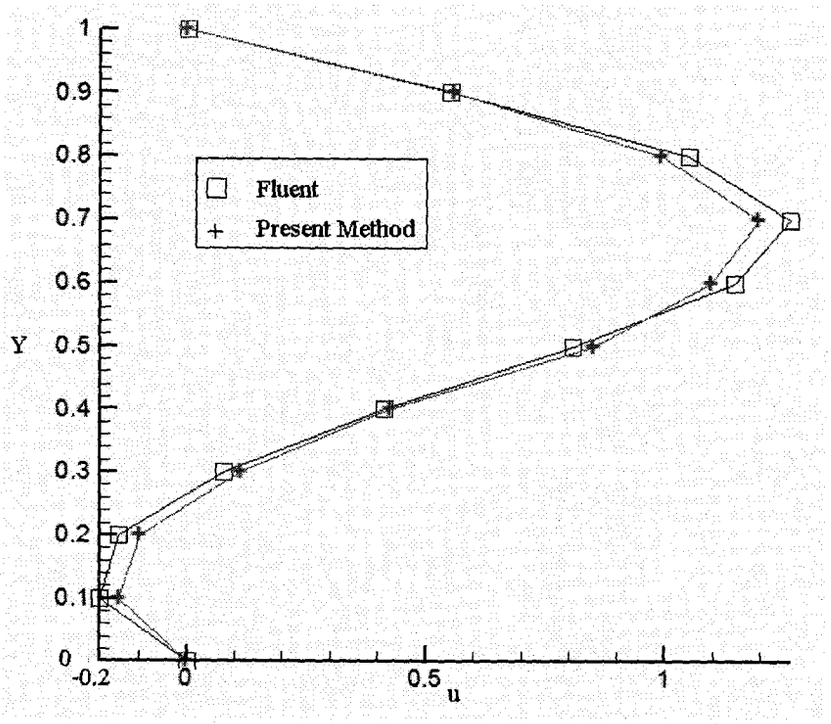

Figure 3.7 u velocity along the vertical line $x = 1.2$

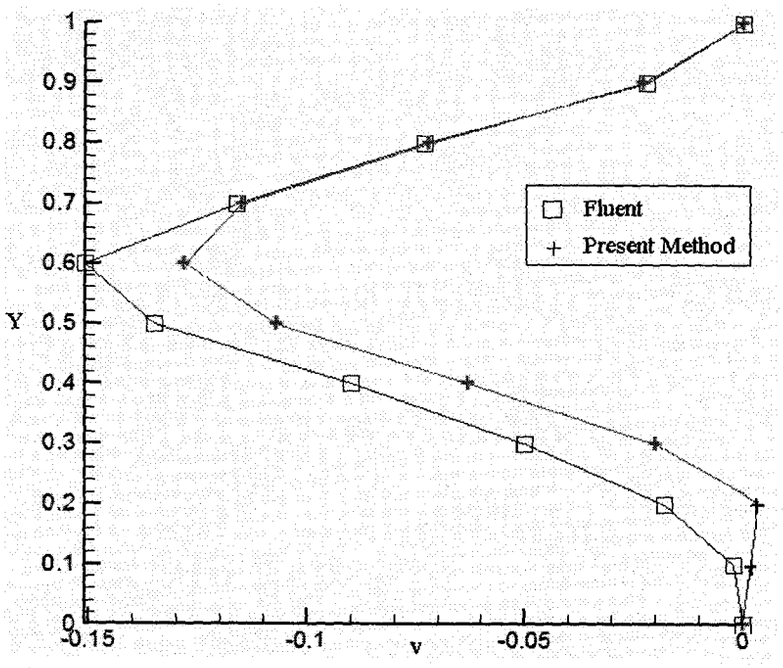

Figure 3.8 v velocity along the vertical line $x = 1.2$

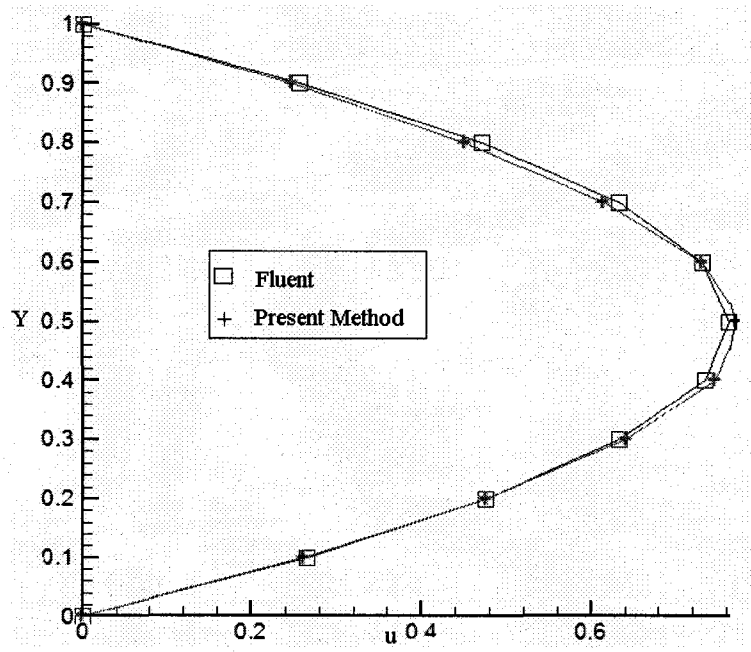

Figure 3.9 u velocity along the vertical line $x = 5$

Pressure contours are compared in Figures 3.10 and 3.11, showing that the contours obtained by FLUENT and the present method are almost identical. Pressure has its minimum values at the inlet and outlet, and its maximum value at the middle of the channel.

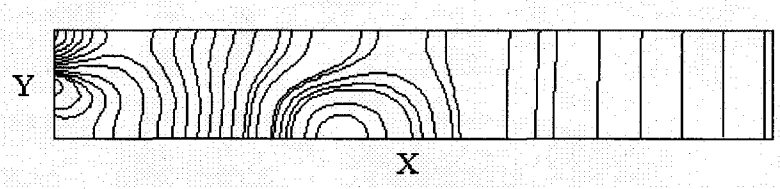

Figure 3.10 Pressure contours for $Re = 200$ using present method

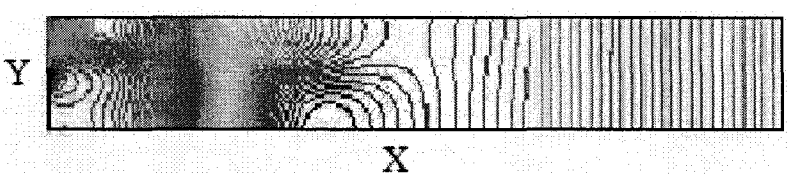

Figure 3.11 Pressure contours for $Re = 200$ using FLUENT

3.3.3 Multiblock Methodology

3.3.3.1 Multiblock Mesh Generation

A multiblock grid is a collection of structured grids that together fill the physical domain. Multiblock grid systems may be rectilinear or curvilinear. The idea behind multiblock mesh generation is that, instead of utilizing one global coordinate system, several local systems are constructed and connected together. The domain is subdivided into blocks and, within each block, a system is derived. The block subdivision provides the necessary flexibility to construct structured meshes for geometrically complex domains. The approach represents a highly effective compromise between a globally structured mesh and an unstructured mesh. In one limit, that of a single block, the global structured mesh is recovered, whilst in the other limit, a fully unstructured mesh of quadrilaterals is obtained. The only lack of flexibility inherent to this latter limit is that the cells or elements are quadrilaterals and are therefore not the lowest geometrical simplex, namely the triangle.

This concept in mesh generation is very powerful. The arrangements of blocks define how the local systems connect and the resulting connectivities between the local coordinate systems define the topology of the grid. Using curvilinear systems, it is possible to construct a wide range of mesh topologies for any given configuration. In particular, it is possible to construct 'component adaptive' mesh topologies to ensure that the mesh lines close to a component are appropriate to the geometrical shape of that component. This is an important aspect of the design and construction of high quality meshes.

The multiblock curvilinear grid system concept is not restricted to any particular mesh point generation technique. The generation of points can be performed using the algebraic or the partial differential equation approach. The block structure is completely independent of any coordinates in the physical space. Each block has its own "local" coordinate system. This system is independent of those in the adjacent blocks. Hence to generate a mesh within a block it is only necessary to construct an algorithm which operates on a simple rectangular computational domain. With a suitable treatment of boundary points, the generation of the global mesh then involves a loop over all the blocks.

A desirable condition for block boundaries to satisfy is that, given two blocks which are adjacent and have a common edge in the block connectivity matrix, the grid lines in physical space, which correspond to points on the edge, must be continuous. Moreover, if a block boundary is adjacent to another block boundary, and the boundary points are fixed, then the resulting mesh will, in general, be discontinuous in gradients and higher derivatives across the boundary. However, slope continuity at block interfaces can be achieved. The transfinite interpolation method provides a mechanism by which slopes at boundaries can be specified. For elliptic grid generation systems, it is possible to manipulate the control functions so as to control the slopes at boundaries.

In this chapter, the present velocity-pressure coupling method is applied to the backward-facing step to test the suitability of the multiblock approach. Note here that this work deals with the solution of the flow equations on a multiblock mesh, rather than the details involved in creating the multiblock mesh.

3.3.3.2 Multiblock Solution for Backward-facing Step

A multiblock mesh for a flow on a Cartesian grid can be illustrated by the two blocks shown in Figure 3.12. To illustrate the methodology and formulate the relevant equations, we have considered a horizontal interface between the two blocks, and specified its location at $j = \frac{J+1}{2}$. A vertical interface would be treated similarly. Due to the staggered grid arrangement in each block, the *u*-momentum and continuity equations can be solved on each block as explained in Chapter 2. However, special treatment must be given to the *v*-momentum equation because the horizontal interface between the blocks is located where *v* is stored. So, in block 1, a relation should be found between *v* stored at the interface, $v_{i,\frac{J+1}{2}}$, and *v* at two grid lines south of the interface, i.e., $v_{i,\frac{J-3}{2}}$. In block 2, the relation should be found between *v* at the interface, $v_{i,\frac{J+1}{2}}$, and *v* at two grid lines north of the interface, i.e., $v_{i,\frac{J+5}{2}}$.

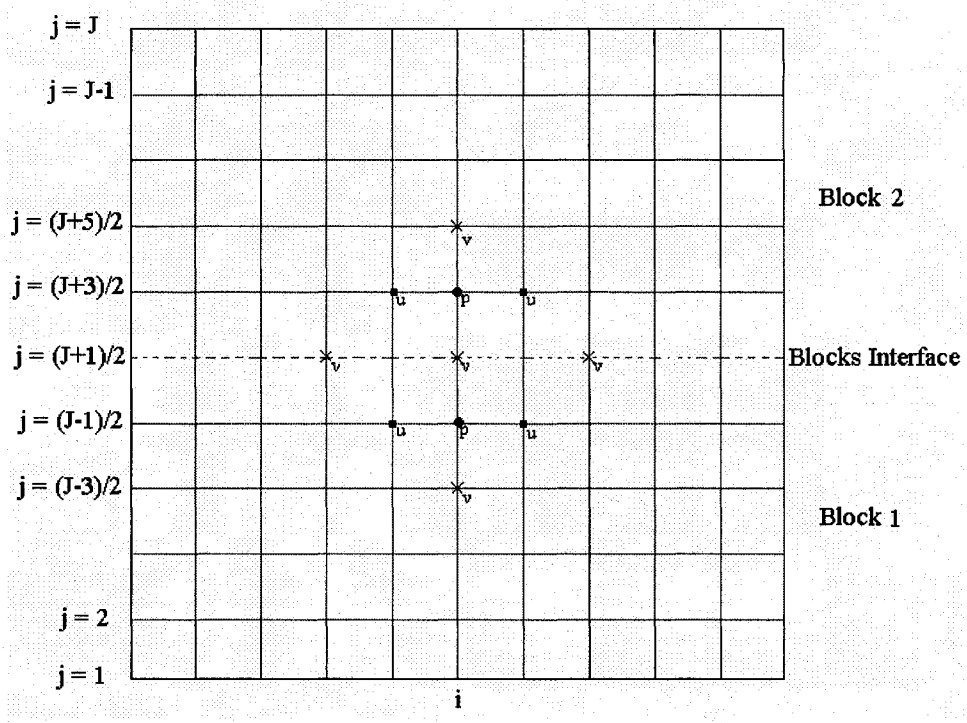

Figure 3.12 Multiblock mesh

In block 1, the continuity equation discretized at $i, \frac{J-1}{2}$, which corresponds to the grid line adjacent to the north boundary of block 1, is

$$\frac{u_{i+1,\frac{J-1}{2}} - u_{i-1,\frac{J-1}{2}}}{2\Delta x} + \frac{v_{i,\frac{J+1}{2}} - v_{i,\frac{J-3}{2}}}{2\Delta y} = 0 \tag{3.3}$$

This equation, written in the form

$$\frac{\Delta y}{\Delta x}\left(u_{i-1,\frac{J-1}{2}} - u_{i+1,\frac{J-1}{2}}\right) + v_{i,\frac{J-3}{2}} = v_{i,\frac{J+1}{2}} \tag{3.4}$$

gives the required relation for block 1. The v-momentum equation in block 1 at the north side (two grid lines south of the interface) becomes

$$b_P^N v_{i,\frac{J-3}{2}} + b_S^N v_{i,\frac{J-7}{2}} + b_W^N v_{i-2,\frac{J-3}{2}} + b_E^N v_{i+2,\frac{J-3}{2}} = \frac{\hat{p}_{i,\frac{J-5}{2}} - \hat{p}_{i,\frac{J-1}{2}}}{2\rho\Delta y} + \hat{S}_u^N \tag{3.5}$$

where

$$\begin{aligned}
b_P^N &= \frac{\hat{u}_{i,\frac{J-3}{2}}}{2\Delta x} + \frac{\hat{v}_{i,\frac{J-3}{2}}}{4\Delta y} + \upsilon\left(\frac{1}{2\Delta x^2} + \frac{1}{4\Delta y^2}\right) \\
b_S^N &= -\frac{\hat{v}_{i,\frac{J-3}{2}}}{4\Delta y} - \frac{\upsilon}{4\Delta y^2} \\
b_W^N &= -\frac{\hat{u}_{i,\frac{J-3}{2}}}{2\Delta x} - \frac{\upsilon}{4\Delta x^2} \\
b_E^N &= -\frac{\upsilon}{4\Delta x^2} \\
\hat{S}_u^S &= \frac{\Delta y}{\Delta x}\left(\frac{\upsilon}{4\Delta y^2} - \frac{\hat{v}_{i,\frac{J-3}{2}}}{4\Delta y}\right)\left(\hat{u}_{i-1,\frac{J-1}{2}} - \hat{u}_{i+1,\frac{J-1}{2}}\right).
\end{aligned} \tag{3.6}$$

A similar discussion as above follows for block 2, where the relation between the v's at the south side (two grid lines north of the interface) is given by

$$\frac{\Delta y}{\Delta x}\left(u_{i+1,\frac{J+3}{2}} - u_{i-1,\frac{J+3}{2}}\right) + v_{i,\frac{J+5}{2}} = v_{i,\frac{J+1}{2}}. \tag{3.7}$$

Note here that the v-equation can be solved in either block first. If v is solved in block 2 first, equation (3.7) is used to evaluate v at the interface. Now, with v known at the interface, block 1 can be treated as discussed in Chapter 2 where v is known at the north boundary (interface).

Flow over the backward-facing step for Re = 100 is considered using the multiblock approach. The flow domain has been divided into two blocks by the horizontal line

emanating from the step corner. Results obtained are essentially identical to those obtained in the case of single block, as seen in Figures 3.14 and 3.15. To further validate the multiblock methodology, an inlet duct has also been added to the flow domain, as illustrated in Figure 3.13, and three blocks are created using horizontal and vertical lines emanating from the step corner. The parabolic inlet flow condition is now applied on the west boundary of block 3. As seen by comparing Figures 3.14, 3.15 and 3.16, the same solution is obtained for the cases of one, two or three blocks.

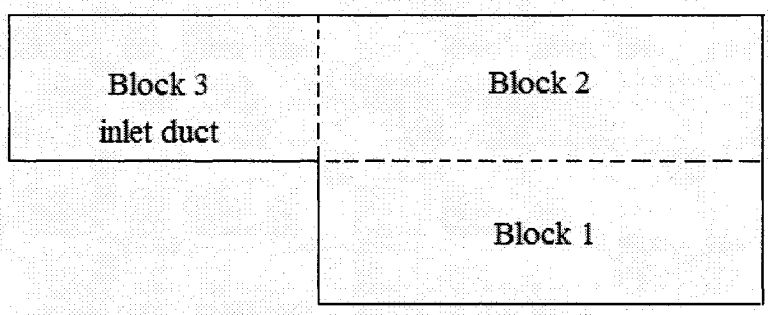

Figure 3.13 Flow domain decomposed into three blocks

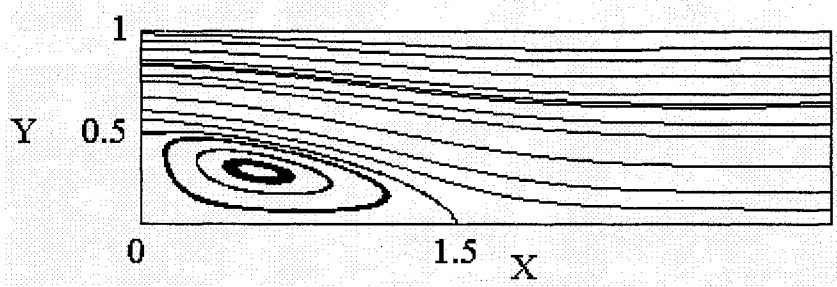

Figure 3.14 Streamlines for *Re* = 100, one block

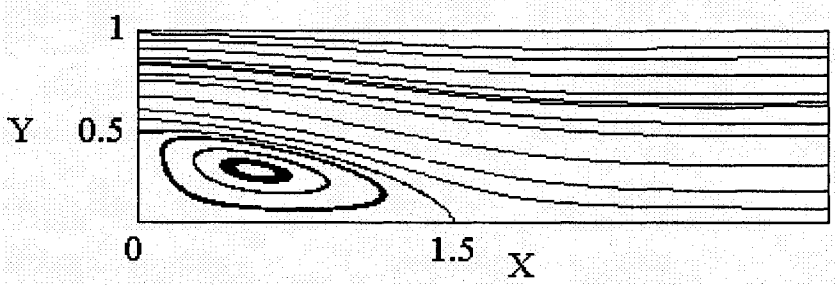

Figure 3.15 Streamlines for *Re* = 100, two blocks

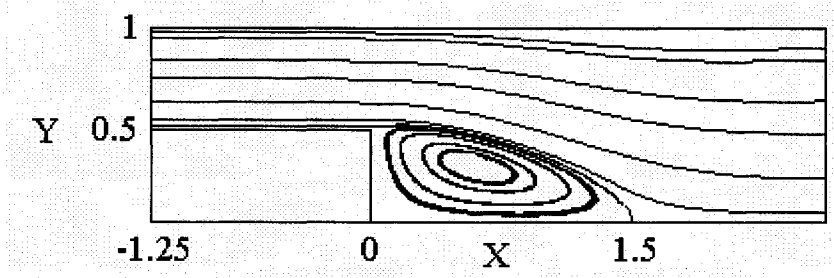

Figure 3.16 Streamlines for *Re* = 100, three blocks

3.4 Flow in a Square Cavity

The problem considered is the two-dimensional viscous flow in a cavity, in which an incompressible fluid is bounded by a square enclosure and the flow is driven by a uniform translation of the top. The fluid motion in this cavity is an example of closed streamline problems that are of theoretical importance because they exhibit the primary features of a broad class of flows, namely steady separated flows. Due to the simplicity of

the cavity geometry, applying a numerical method on this flow problem, in terms of coding, is quite easy and straightforward. However, numerical methods for solving the flow equations are often tested and evaluated on cavity flows because of the complexity of the flow physics.

Despite its simple geometry, the driven cavity flow retains rich fluid flow physics manifested by multiple counter-rotating recirculating regions in the corners of the cavity depending on the Reynolds number. In the literature, different numerical approaches have been applied to the lid-driven cavity flow problem. Though this flow problem has been numerically studied extensively, still there are some points which are not agreed upon (Erturk et al [53]). For example, an interesting point among many studies is that different numerical formulations for the simulation of cavity flow yield about the same results for $Re \leq 1{,}000$, but results start to deviate from each other for larger *Re*. Another interesting point is that while some studies predict a periodic flow at high Reynolds numbers, others present steady solutions. Aydin and Fenner [54] have used a boundary element method formulation with central and upwind finite difference schemes for the convective terms. They have stated that their formulation loses its reliability for Reynolds numbers greater than 1,000. Grigoriev and Dargush [55] have presented a boundary element method solution with an improved penalty function technique using hexagonal subregions, discretizing the integral equation for each subregion as in the finite element method. They have used a non-uniform mesh of 5040 quadrilateral cells. Using this approach they were able to solve driven cavity flow up to $Re = 5{,}000$. Ghia et al [56] used the vorticity-streamfunction formulation to study the effectiveness of the coupled strongly implicit multigrid method in the determination of high *Re* fine mesh flow solutions. They

presented numerical values for the velocity components along vertical and horizontal lines through the geometric centre of the cavity.

3.4.1 Problem Specification and Boundary Conditions

Lid-driven cavity flow is defined as steady incompressible flow in a rectangular domain whose top boundary moves with constant velocity in the plane of the cavity cross-section. Therefore, the flow movement inside the cavity is induced by the top wall of the cavity. The present simulation uses Cartesian coordinates with the origin located at the lower left corner and the top boundary moves from left to right. The fluid velocities on the left, right and bottom sides of the cavity are fixed at zero, while a uniform velocity $u = 1$ is applied along the top wall, as illustrated in Figure 3.17.

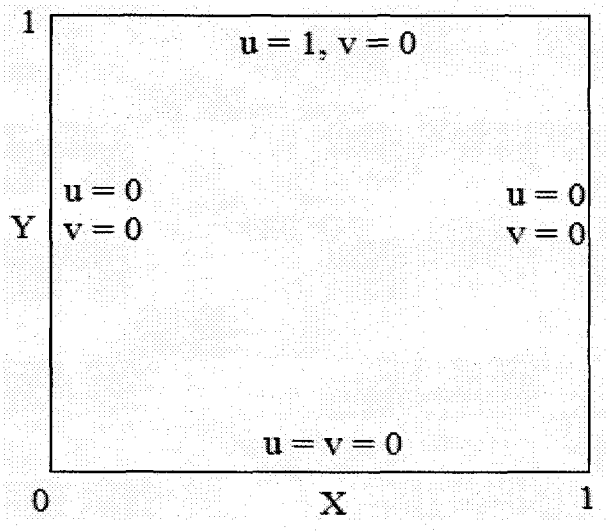

Figure 3.17 Lid-driven cavity

3.4.2 Results and Discussion

Figures 3.18, 3.19 and 3.21 show plots of streamlines for Re = 100, 400 and 1000 obtained using the present method. The flow structure is in excellent agreement with the work of Ghia et al [56], as illustrated by comparing the flow patterns in Figures 3.19 and 3.20.

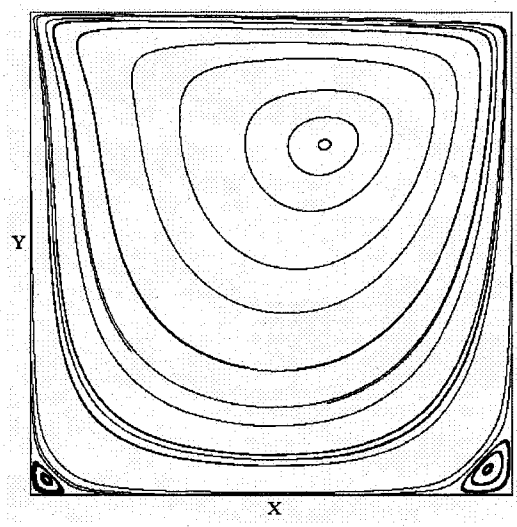

Figure 3.18 Streamlines for Re = 100

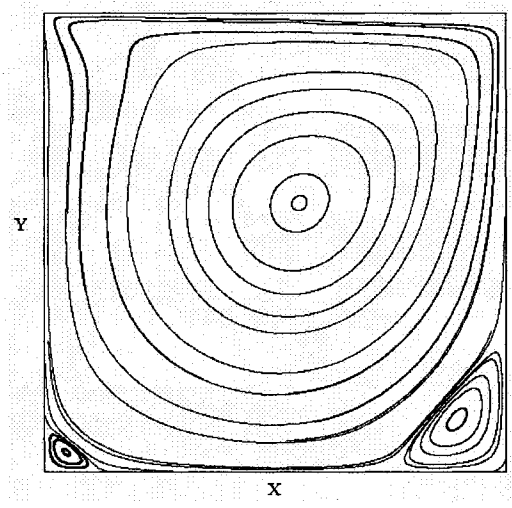

Figure 3.19 Streamlines for Re = 400 using present method

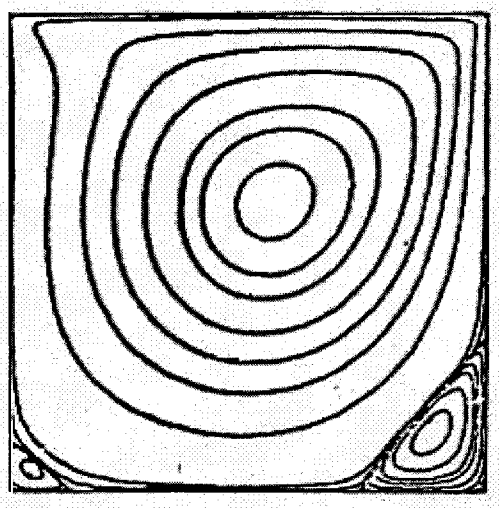

Figure 3.20 Streamlines for $Re = 400$, from Ghia et al [56]

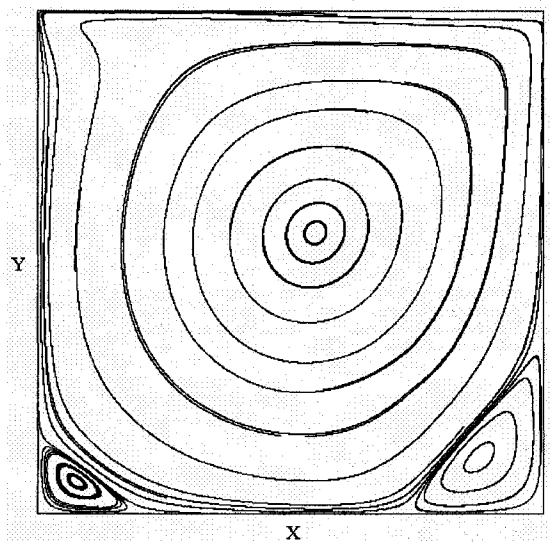

Figure 3.21 Streamlines for $Re = 1000$

The numerical solution for Reynolds number up to 1000 shows a large primary vortex and two secondary vortices in the lower corners, in agreement with results reported by Ghia et al [56] and many other researchers. These streamline plots give a clear picture of the overall flow pattern and the effect of Reynolds number on the structure of the steady recirculating eddies in the cavity. In addition to the primary centre vortex, a pair of

counter-rotating eddies of much smaller strength develop in the lower corners of the cavity. For Re = 10, the centre of the primary vortex is located at the mid-width and about one third of the cavity depth from the top. As Re increases (Re = 100), the primary vortex centre moves toward the right and the vortex becomes increasing circular. Finally, this centre moves down towards the geometric centre of the cavity as the Re increases further. In the case of Re = 100, a 101x101 mesh was created and the results obtained agree very well with those obtained by Ghia et al [56]. A finer mesh, 201x201, was also used for this Re, but no significant change was noticed. The number of iteration needed to satisfy the convergence criterion $\frac{\sum|u_{new}-u_{old}|}{\sum u_{new}}<10^{-3}$ was 11130. In the case of Re = 400, a 201x201 mesh was also used and the number of iteration required for convergence was 16579. When Re = 1000, the solution failed to converge using the same criterion on the 201x201 mesh. The flow equations in this case are solved on a 301x301 mesh with a different convergence criterion $|u_{new}-u_{old}|\leq 10^{-4}$. Figures 3.22 and 3.23 show the u velocity component along the vertical centreline for Re = 100 and 1000, respectively. Figures 3.24 and 3.25 show the v velocity component along the horizontal centreline for Reynolds numbers of 100 and 1000, respectively. The results for Re = 100 are in excellent agreement with those obtained by Ghia et al [56]. For Re = 1000, the u component agrees very well but the v component is not as good as those obtained for lower Re.

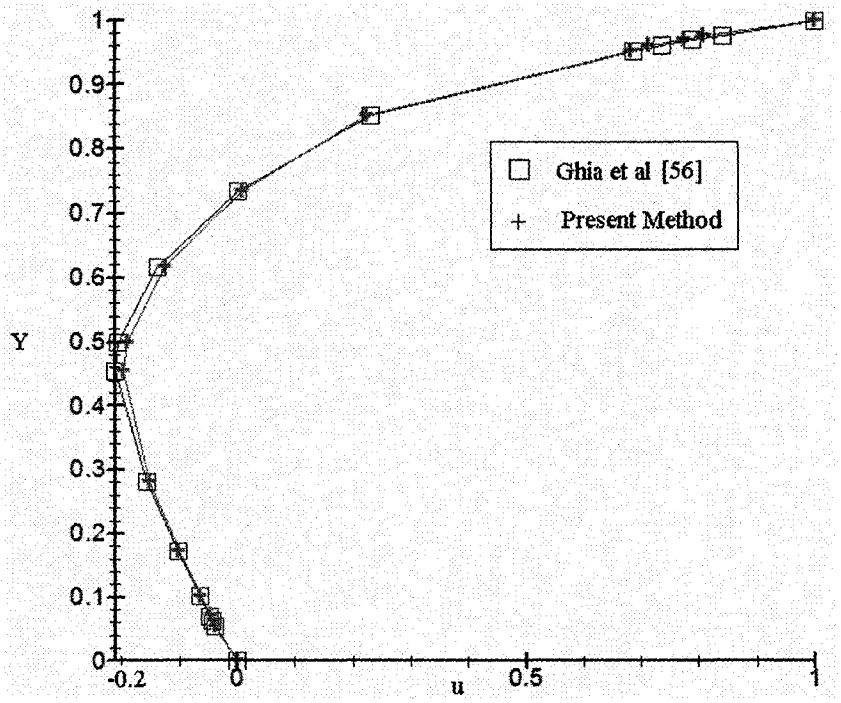

Figure 3.22 *u* velocity along vertical line through geometric centre of cavity for *Re* = 100

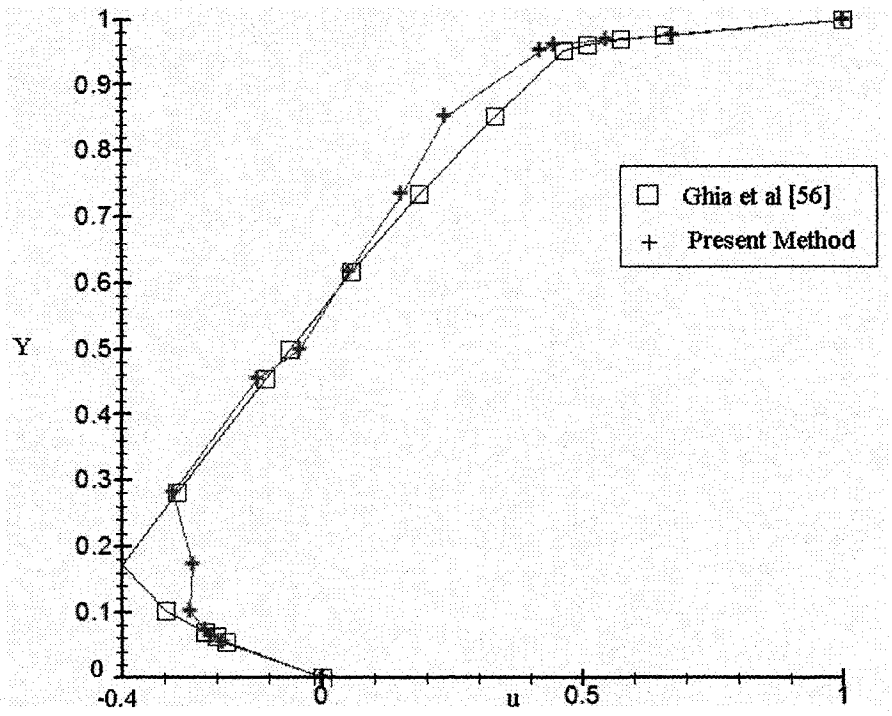

Figure 3.23 *u* velocity along vertical line through geometric centre of cavity for *Re* = 1000

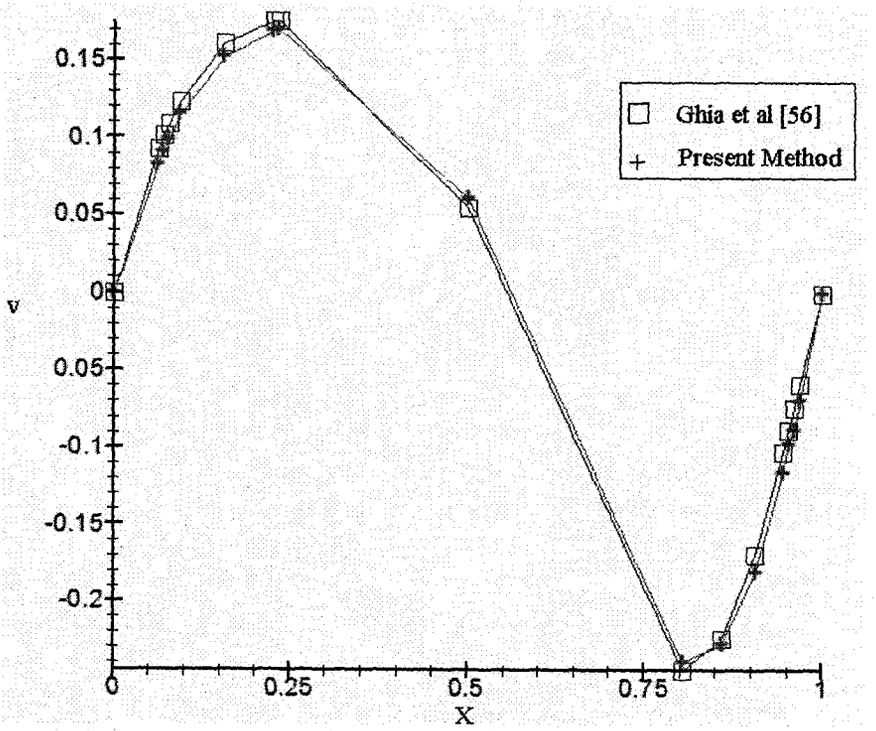

Figure 3.24 v velocity along horizontal line through geometric centre of cavity for $Re = 100$

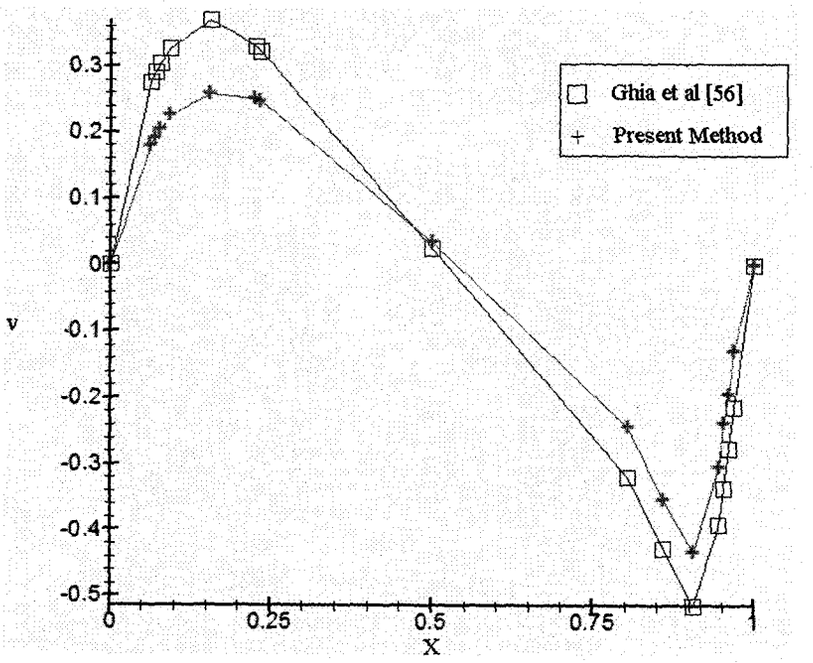

Figure 3.25 v velocity along horizontal line through geometric centre of cavity for $Re = 1000$

Results obtained for Re = 400 are also compared to those obtained by using FLUENT. Figures 3.26 and 3.27 show the u velocity along the vertical line and v velocity along the horizontal line through the geometric centre of the cavity, respectively.

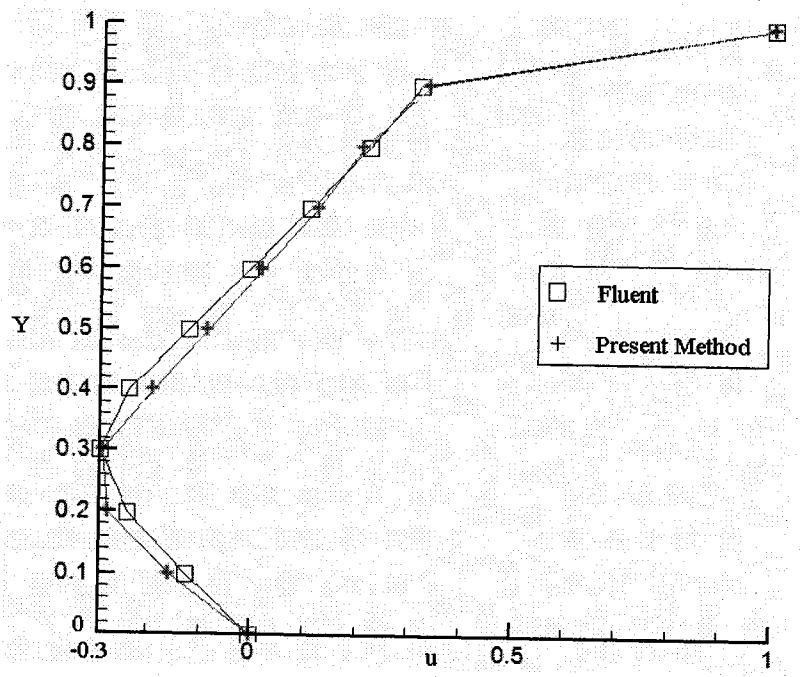

Figure 3.26 u velocity along vertical line through geometric centre of cavity for Re = 400

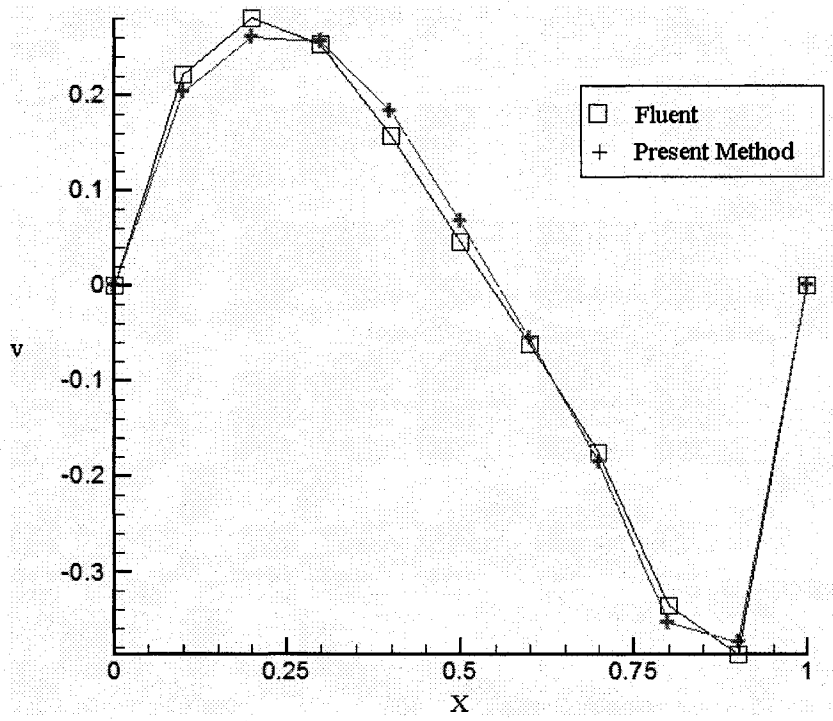

Figure 3.27 v velocity along horizontal line through geometric centre of cavity for $Re = 400$

Pressure contours are compared in Figures 3.28 and 3.29, showing that the contours are almost identical. Pressure has its maximum value at the right top corner of the cavity. The results for velocity and pressure obtained from the present method and from FLUENT are in very good agreement.

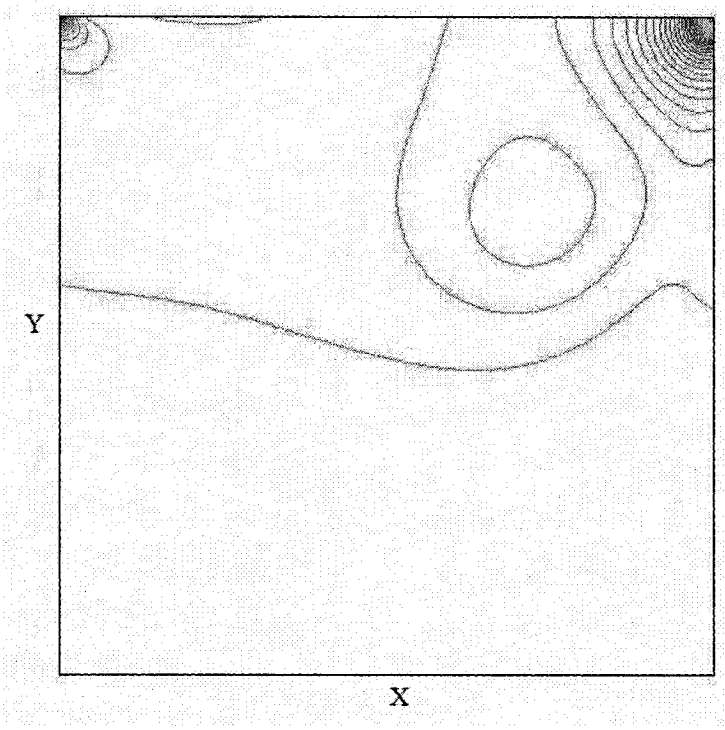

Figure 3.28 Pressure contours from FLUENT, $Re = 400$

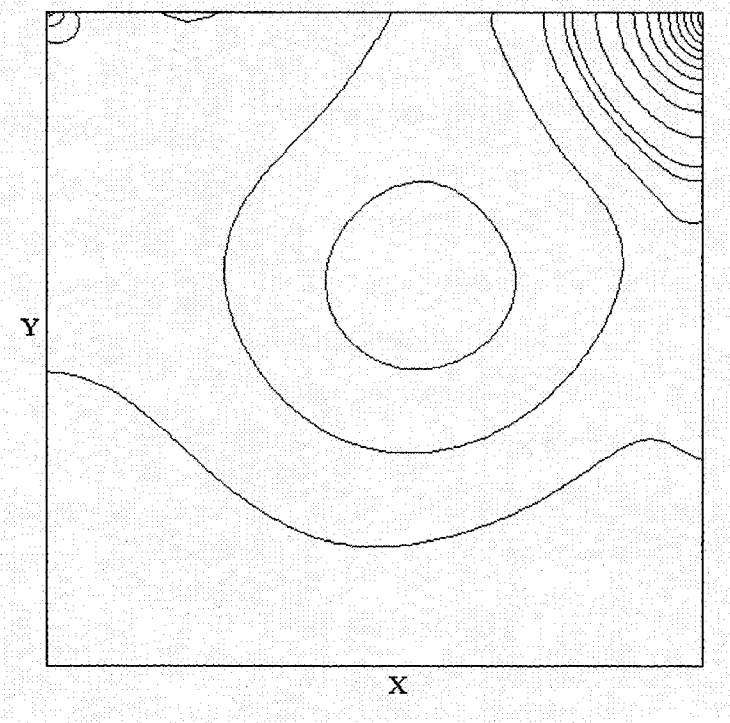

Figure 3.29 Pressure contours from present method, $Re = 400$

3.5 Conclusions

The proposed method has first been tested on a simple problem that has an exact solution in the downstream region, specifically flow in a straight duct. The results obtained for various Reynolds numbers are in excellent agreement with the exact solution and other numerical results in the fully developed region.

The two-dimensional lid-driven cavity flow and the flow over a backward-facing step at various Reynolds numbers have been simulated using the proposed method. Numerical results are compared with benchmark solutions, FLUENT simulations and experimental data.

In the case of the backward-facing step, predictions from the present numerical model have been compared against experimental data for low Reynolds number. In addition, computed reattachment lengths have been compared against alternative numerical predictions and experimental measurements. Reattachment length for various *Re* and the velocity components for $Re = 200$ across vertical lines in the separation region and downstream are compared to those obtained by FLUENT. The proposed method is found to give realistic flow predictions and the results are found to be in excellent agreement with the results published by Armaly et al [50], Barton [49], Barber and Fonty [51] and FLUENT.

For cavity flow, results for Reynolds number up to 1000 are reported. At higher Reynolds number the results differ among researchers depending on the methods and schemes used to solve the flow equations. FLUENT is also used for $Re = 400$ to compare pressure contours and velocities across centrelines. The results obtained are in excellent agreement with those reported in the literature and with FLUENT results.

CHAPTER IV

DISCRETIZED FLOW EQUATIONS ON A STAGGERED CURVILINEAR GRID

4.1 Introduction

Analytical and numerical methods for the generation of body-fitted coordinate systems have been developed for the solution of flow problems on complex geometries. The most commonly used method for the generation of smooth grids is elliptic grid generation, where an elliptic system of partial differential equations in the form (for 2D)

$$\begin{aligned} \xi_{xx} + \xi_{yy} &= P(\xi,\eta) \\ \eta_{xx} + \eta_{yy} &= Q(\xi,\eta) \end{aligned} \tag{4.1}$$

is solved. The "control functions" P and Q can be fashioned to control the spacing and orientation of the coordinate lines. Several techniques have been developed concerning the selection of these control functions. Some of these methods are introduced below.

Thompson et al [57] developed one of the most commonly used elliptic grid generation systems. They proposed expressions for P and Q in terms of exponential functions. These functions contain several amplitude, decay and location parameters which can be adjusted to control the degree of clustering or repulsion from particular points or lines in the mesh system. Amplitude and decay factors must be tuned to achieve good gridding. This is even more cumbersome when a multiblock approach is used since these parameters may have to be changed from one block to another. Steger and Sorenson [58] improved on the Thompson et al [57] formulation by imposing the additional requirement of orthogonality at a domain boundary. The constant amplitudes in the exponential functions are replaced by functions of one variable along a boundary. In addition to decay factors which have to

be properly specified, P and Q must be under-relaxed to achieve convergence. Thomas and Middlecoff [59] used a reformulated version of the grid generation equations, and assumed that the ξ= constant curves are straight as they leave the boundary. In this case the expressions for P and Q can be determined iteratively from the boundary data and interpolation to the interior. Barron [60] solved the same system of equations with different control functions to enhance orthogonality of the mesh near the boundaries. In fact, with this method, only the boundary data and interpolation are required to determine P and Q explicitly. This method is capable of generating high quality structured mesh systems at a relatively low cost. It is especially useful when multiblock grid generation is required since it imposes orthogonality at block interfaces, and it is straightforward and easy to implement. The only input required into the system is the boundary data for each block. Unlike most other schemes which attempt to ensure some degree of orthogonality, this method does not require user input of amplitude and decay factors, or additional relaxation parameters. The control functions are evaluated explicitly and non-iteratively from the boundary data, making the system completely automated. In this thesis, Barron's approach [60] is followed to generate the meshes.

We note that equations (4.1) are not convenient to solve since they are expressed in the physical (x, y) domain. Thus, equations (4.1) are transformed to the (ξ,η) computational domain, resulting in the elliptic system

$$\begin{aligned}
\left(x_\eta^2+y_\eta^2\right)x_{\xi\xi}-2\left(x_\xi x_\eta+y_\xi y_\eta\right)x_{\xi\eta}+\left(x_\xi^2+y_\xi^2\right)x_{\eta\eta}&=-J^2\left(Px_\xi+Qx_\eta\right)\\
\left(x_\eta^2+y_\eta^2\right)y_{\xi\xi}-2\left(x_\xi x_\eta+y_\xi y_\eta\right)y_{\xi\eta}+\left(x_\xi^2+y_\xi^2\right)y_{\eta\eta}&=-J^2\left(Py_\xi+Qy_\eta\right)
\end{aligned} \tag{4.2}$$

where J is the transformation Jacobian.

These equations are solved to give

$$x_{i,j} = x(\xi_i, \eta_j) = x(i, j)$$

$$y_{i,j} = y(\xi_i, \eta_j) = y(i, j)$$

where we have set $\Delta\xi = \Delta\eta = 1$ so that $\xi_i = i$ and $\eta_j = j$.

The Navier-Stokes equations for the two-dimensional, steady, incompressible, viscous flow in terms of curvilinear coordinates (ξ, η), in the non-conservative dimensional form, are

$$\xi_x u_\xi + \eta_x u_\eta + \xi_y v_\xi + \eta_y v_\eta = 0 \tag{4.3}$$

$$\left(u\xi_x + v\xi_y\right) u_\xi + \left(u\eta_x + v\eta_y\right) u_\eta = -\frac{\xi_x}{\rho} p_\xi - \frac{\eta_x}{\rho} p_\eta + \upsilon\left\{\left(\xi_x^2 + \xi_y^2\right) u_{\xi\xi} + \left(\eta_x^2 + \eta_y^2\right) u_{\eta\eta} + 2\left(\xi_x\eta_x + \xi_y\eta_y\right) u_{\xi\eta} + \left(\xi_{xx} + \xi_{yy}\right) u_\xi + \left(\eta_{xx} + \eta_{yy}\right) u_\eta\right\} \tag{4.4}$$

$$\left(u\xi_x + v\xi_y\right) v_\xi + \left(u\eta_x + v\eta_y\right) v_\eta = -\frac{\xi_y}{\rho} p_\xi - \frac{\eta_y}{\rho} p_\eta + \upsilon\left\{\left(\xi_x^2 + \xi_y^2\right) v_{\xi\xi} + \left(\eta_x^2 + \eta_y^2\right) v_{\eta\eta} + 2\left(\xi_x\eta_x + \xi_y\eta_y\right) v_{\xi\eta} + \left(\xi_{xx} + \xi_{yy}\right) v_\xi + \left(\eta_{xx} + \eta_{yy}\right) v_\eta\right\} \tag{4.5}$$

where u and v are now the velocity components in the ξ and η direction respectively, ξ_x, ξ_y, η_x and η_y are the metrics of transformation [61].

The momentum equations (4.4) and (4.5) form a system of second order partial differential equations which is elliptic in nature. The unknowns in these equations are velocity and pressure.

The metrics of the transformation appearing as coefficients in the flow equations (4.3)-(4.5) are given by

$$\xi_x = \frac{y_\eta}{J}$$

$$\eta_x = -\frac{y_\xi}{J}$$

$$\xi_y = -\frac{x_\eta}{J}$$

$$\eta_y = \frac{x_\xi}{J}$$

where

$$J = \frac{\partial(x,y)}{\partial(\xi,\eta)} = x_\xi y_\eta - x_\eta y_\xi . \tag{4.6}$$

These metrics are known quantities once the solution of the grid generation equations (4.2) has been obtained.

4.2 Finite Differencing on a Curvilinear Staggered Grid

The values of the metrics of the transformation are required at each grid point. Since the step sizes in the computational domain are equally spaced $(\Delta\xi = \Delta\eta = 1)$, x_ξ , x_η, y_ξ, y_η, $x_{\xi\xi}$, $x_{\eta\eta}$, $y_{\xi\xi}$, $y_{\eta\eta}$, $y_{\eta\xi}$ and $x_{\eta\xi}$ can be easily computed by various finite difference approximations. A second order central difference is used in this thesis to approximate these metrics at all interior nodes, i.e., at all interior *u*-nodes, *v*-nodes and *p*-nodes. At the nodes adjacent to the boundaries, forward or backward second order differencing is used depending on the location of the boundary nodes. These approximations at interior nodes are

$$x_{\xi}^{\text{int}}\Big|_{i,j} \approx \frac{x_{i+1,j} - x_{i-1,j}}{2}$$

$$x_{\eta}^{\text{int}}\Big|_{i,j} \approx \frac{x_{i,j+1} - x_{i,j-1}}{2}$$

$$x_{\xi\xi}^{\text{int}}\Big|_{i,j} \approx x_{i-1,j} - 2x_{i,j} + x_{i+1,j}$$

$$x_{\eta\eta}^{\text{int}}\Big|_{i,j} \approx x_{i,j-1} - 2x_{i,j} + x_{i,j+1}$$

$$x_{\xi\eta}^{\text{int}}\Big|_{i,j} \approx \frac{x_{i+1,j+1} - x_{i+1,j-1} - x_{i-1,j+1} + x_{i-1,j-1}}{4}, \tag{4.7}$$

and similar expressions for derivatives of y.

4.3 Discretization of the Momentum Equations

A staggered grid is used to store the velocity components u and v and the pressure p. The velocity components u and v are stored at the *i-1,j* and *i,j+1* locations respectively and p is stored at *i,j*. The first order backward difference of the convective terms in equations (4.4) and (4.5), in the ξ direction, are given by

$$u_{\xi}\Big|_{i-1,j} \approx \frac{u_{i-1,j} - u_{i-3,j}}{2}$$

$$v_{\xi}\Big|_{i,j+1} \approx \frac{v_{i,j+1} - v_{i-2,j+1}}{2}.$$

Note that these differences are expressed in terms of nodes at which the particular variable is stored, which means that the spacing between u-nodes is $2\Delta\xi$.

The second order central difference of the convective terms in the η direction are given by

$$u_\eta\Big|_{i-1,j} \approx \frac{u_{i-1,j+2} - u_{i-1,j-2}}{4}$$

$$v_\eta\Big|_{i,j+1} \approx \frac{v_{i,j+3} - v_{i,j-1}}{4}.$$

The diffusion terms in the flow equations are represented using second order accurate central differences, given by

$$u_{\xi\xi}\Big|_{i-1,j} \approx \frac{u_{i-3,j} - 2u_{i-1,j} + u_{i+1,j}}{4}$$

$$v_{\xi\xi}\Big|_{i,j+1} \approx \frac{v_{i-2,j+1} - 2v_{i,j+1} + v_{i+2,j+1}}{4}$$

$$u_{\eta\eta}\Big|_{i-1,j} \approx \frac{u_{i-1,j+2} - 2u_{i-1,j} + u_{i-1,j-2}}{4}$$

$$v_{\eta\eta}\Big|_{i,j+1} \approx \frac{v_{i,j+3} - 2v_{i,j+1} + v_{i,j-1}}{4}.$$

In equation (4.4), convective-like terms involving u_ξ and u_η appear on the right hand side. However, these arise due to the transformation of the diffusion terms. Therefore, these terms are central differenced instead of backward differenced, giving

$$u_\xi\Big|_{i-1,j} \approx \frac{u_{i+1,j} - u_{i-3,j}}{4}.$$

A similar discussion holds for the v_ξ and v_η terms in the v-momentum equation (4.5). Therefore,

$$v_\xi\Big|_{i,j+1} \approx \frac{v_{i+2,j+1} - v_{i-2,j+1}}{4}.$$

The mixed derivative of u and v are central differenced to give, respectively

$$u_{\xi\eta}\Big|_{i-1,j} \approx \frac{u_{i+1,j+2} - u_{i-3,j+2} - u_{i+1,j-2} + u_{i-3,j-2}}{16}$$

$$v_{\xi\eta}\Big|_{i,j+1} \approx \frac{v_{i+2,j+3} - v_{i-2,j+3} - v_{i+2,j-1} + v_{i-2,j-1}}{16}.$$

The pressure gradients are approximated by second order accurate central differences using the locations where p is defined. This gives

$$p_{\xi}\Big|_{i-1,j} \approx \frac{p_{i,j} - p_{i-2,j}}{2}$$

$$p_{\eta}\Big|_{i-1,j} \approx \frac{p_{i-2,j+2} + p_{i,j+2} - p_{i-2,j-2} - p_{i,j-2}}{8}$$

$$p_{\xi}\Big|_{i,j+1} \approx \frac{p_{i+2,j+2} + p_{i+2,j} - p_{i-2,j} - p_{i-2,j+2}}{8}$$

$$p_{\eta}\Big|_{i,j+1} \approx \frac{p_{i,j+2} - p_{i,j}}{2}.$$

4.3.1 Discretized Equations at Interior Nodes

The discrete u- and v- momentum equations at interior nodes may be written respectively as

$$a_P^{\text{int}} u_{i-1,j} + a_N^{\text{int}} u_{i-1,j+2} + a_S^{\text{int}} u_{i-1,j-2} + a_W^{\text{int}} u_{i-3,j} + a_E^{\text{int}} u_{i+1,j} = \xi_x \frac{\hat{p}_{i-2,j} - \hat{p}_{i,j}}{2\rho} + \hat{S}_u^{\text{int}} \qquad (4.8)$$

$$b_P^{\text{int}} v_{i,j+1} + b_N^{\text{int}} v_{i,j+3} + b_S^{\text{int}} v_{i,j-1} + b_W^{\text{int}} v_{i-2,j+1} + b_E^{\text{int}} v_{i+2,j+1} = \eta_y \frac{\hat{p}_{i,j} - \hat{p}_{i,j+2}}{2\rho} + \hat{S}_v^{\text{int}} \qquad (4.9)$$

where

$$\hat{S}_u^{\text{int}} = \frac{\eta_x \left(\hat{p}_{i-2,j-2} + \hat{p}_{i,j-2} - \hat{p}_{i-2,j+2} - \hat{p}_{i,j+2}\right)}{8\rho} + \upsilon \left(\frac{\xi_x \eta_x + \xi_y \eta_y}{8}\right) \left(\hat{u}_{i+1,j+2} - \hat{u}_{i-3,j+2} - \hat{u}_{i+1,j-2} + \hat{u}_{i-3,j-2}\right)$$

$$\hat{S}_v^{\text{int}} = -\frac{\xi_y\left(\hat{p}_{i+2,j+2} + \hat{p}_{i+2,j} - \hat{p}_{i-2,j} - \hat{p}_{i-2,j+2}\right)}{8\rho} + \upsilon\left(\frac{\xi_x\eta_x + \xi_y\eta_y}{8}\right)\left(\hat{v}_{i+2,j+3} - \hat{v}_{i-2,j+3} - \hat{v}_{i+2,j-1} + \hat{v}_{i-2,j-1}\right)$$

$$a_P^{\text{int}} = \frac{\xi_x\hat{u}_{i-1,j}}{2} + \frac{\xi_y\hat{v}_{i-1,j}}{2} + \upsilon\left(\frac{\eta_x^2+\eta_y^2}{2}\right) + \upsilon\left(\frac{\xi_x^2+\xi_y^2}{2}\right)$$

$$a_N^{\text{int}} = \frac{\eta_x\hat{u}_{i-1,j}}{4} + \frac{\eta_y\hat{v}_{i-1,j}}{4} - \upsilon\left(\frac{\eta_x^2+\eta_y^2}{4}\right) - \upsilon\left(\frac{\eta_{xx}+\eta_{yy}}{4}\right)$$

$$a_S^{\text{int}} = -\frac{\eta_x\hat{u}_{i-1,j}}{4} - \frac{\eta_y\hat{v}_{i-1,j}}{4} - \upsilon\left(\frac{\eta_x^2+\eta_y^2}{4}\right) + \upsilon\left(\frac{\eta_{xx}+\eta_{yy}}{4}\right)$$

$$a_W^{\text{int}} = -\frac{\xi_x\hat{u}_{i-1,j}}{2} - \frac{\xi_y\hat{v}_{i-1,j}}{2} - \upsilon\left(\frac{\xi_x^2+\xi_y^2}{4}\right) + \upsilon\left(\frac{\xi_{xx}+\xi_{yy}}{4}\right)$$

$$a_E^{\text{int}} = -\upsilon\left(\frac{\xi_x^2+\xi_y^2}{4}\right) - \upsilon\left(\frac{\xi_{xx}+\xi_{yy}}{4}\right)$$

$$b_P^{\text{int}} = \frac{\xi_x\hat{u}_{i,j+1}}{2} + \frac{\xi_y\hat{v}_{i,j+1}}{2} + \upsilon\left(\frac{\eta_x^2+\eta_y^2}{2}\right) + \upsilon\left(\frac{\xi_x^2+\xi_y^2}{2}\right)$$

$$b_N^{\text{int}} = \frac{\eta_x\hat{u}_{i,j+1}}{4} + \frac{\eta_y\hat{v}_{i,j+1}}{4} - \upsilon\left(\frac{\eta_x^2+\eta_y^2}{4}\right) - \upsilon\left(\frac{\eta_{xx}+\eta_{yy}}{4}\right)$$

$$b_S^{\text{int}} = -\frac{\eta_x\hat{u}_{i,j+1}}{4} - \frac{\eta_y\hat{v}_{i,j+1}}{4} - \upsilon\left(\frac{\eta_x^2+\eta_y^2}{4}\right) + \upsilon\left(\frac{\eta_{xx}+\eta_{yy}}{4}\right)$$

$$b_W^{\text{int}} = -\frac{\xi_x\hat{u}_{i,j+1}}{2} - \frac{\xi_y\hat{v}_{i,j+1}}{2} - \upsilon\left(\frac{\xi_x^2+\xi_y^2}{4}\right) + \upsilon\left(\frac{\xi_{xx}+\xi_{yy}}{4}\right)$$

$$b_E^{\text{int}} = -\upsilon\left(\frac{\xi_x^2+\xi_y^2}{4}\right) - \upsilon\left(\frac{\xi_{xx}+\xi_{yy}}{4}\right). \qquad (4.10)$$

The hat over p, u and v means that these quantities are evaluated at the previous iteration. Because of the use of a staggered grid, the values of the v-velocity in the u-momentum equation and the u-velocity in the v-momentum equation, appearing as coefficients of the convective derivatives, are not available at the desired points. These velocities were computed using the four surrounding grid points, i.e.

$$u\big|_{i,j+1} \approx \frac{u_{i+1,j} + u_{i+1,j+2} + u_{i-1,j} + u_{i-1,j+2}}{4}$$

$$v\big|_{i-1,j} \approx \frac{v_{i,j-1} + v_{i,j+1} + v_{i-2,j-1} + v_{i-2,j+1}}{4}.$$

4.3.2 Discretized Equations at the Boundaries

The problems considered in Chapter 5, solved using curvilinear coordinates, involve an inlet flow or wall jet at the west boundary, outlet flow at the east boundary, stationary wall at the south boundary and symmetry at the north boundary. The discussions regarding velocities presented in Chapter 2 are valid here, except for the north boundary which was previously identified as a wall. It is important to note that the u-and v-momentum equations have an extra term involving pressure, incorporated into the source terms $\hat{S}_u$ and $\hat{S}_v$, due to the transformation. Therefore, special attention must be given to approximate these pressure gradients.

4.3.2.1 Equations at the South Boundary

The pressure gradients $\frac{\partial p}{\partial \eta}$ and $\frac{\partial p}{\partial \xi}$ appear in the source terms for the u- and v-momentum equations, respectively. Various schemes can be applied to evaluate these pressure gradients at near-boundary nodes, for example, the projection method [62]. In

this thesis, a one-sided difference is used to approximate the term $\frac{\partial p}{\partial \eta}$ for the *u*-momentum equation at nodes adjacent to the south boundary, i.e., $j = 2$ nodes. Therefore, we take

$$\left.\frac{\partial p}{\partial \eta}\right|_{i-1,2} \approx \frac{p_{i-2,4} + p_{i,4} - p_{i,2} - p_{i-2,2}}{4}.$$

The *u*-momentum equation along $j = 2$ becomes

$$a_P^S u_{i-1,2} + a_N^S u_{i-1,4} + a_W^S u_{i-3,2} + a_E^S u_{i+1,2} = \xi_x \frac{\hat{p}_{i-2,2} - \hat{p}_{i,2}}{2\rho} + \hat{S}_u^S$$

where

$$\hat{S}_u^S = \frac{\eta_x\left(\hat{p}_{i,2} + \hat{p}_{i-2,2} - \hat{p}_{i-2,4} - \hat{p}_{i,4}\right)}{4\rho} + \upsilon\left(\frac{\xi_x\eta_x + \xi_y\eta_y}{12}\right)\left(\hat{u}_{i+1,4} - \hat{u}_{i-3,4} + 4\hat{u}_{i-3,1} - 4\hat{u}_{i+1,1}\right) + \hat{u}_{i-1,1}\left[\frac{2\eta_x\hat{u}_{i-1,2}}{3} + \frac{2\eta_y\hat{v}_{i-1,2}}{3} + \frac{2\upsilon}{3}\left(\eta_x^2 + \eta_y^2\right) - \frac{2\upsilon}{3}\left(\eta_{xx} + \eta_{yy}\right)\right]$$

$$a_P^S = \frac{\hat{u}_{i-1,2}}{2}\left(\xi_x + \eta_x\right) + \frac{\hat{v}_{i-1,2}}{2}\left(\xi_y + \eta_y\right) + \upsilon\left(\eta_x^2 + \eta_y^2\right) + \upsilon\left(\frac{\xi_x^2 + \xi_y^2}{2}\right) - \upsilon\left(\frac{\eta_{xx} + \eta_{yy}}{2}\right)$$

$$a_N^S = \frac{\eta_x\hat{u}_{i-1,2}}{6} + \frac{\eta_y\hat{v}_{i-1,2}}{6} - \upsilon\left(\frac{\eta_x^2 + \eta_y^2}{3}\right) - \upsilon\left(\frac{\eta_{xx} + \eta_{yy}}{6}\right)$$

$$a_W^S = -\frac{\xi_x\hat{u}_{i-1,2}}{2} - \frac{\xi_y\hat{v}_{i-1,2}}{2} - \upsilon\left(\frac{\xi_x^2 + \xi_y^2}{4}\right) + \upsilon\left(\frac{\xi_{xx} + \xi_{yy}}{4}\right) + \upsilon\left(\frac{\xi_x\eta_x + \xi_y\eta_y}{4}\right)$$

$$a_E^S = -\upsilon\left(\frac{\xi_x^2 + \xi_y^2}{4}\right) - \upsilon\left(\frac{\xi_{xx} + \xi_{yy}}{4}\right) - \upsilon\left(\frac{\xi_x\eta_x + \xi_y\eta_y}{4}\right).$$

The pressure gradient $\frac{\partial p}{\partial \xi}$ in the *v*-momentum equation does not need special treatment, so the *v*-momentum equation at this boundary is the same as at the interior points, except that the velocity components at this boundary are known.

4.3.2.2 Equations at the North Boundary

As previously mentioned, the boundary condition applied at the north boundary of the physical domain is the flow symmetry boundary condition, i.e. $\frac{\partial u}{\partial y} = 0$ and $v = 0$. Since this north boundary is also a flow symmetry boundary in the computational domain, this condition becomes $\frac{\partial u}{\partial \eta} = 0$ and $v = 0$ along $j = J$. A one-sided difference is used to approximate the term $\frac{\partial p}{\partial \eta}$. Therefore, we take

$$\left.\frac{\partial p}{\partial \eta}\right|_{i-1,J-1} \approx \frac{p_{i,J-1} + p_{i-2,J-1} - p_{i-2,J-3} - p_{i,J-3}}{4}$$

where J is the maximum number of nodes in the η direction. The *u*-momentum equation along $j = J-1$ becomes

$$a_P^N u_{i-1,J-1} + a_S^N u_{i-1,J-3} + a_W^N u_{i-3,J-1} + a_E^N u_{i+1,J-1} = \xi_x \frac{\hat{p}_{i-2,J-1} - \hat{p}_{i,J-1}}{2\rho} + \hat{S}_u^N$$

where

$$\hat{S}_u^N = \frac{\eta_x\left(\hat{p}_{i,J-3} + \hat{p}_{i-2,J-3} - \hat{p}_{i-2,J-1} - \hat{p}_{i,J-1}\right)}{4\rho} + \upsilon\left(\frac{\xi_x\eta_x + \xi_y\eta_y}{12}\right)\left(\hat{u}_{i-3,J-3} - \hat{u}_{i+1,J-3}\right)$$

$$a_P^N = \hat{u}_{i-1,J-1}\left(\frac{\xi_x}{2} + \frac{\eta_x}{6}\right) + \hat{v}_{i-1,J-1}\left(\frac{\xi_y}{2} + \frac{\eta_y}{6}\right) + \upsilon\left(\frac{\eta_x^2 + \eta_y^2}{3}\right) + \upsilon\left(\frac{\xi_x^2 + \xi_y^2}{2}\right) - \upsilon\left(\frac{\eta_{xx} + \eta_{yy}}{6}\right)$$

$$a_W^N = -\frac{\xi_x \hat{u}_{i-1,J-1}}{2} - \frac{\xi_y \hat{v}_{i-1,J-1}}{2} - \upsilon\left(\frac{\xi_x^2 + \xi_y^2}{4}\right) + \upsilon\left(\frac{\xi_{xx} + \xi_{yy}}{4}\right) + \upsilon\left(\frac{\xi_x \eta_x + \xi_y \eta_y}{12}\right)$$

$$a_E^N = -\upsilon\left(\frac{\xi_x^2 + \xi_y^2}{4}\right) - \upsilon\left(\frac{\xi_{xx} + \xi_{yy}}{4}\right) - \upsilon\left(\frac{\xi_x \eta_x + \xi_y \eta_y}{12}\right)$$

$$a_S^N = -\frac{\eta_x \hat{u}_{i-1,J-1}}{6} - \frac{\eta_y \hat{v}_{i-1,J-1}}{6} - \upsilon\left(\frac{\eta_x^2 + \eta_y^2}{3}\right) + \upsilon\left(\frac{\eta_{xx} + \eta_{yy}}{6}\right).$$

The v-momentum equation at this boundary is the same as at the interior nodes, except that $v = 0$ at this boundary ($j = J$) and u is calculated from $u_{i,J} = u_{i,J-1}$.

4.3.2.3 Equations at the West Boundary

In the source term of the v-momentum equation, a forward difference is used to approximate the term $\frac{\partial p}{\partial \xi}$. Therefore, we use

$$\left.\frac{\partial p}{\partial \xi}\right|_{2,j+1} \approx \frac{p_{4,j+2} + p_{4,j} - p_{2,j} - p_{2,j+2}}{4}.$$

The v-momentum equation along $i = 2$ becomes

$$b_P^W v_{2,j+1} + b_N^W v_{2,j+3} + b_S^W v_{2,j-1} + b_E^W v_{4,j+1} = \eta_y \frac{\hat{p}_{2,j} - \hat{p}_{2,j+2}}{2\rho} + \hat{S}_v^W$$

where

$$\hat{S}_v^W = -\frac{\xi_y\left(\hat{p}_{4,j+2} + \hat{p}_{4,j} - \hat{p}_{2,j} - \hat{p}_{2,j+2}\right)}{4\rho}$$

$$+ \upsilon\left(\frac{\xi_x \eta_x + \xi_y \eta_y}{12}\right)\left(\hat{v}_{4,j+3} - \hat{v}_{4,j-1} - 4v_{1,j+3} + 4v_{1,j-1}\right)$$

$$+ v_{1,j+1}\left[\frac{2\upsilon}{3}\left(\xi_x^2 + \xi_y^2\right) - \frac{2\upsilon}{3}\left(\xi_{xx} + \xi_{yy}\right) + \frac{2}{3}\xi_x \hat{u}_{2,j+1} + \frac{2}{3}\xi_y \hat{v}_{2,j+1}\right]$$

$$b_P^W = \frac{\xi_x \hat{u}_{2,j+1}}{2} + \frac{\xi_y \hat{v}_{2,j+1}}{2} + \upsilon\left(\frac{\eta_x^2 + \eta_y^2}{2}\right) + \upsilon\left(\xi_x^2 + \xi_y^2\right) - \upsilon\left(\frac{\xi_{xx} + \xi_{yy}}{2}\right)$$

$$b_N^W = \frac{\eta_x \hat{u}_{2,j+1}}{4} + \frac{\eta_y \hat{v}_{2,j+1}}{4} - \upsilon\left(\frac{\eta_x^2 + \eta_y^2}{4}\right) - \upsilon\left(\frac{\xi_x \eta_x + \xi_y \eta_y}{4}\right) - \upsilon\left(\frac{\eta_{xx} + \eta_{yy}}{4}\right)$$

$$b_S^W = -\frac{\eta_x \hat{u}_{2,j+1}}{4} - \frac{\eta_y \hat{v}_{2,j+1}}{4} - \upsilon\left(\frac{\eta_x^2 + \eta_y^2}{4}\right) + \upsilon\left(\frac{\xi_x \eta_x + \xi_y \eta_y}{4}\right) + \upsilon\left(\frac{\eta_{xx} + \eta_{yy}}{4}\right)$$

$$b_E^W = \frac{\xi_x \hat{u}_{2,j+1}}{6} + \frac{\xi_y \hat{v}_{2,j+1}}{6} - \upsilon\left(\frac{\xi_x^2 + \xi_y^2}{3}\right) - \upsilon\left(\frac{\xi_{xx} + \xi_{yy}}{6}\right).$$

The u-momentum equation at the west side will be the same as at interior points, except that the velocity components at that boundary are known.

4.3.2.4 Equations at the East Boundary

In the v-momentum equation, a backward difference is used to approximate the term $\frac{\partial p}{\partial \xi}$ and the boundary condition $\frac{\partial v}{\partial \xi} = 0$ is applied at $i = I$ in the discrete form $v_{I+1,j+1} = v_{I-1,j+1}$.

Therefore, we take

$$\left.\frac{\partial p}{\partial \xi}\right|_{I-1,j+1} \approx \frac{p_{I-1,j+2} + p_{I-1,j} - p_{I-3,j+2} - p_{I-3,j}}{4},$$

and the v-momentum equation along $i = I$-1 becomes

$$b_P^E v_{I-1,j+1} + b_N^E v_{I-1,j+3} + b_S^E v_{I-1,j-1} + b_W^E v_{I-3,j+1} = \eta_y \frac{\hat{p}_{I-1,j} - \hat{p}_{I-1,j+2}}{2\rho} + \hat{S}_v^E$$

where

$$\hat{S}_v^E = -\frac{\xi_y\left(\hat{p}_{I-1,j+2} + \hat{p}_{I-1,j} - \hat{p}_{I-3,j+2} - \hat{p}_{I-3,j}\right)}{4\rho} + \upsilon\left(\frac{\xi_x\eta_x + \xi_y\eta_y}{8}\right)\left(\hat{v}_{I-1,j+3} - \hat{v}_{I-3,j+3} - \hat{v}_{I-1,j-1} + \hat{v}_{I-3,j-1}\right)$$

$$b_P^E = \frac{\xi_x\hat{u}_{I-1,j+1}}{2} + \frac{\xi_y\hat{v}_{I-1,j+1}}{2} + \upsilon\left(\frac{\xi_x^2 + \xi_y^2}{4}\right) - \upsilon\left(\frac{\xi_{xx} + \xi_{yy}}{4}\right) + \upsilon\left(\frac{\eta_x^2 + \eta_y^2}{2}\right)$$

$$b_N^E = \frac{\eta_x\hat{u}_{I-1,j+1}}{4} + \frac{\eta_y\hat{v}_{I-1,j+1}}{4} - \upsilon\left(\frac{\eta_x^2 + \eta_y^2}{4}\right) - \upsilon\left(\frac{\eta_{xx} + \eta_{yy}}{4}\right)$$

$$b_S^E = -\frac{\eta_x\hat{u}_{I-1,j+1}}{4} - \frac{\eta_y\hat{v}_{I-1,j+1}}{4} - \upsilon\left(\frac{\eta_x^2 + \eta_y^2}{4}\right) + \upsilon\left(\frac{\eta_{xx} + \eta_{yy}}{4}\right)$$

$$b_W^E = -\frac{\xi_x\hat{u}_{I-1,j+1}}{2} - \frac{\xi_y\hat{v}_{I-1,j+1}}{2} - \upsilon\left(\frac{\xi_x^2 + \xi_y^2}{4}\right) + \upsilon\left(\frac{\xi_{xx} + \xi_{yy}}{4}\right).$$

In the case of the *u*-momentum equation, the same boundary condition $\frac{\partial u}{\partial \xi} = 0$ is applied, represented in discrete form as $u_{I-2,j} = u_{I,j}$. Applying this condition, the discretized *u*-momentum equation along the line $i = I\text{-}2$ becomes

$$a_P^E u_{I-2,j} + a_N^E u_{I-2,j+2} + a_S^E u_{I-2,j-2} + a_W^E u_{I-4,j} = \xi_x\frac{\hat{p}_{I-3,j} - \hat{p}_{I-1,j}}{2\rho} + \hat{S}_u^E$$

where

$$\hat{S}_u^E = \frac{\eta_x\left(\hat{p}_{I-3,j-2} + \hat{p}_{I-1,j-2} - \hat{p}_{I-3,j+2} - \hat{p}_{I-1,j+2}\right)}{8\rho} + \upsilon\left(\frac{\xi_x\eta_x + \xi_y\eta_y}{8}\right)\left(\hat{u}_{I-2,j+2} - \hat{u}_{I-4,j+2} - \hat{u}_{I-2,j-2} + \hat{u}_{I-4,j-2}\right)$$

$$a_P^E = \frac{\xi_x \hat{u}_{I-2,j}}{2} + \frac{\xi_y \hat{v}_{I-2,j}}{2} + \upsilon\left(\frac{\eta_x^2 + \eta_y^2}{2}\right) + \upsilon\left(\frac{\xi_x^2 + \xi_y^2}{4}\right) - \upsilon\left(\frac{\xi_{xx} + \xi_{yy}}{4}\right)$$

$$a_N^E = \frac{\eta_x \hat{u}_{I-2,j}}{4} + \frac{\eta_y \hat{v}_{I-2,j}}{4} - \upsilon\left(\frac{\eta_x^2 + \eta_y^2}{4}\right) - \upsilon\left(\frac{\eta_{xx} + \eta_{yy}}{4}\right)$$

$$a_S^E = -\frac{\eta_x \hat{u}_{I-2,j}}{4} - \frac{\eta_y \hat{v}_{I-2,j}}{4} - \upsilon\left(\frac{\eta_x^2 + \eta_y^2}{4}\right) + \upsilon\left(\frac{\eta_{xx} + \eta_{yy}}{4}\right)$$

$$a_W^E = -\frac{\xi_x \hat{u}_{I-2,j}}{2} - \frac{\xi_y \hat{v}_{I-2,j}}{2} - \upsilon\left(\frac{\xi_x^2 + \xi_y^2}{4}\right) + \upsilon\left(\frac{\xi_{xx} + \xi_{yy}}{4}\right).$$

4.3.2.5 Equations at the West South and West North Corners

The discretized *u*-momentum equation derived for nodes adjacent to the south and north boundaries can be used at these corners respectively, since no changes take place at the west boundary other than that *u* is known. The discretized *v*-momentum equation derived for nodes adjacent to the west boundary can be used at these corners, with velocities known at the south and north boundaries.

4.3.2.6 Equations at the East South and East North Corners

The discretized *u*-momentum equation at south and north boundaries can be used at these corners by modifying the central coefficient (i.e., a_p) according to the boundary condition applied at the east side. The *v*-momentum equation used at the east boundary can be used at these corners, with velocities known at the south and north boundaries.

In general, the *u*-momentum and *v*-momentum equations may be written respectively as

$$\begin{aligned} a_{i-1,j} u_{i-1,j} &= \sum_{nb} a_{nb} u_{nb} + \frac{\xi_x}{\rho} \frac{p_{i-2,j} - p_{i,j}}{2} + \hat{S}_u \\ b_{i,j+1} v_{i,j+1} &= \sum_{nb} b_{nb} v_{nb} + \frac{\eta_y}{\rho} \frac{p_{i,j+2} - p_{i,j}}{2} + \hat{S}_v \end{aligned} \tag{4.11}$$

Here, *nb* refers to the neighbours of the nodes where $u_{i-1,j}$ and $v_{i,j+1}$ are to be calculated.

4.4 Discretization of the Continuity Equation

The discrete continuity equation at the *i j* location may be written as

$$\xi_x \frac{u_{i+1,j} - u_{i-1,j}}{2} + \eta_y \frac{v_{i,j+1} - v_{i,j-1}}{2} = -\eta_x \hat{u}_\eta\Big|_{i,j} - \xi_y \hat{v}_\xi\Big|_{i,j}$$

where the derivatives on the right hand side are evaluated from previous iterations and are approximated by values where *u* and *v* are stored. i.e.,

$$\hat{u}_\eta\Big|_{i,j} = \frac{\hat{u}_{i+1,j+2} + \hat{u}_{i-1,j+2} - \hat{u}_{i+1,j-2} - \hat{u}_{i-1,j-2}}{8}$$

$$\hat{v}_\xi\Big|_{i,j} = \frac{\hat{v}_{i+2,j+1} + \hat{v}_{i+2,j-1} - \hat{v}_{i-2,j+1} - \hat{v}_{i-2,j-1}}{8}.$$

4.4.1 Velocity-Pressure Coupling

Let u^* and v^* be the discrete *u* and *v* fields resulting from a solution of the discrete *u*-and *v*-momentum equations, corresponding to an approximate pressure field p^*. Thus, from equations (4.11),

$$\begin{aligned} a_{i-1,j} u^*_{i-1,j} &= \sum_{nb} a_{nb} u^*_{nb} + \frac{\xi_x}{\rho} \frac{p^*_{i-2,j} - p^*_{i,j}}{2} + \hat{S}^*_u \\ b_{i,j+1} v^*_{i,j+1} &= \sum_{nb} b_{nb} v^*_{nb} + \frac{\eta_y}{\rho} \frac{p^*_{i,j+2} - p^*_{i,j}}{2} + \hat{S}^*_v. \end{aligned} \tag{4.12}$$

As in the Cartesian formulation, a correction is proposed to the starred velocity field

$$\begin{aligned} u &= u^* + u' \\ v &= v^* + v'. \end{aligned} \tag{4.13}$$

Correspondingly, we correct the existing pressure field p^* with

$$p = p^* + p'. \tag{4.14}$$

using equations (4.13) and (4.14), and subtracting equations (4.12) from equations (4.11) we obtain

$$a_{i-1,j}u'_{i-1,j} = \sum_{nb} a_{nb}u'_{nb} + \frac{\xi_x}{\rho}\frac{p'_{i-2,j} - p'_{i,j}}{2} + \hat{S}'_u$$
$$b_{i,j+1}v'_{i,j+1} = \sum_{nb} b_{nb}v'_{nb} + \frac{\eta_y}{\rho}\frac{p'_{i,j} - p'_{i,j+2}}{2} + \hat{S}'_v . \tag{4.15}$$

As in the SIMPLE algorithm, we approximate equations (4.15) as

$$a_{i-1,j}u'_{i-1,j} \approx \frac{\xi_x}{\rho}\frac{p'_{i-2,j} - p'_{i,j}}{2}$$
$$b_{i,j+1}v'_{i,j+1} \approx \frac{\eta_y}{\rho}\frac{p'_{i,j} - p'_{i,j+2}}{2} . \tag{4.16}$$

So, equations (4.13) are now

$$u_{i-1,j} = u^*_{i-1,j} + \xi_x \frac{p'_{i-2,j} - p'_{i,j}}{2\rho a_{i-1,j}}$$
$$v_{i,j+1} = v^*_{i,j+1} + \eta_y \frac{p_{i,j} - p'_{i,j+2}}{2\rho b_{i,j+1}} . \tag{4.17}$$

We now consider the discrete continuity equation. The starred velocities u^* and v^*, obtained by solving the momentum equations using the prevailing pressure field p^*, do not satisfy the discrete continuity equation. Thus we require the corrected velocities, given by equations (4.17), to satisfy the continuity equation. Therefore,

$$\xi_x \frac{\left\{u^*_{i+1,j} + \frac{\xi_x}{\rho}\frac{p'_{i,j} - p'_{i+2,j}}{2a_{i+1,j}}\right\} - \left\{u^*_{i-1,j} + \frac{\xi_x}{\rho}\frac{p'_{i-2,j} - p'_{i,j}}{2a_{i-1,j}}\right\}}{2}$$
$$+\eta_y \frac{\left\{v^*_{i,j+1} + \frac{\eta_y}{\rho}\frac{p'_{i,j} - p'_{i,j+2}}{2b_{i,j+1}}\right\} - \left\{v^*_{i,j-1} + \frac{\eta_y}{\rho}\frac{p'_{i,j-2} - p'_{i,j}}{2b_{i,j-1}}\right\}}{2} = -\eta_x \hat{u}_\eta\Big|_{i,j} - \xi_y \hat{v}_\xi\Big|_{i,j} .$$

Rearranging terms, we may write an equation for the pressure correction as:

$$c_P^{int} p_{i,j}^{'} + c_E^{int} p_{i+2,j}^{'} + c_W^{int} p_{i-2,j}^{'} + c_N^{int} p_{i,j+2}^{'} + c_S^{int} p_{i,j-2}^{'} = \xi_x \frac{u_{i-1,j}^{*} - u_{i+1,j}^{*}}{2} - \eta_y \frac{v_{i,j+1}^{*} - v_{i,j-1}^{*}}{2} + \hat{S}_P^{int}$$

where

$$\hat{S}_P^{int} = -\eta_x \left(\frac{\hat{u}_{i+1,j+2} + \hat{u}_{i-1,j+2} - \hat{u}_{i+1,j-2} - \hat{u}_{i-1,j-2}}{8} \right) - \xi_y \left(\frac{\hat{v}_{i+2,j+1} + \hat{v}_{i+2,j-1} - \hat{v}_{i-2,j+1} - \hat{v}_{i-2,j-1}}{8} \right)$$

$$c_P^{\text{int}} = \frac{\xi_x^2}{4\rho a_{i+1,j}} + \frac{\xi_x^2}{4\rho a_{i-1,j}} + \frac{\eta_y^2}{4\rho b_{i,j+1}} + \frac{\eta_y^2}{4\rho b_{i,j-1}}$$

$$c_E^{\text{int}} = -\frac{\xi_x^2}{4\rho a_{i+1,j}}$$

$$c_W^{\text{int}} = -\frac{\xi_x^2}{4\rho a_{i-1,j}}$$

$$c_N^{\text{int}} = -\frac{\eta_y^2}{4\rho b_{i,j+1}}$$

$$c_S^{\text{int}} = -\frac{\eta_y^2}{4\rho b_{i,j-1}}.$$

4.4.2 Pressure Correction Equation at the Boundaries

Suppose the velocity component v is known at the south and north boundaries and u is known at the west boundary (inlet). Based on this information, the pressure correction equation will take different forms on different boundaries.

4.4.2.1 Pressure Correction Equation at the West Boundary

The velocity components are known at the inlet. Therefore, the pressure correction equation along $i = 2$ will become

$$c_P^{W} p_{2,j}^{'} + c_E^{int} p_{4,j}^{'} + c_N^{int} p_{2,j+2}^{'} + c_S^{int} p_{2,j-2}^{'} = \xi_x \frac{u_{1,j} - u_{3,j}^{*}}{2} - \eta_y \frac{v_{2,j+1}^{*} - v_{2,j-1}^{*}}{2} + \hat{S}_P^{W}$$

where

$$\hat{S}_p^W = -\eta_x\left(\frac{\hat{u}_{3,j+2} + u_{1,j+2} - \hat{u}_{3,j-2} - u_{1,j-2}}{8}\right) - \xi_y\left(\frac{\hat{v}_{4,j+1} + \hat{v}_{4,j-1} + \hat{v}_{2,j+1} + \hat{v}_{2,j-1}}{8}\right)$$

$$c_P^w = \frac{\xi_x^2}{4\rho a_{3,j}} + \frac{\eta_y^2}{4\rho b_{2,j+1}} + \frac{\eta_y^2}{4\rho b_{2,j-1}},$$

and other coefficients are the same as defined at the interior nodes.

4.4.2.2 Pressure Correction Equation at the South Boundary

At the south wall ($j = 1$) the velocity components are equal to zero.

Therefore, the pressure correction equation along $j = 2$ becomes

$$c_P^S p'_{i,2} + c_E^{int} p'_{i+2,2} + c_W^{int} p'_{i-2,2} + c_N^{int} p'_{i,4} = \xi_x \frac{u^*_{i-1,2} - u^*_{i+1,2}}{2} - \eta_y \frac{v^*_{i,3}}{2} + \hat{S}_p^S$$

where

$$\hat{S}_p^S = -\eta_x\left(\frac{\hat{u}_{i+1,2} + \hat{u}_{i-1,2} + \hat{u}_{i-1,4} + \hat{u}_{i+1,4}}{8}\right) - \xi_y\left(\frac{\hat{v}_{i+2,3} - \hat{v}_{i-2,3}}{8}\right)$$

$$c_P^S = \frac{\xi_x^2}{4\rho a_{i+1,2}} + \frac{\xi_x^2}{4\rho a_{i-1,2}} + \frac{\eta_y^2}{4\rho b_{i,3}}.$$

All other coefficients are the same as defined at the interior nodes.

4.4.2.3 Pressure Correction Equation at the North Boundary

At the north boundary the flow symmetry boundary condition is used and the v component of velocity is equal to zero.

Therefore, the pressure correction equation along $j = J$-1 will be

$$c_P^N p'_{i,J-1} + c_E^{int} p'_{i+2,J-1} + c_W^{int} p'_{i-2,J-1} + c_S^{int} p'_{i,J-3} = \xi_x \frac{u^*_{i-1,J-1} - u^*_{i+1,J-1}}{2} + \eta_y \frac{v^*_{i,J-2}}{2} + \hat{S}_p^N$$

where

$$\hat{S}_p^N = -\eta_x\left(\frac{\hat{u}_{i+1,J-1}+\hat{u}_{i-1,J-1}-\hat{u}_{i-1,J-3}-\hat{u}_{i+1,J-3}}{8}\right)-\xi_y\left(\frac{\hat{v}_{i+2,J-2}-\hat{v}_{i-2,J-2}}{8}\right)$$

$$c_P^N = \frac{\xi_x^2}{4\rho a_{i+1,J-1}}+\frac{\xi_x^2}{4\rho a_{i-1,J-1}}+\frac{\eta_y^2}{4\rho b_{i,J-2}}.$$

All other coefficients are the same as defined at the interior nodes.

4.4.2.4 Pressure Correction Equation at the East Boundary

The velocity at the outlet is not corrected by means of pressure corrections. Hence in the discretized pressure correction equation the link to the outlet boundary side is suppressed by setting $c_E = 0$. Therefore the equation along the gridline i = I-1 adjacent to the east boundary is given by

$$c_P^{int} p'_{I-1,j} + c_W^{int} p'_{I-3,j} + c_N^{int} p'_{I-1,j+2} + c_S^{int} p'_{I-1,j-2} = \xi_x \frac{u^*_{I-2,j} - u_{I,j}}{2} - \eta_y \frac{v^*_{I-1,j+1} - v^*_{I-1,j-1}}{2} + \hat{S}_p^E$$

where

$$\hat{S}_p^E = -\eta_x\left(\frac{\hat{u}_{I,j+2}+\hat{u}_{I-2,j+2}-\hat{u}_{I,j-2}-\hat{u}_{I-2,j-2}}{8}\right)-\xi_y\left(\frac{\hat{v}_{I-1,j+1}+\hat{v}_{I-1,j-1}-\hat{v}_{I-3,j+1}-\hat{v}_{I-3,j-1}}{8}\right)$$

and all the coefficients are the same as those at the interior nodes.

The solution algorithm is the same as in Chapter 2, Section 2.5.

CHAPTER V

APPLICATIONS ON A CURVILINEAR GRID

5.1 Introduction

In this chapter, the algorithm developed in Chapter 2 and extended to curvilinear domains in Chapter 4 is applied to three test problems, namely, flow over a backward-facing step, flow in a complex channel, and flow over a scour hole.

Each of the problems considered here is of great interest, the first two being important validation test cases for any numerical model. Although flow over a backward-facing step was simulated in Chapter 3, it is simulated again in this chapter on a rectangular mesh with clustering along the bottom wall. The complex channel is one of the most fundamental curvilinear domains in which flow separation can occur [63]. The scour hole problem is considered as an initial test case for investigating the suitability of the present method in simulating flow patterns generated by a water jet impinging on deformable sand beds.

5.2 The Backward-facing Step Flow with a Clustered Mesh

The problem specification considered in this section is exactly the same as in Chapter 3. The flow is simulated on a mesh where clustering is imposed close to the lower wall boundary as illustrated in Figure 5.1. This problem is considered here to further validate the results obtained in Chapter 3, since more grid points are taken at the region of interest, where reattachment and recirculation take place. It also serves as a simple check on the equations derived in Chapter 4. The case considered is for Re = 200. The results, as shown in Figures 5.2 and 5.3, are identical to those obtained on a Cartesian mesh with

no clustering. This implies that the mesh size taken in Chapter 3 is good enough to accurately capture the reattachment length and the recirculation zone.

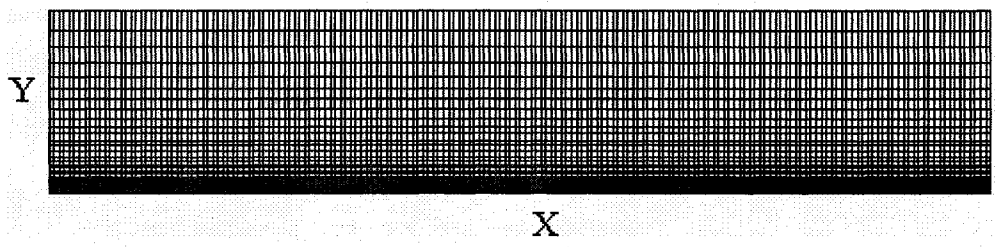

Figure 5.1 Clustered mesh for backward-facing step flow

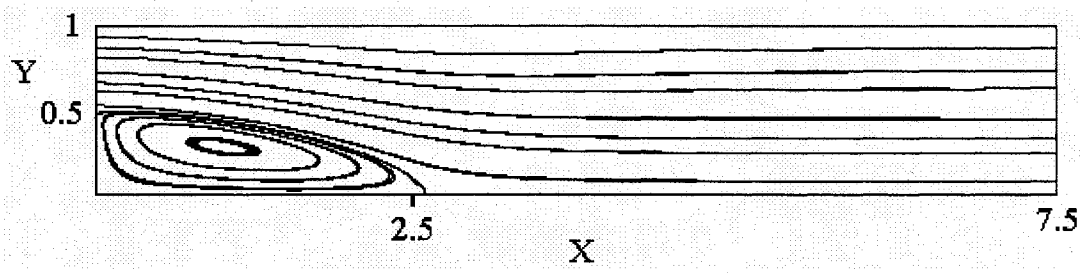

Figure 5.2 Streamlines for $Re = 200$, no clustering

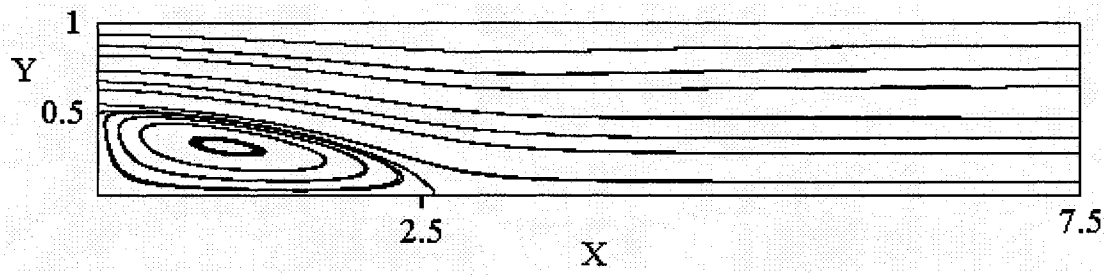

Figure 5.3 Streamlines for $Re = 200$, with clustering

5.3 Flow in a Complex Channel

In 1982, the International Association for Hydraulic Research (IAHR) Working Group on Refined Modeling of Flows devoted the fifth IAHR meeting to the specific subject of assessing the capabilities of various numerical simulation methods to deal with laminar flows in complex geometries. Here, complex geometry refers to a flow domain that does not coincide with the coordinate axes in some simple coordinate system such as Cartesian or polar.

A single, well defined comparison problem, namely the laminar flow in a channel with smooth expansion, suggested by the work of Roache [64] on the scaling of Reynolds number in weakly separated channel flows, was chosen by the IAHR group for testing various numerical methods. The purpose of the test problem was to evaluate the capabilities of various Navier-Stokes solvers and to highlight difficulties in the modeling of complex geometries. A comparison and discussion of the solutions obtained by the participants was reported by Napolitano and Orlandi [65]. This problem has been chosen to test the present solver described in Chapter 4.

5.3.1 Problem Specification and Boundary Conditions

The geometry proposed by Roache [64] is a diverging channel with length depending on the Reynolds number *Re*, i.e., the length of the channel is scaled proportionally to *Re* so that the channel becomes longer and straighter as *Re* increases, as shown in Figure 5.4. For $Re \gg 1$, quasi-self-similar flow conditions and solutions can be obtained, as discussed by Roache [64].

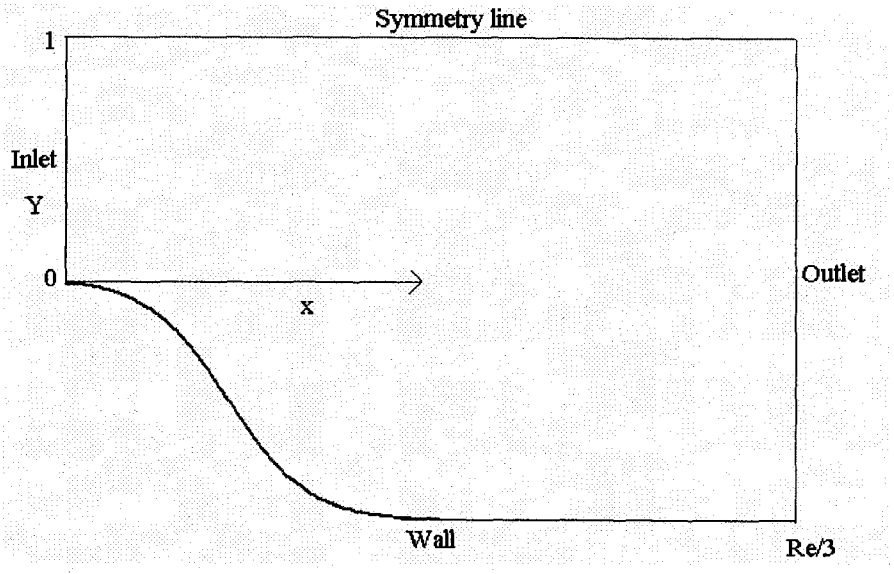

Figure 5.4 Complex channel

For the IAHR workshop, flows were computed for *Re* = 10 and *Re* = 100. *Re* = 10 was chosen because of its highly distorted geometry. *Re* = 100 was chosen to assess the dependence of the convergence rate on *Re*.

The lower boundary of the channel is considered as a wall and is given analytically by

$$y = y_l(x) = \frac{1}{2}[\tanh(2 - 30\frac{x}{\mathrm{Re}}) - \tanh(2)],\ 0 \le x \le \frac{\mathrm{Re}}{3}.$$

The upper boundary, which is taken to be a symmetry line, is located at $y = 1$.

The inlet boundary conditions are given in terms of the Cartesian velocity components u, v as

$$\left.\begin{aligned} u &= 3\left(y - \frac{y^2}{2}\right) \\ v &= 0 \end{aligned}\right\} \text{ for } x = 0,\ 0 \le y \le 1.$$

A parallel flow is assumed for the outflow boundary condition, that is $\frac{\partial u}{\partial x} = 0$ and $\frac{\partial v}{\partial x} = 0$. The origin of the physical coordinates (*x,y*) is on the lower wall at the inflow boundary, where the channel half-height has been normalized to 1. The maximum inflow velocity is $u(0,1) = 1.5$, and the length of the channel is $Re/3$.

The domain as described above is not a rectangular one, so a transformation from the physical domain to a computational domain is employed, and the flow calculation is performed in the computational domain. Elliptic grid generation is used to obtain a staggered grid system in the computational (ξ, η) plane.

The lower and upper boundaries in the computational domain are given by $\eta = 1$ and $\eta = M$ respectively, $1 \le \xi \le N$ where N is the maximum number of nodes in the ξ direction and M is the maximum number of nodes in the η direction. The inlet and outlet boundaries are given by $\xi = 1$ and $\xi = N$ respectively, $1 \le \eta \le M$. A typical grid (in the physical domain) is shown in Figure 5.5.

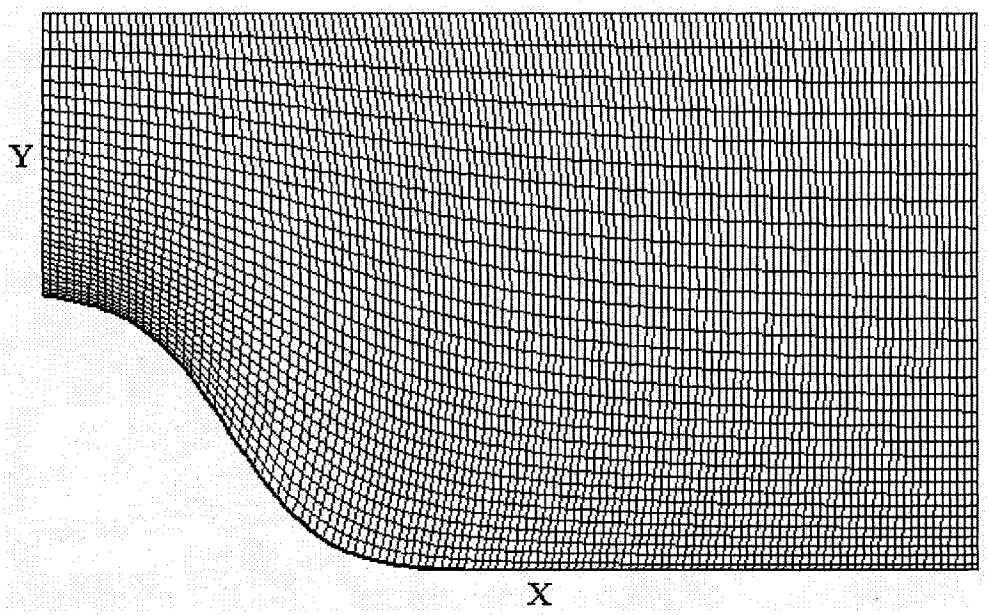

Figure 5.5 Clustered mesh for the complex channel

5.3.2 Results and Discussion

In the absence of an exact reference solution, the results obtained by Cliffe et al [63] have been taken as the benchmark, as recommended by Napolitano and Orlandi [65]. Cliffe et al used a finite element method in primitive variables, a Newton-Raphson linearization scheme and the frontal solution method for the resulting linear system. The results are also compared to Carson [66] who used a velocity-vorticity approach in streamfunction coordinates to solve this problem.

Because of the known difficulties with the outlet boundary condition, several runs for different outlet lengths were performed in the present work. For $Re = 10$ the first run used exactly the same domain as defined above. In this case the flow was still developing at the given outlet, so the specified outlet boundary condition, which is appropriate to fully developed flow, is not strictly applicable. This issue was also reported by Cliffe et al [63]. To avoid this problem another run was taken, in which the outlet boundary was extended.

The length of the lower and upper boundary were taken to be *Re* instead of *Re*/3 and a mesh of size 201x101 was used, with clustering at the lower boundary. In this case the separation zone and the reattachment length were captured correctly, as shown in Figure 5.6. The predicted reattachment length is 1.82 and the reattachment length obtained by Cliffe et al [63] was 1.76. The convergence criterion was taken to be $|u_{old} - u_{new}| \leq 10^{-6}$ and the number of iteration required was 11669. The circulation zone obtained by using FLUENT is shown in Figure 5.7. The circulation zones obtained by FLUENT and the proposed method are almost identical. The vorticity was also evaluated at the lower wall using $\omega = \frac{\partial v}{\partial x} - \frac{\partial u}{\partial y}$, which in the curvilinear coordinates is reduced to

$$\omega = \left(\frac{\partial \eta}{\partial x}\frac{\partial v}{\partial \eta}\right) - \left(\frac{\partial \eta}{\partial y}\frac{\partial u}{\partial \eta}\right).$$

Derivatives normal to the wall were evaluated using one-sided difference approximation of second order.

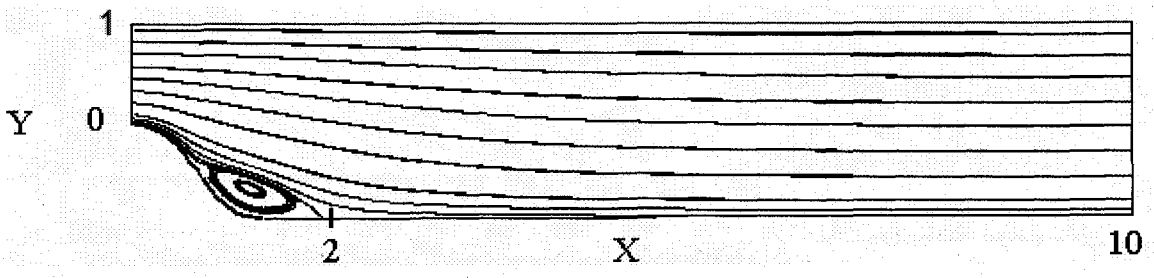

Figure 5.6 Streamlines for *Re* = 10 using present method

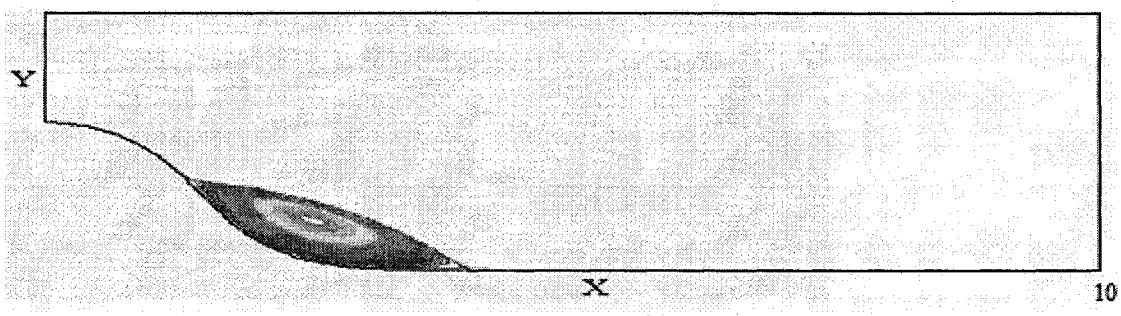

Figure 5.7 Streamlines for $Re = 10$ using FLUENT

Figure 5.8 shows the vorticity at the wall using the proposed method compared to those found by Cliffe et al [63] and Carson [66]. Figure 5.9 shows pressure at the wall using the proposed method compared to those found by Cliffe et al [63] and Rostagi [67]. The nature of the imposed inlet velocity profile generates a discontinuity in vorticity on the channel wall at the inlet. This discontinuity affects the pressure close to the inlet, and Cliffe et al [63] have made an adjustment for this discontinuity. Runs were carried out for several different mesh sizes. A smaller number of nodes could not capture the circulation zone, even though the 'solution' behaved nicely. For less nodes, a length of $Re/3$ allowed the 'solution' to converge, but the circulation zone could not be captured.

Napolitano and Orlandi [65] reported in their paper that some of the researchers involved in the fifth meeting of the IAHR failed to obtain separation in the case of $Re = 100$. Others reported large average percentage errors of vorticity, which is primarily due to inaccurate results in calculating the separation length. Carson [66] in his work also failed to obtain converged solution at $Re = 100$. Di Carlo et al [68] obtained a recirculation region. In their work, they used second order differencing to discretize the convective terms. In this present method, the solution converged but the circulation region could not be captured even on a refined mesh, as shown in Figure 5.10. FLUENT also failed in

capturing the recirculation zone. This problem could not be avoided by using a more refined mesh. Possibly, it could be solved by using other differencing such as second order upwind, or a hybrid scheme.

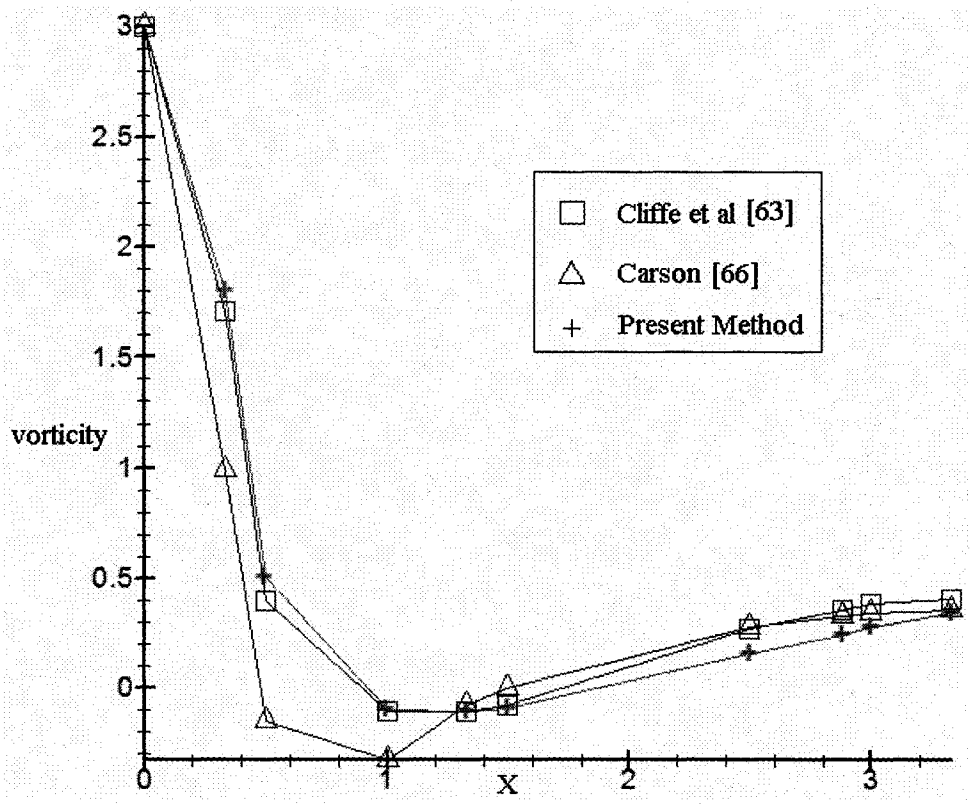

Figure 5.8 Vorticity along the lower wall, $Re = 10$

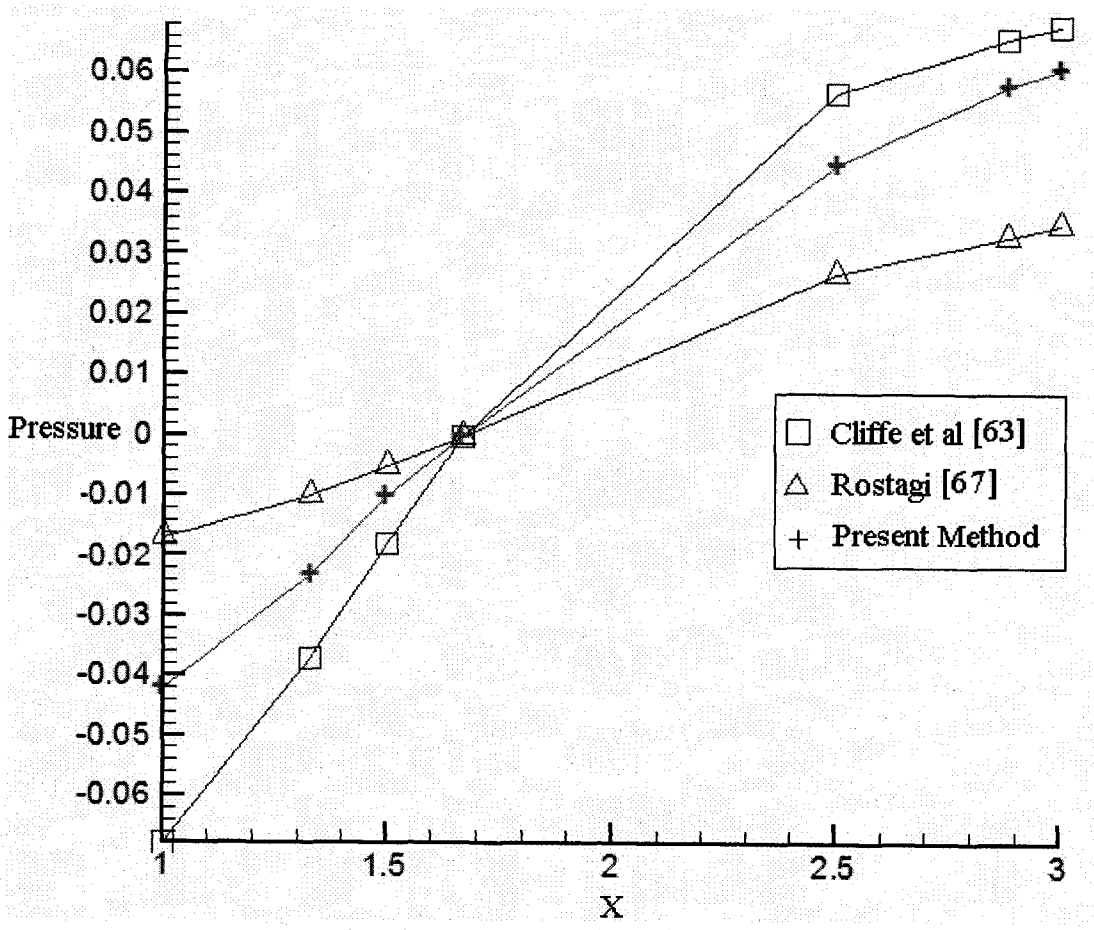

Figure 5.9 Pressure along the lower wall, $Re = 10$

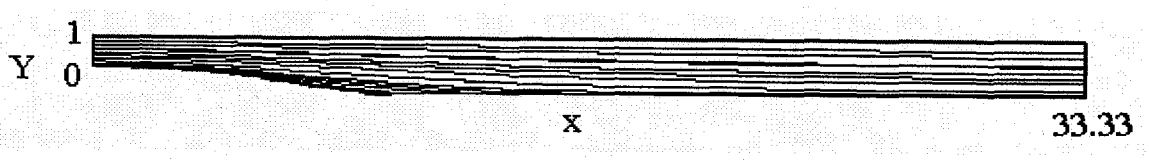

Figure 5.10 Streamlines for $Re = 100$ using present method

5.4 Flow in a Scour Hole

5.4.1 Problem Specification and Boundary Conditions

Bey [69] performed experiments in a 2.5 m long and 0.5 m high channel with a wall jet of 2.5 mm width. Figure 5.11 shows the channel shape after the scour hole has developed. For the simulation in this thesis, the lower boundary of the channel is considered as a wall, where $u = v = 0$, and is created based on the *(x,y)* locations provided by Bey [69]. The upper boundary, which is taken to be symmetry plane, is located at $y = 0.5$. The inlet boundary conditions are given in terms of the Cartesian velocity components u, v as

$$\left.\begin{aligned} u &= 0 \\ v &= 0 \end{aligned}\right\} \text{ for } x = 0,\ 0.0125 \le y \le 0.5$$

$$\left.\begin{aligned} u &= 0.0015 \\ v &= 0 \end{aligned}\right\} \text{ for } x = 0,\ -0.0125 \le y \le 0.0125 \qquad \text{(jet).}$$

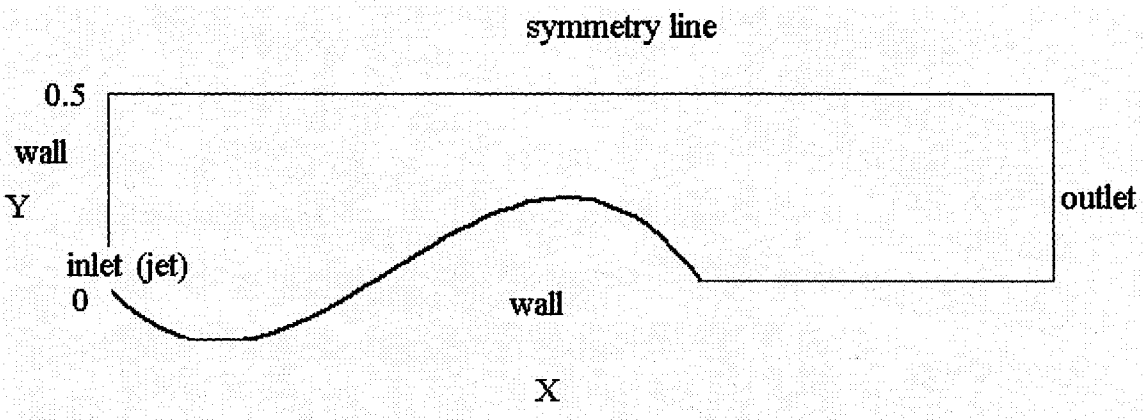

Figure 5.11 Schematic of developed scour hole in a channel

This velocity profile corresponds to $Re = \frac{uh}{\upsilon} = 25$, where h is the jet height. The flow at the outlet boundary is assumed to be a parallel flow, that is $\frac{\partial u}{\partial x} = 0$ and $\frac{\partial v}{\partial x} = 0$.

Since the domain is not rectangular, a transformation from the physical domain to a rectangular domain is used, and the calculation is carried out in the computational domain.

The lower and upper boundaries in the computational domain are now given by $\eta = 1$ and $\eta = M$ respectively, $1 \le \xi \le N$ where N is the maximum number of nodes in the ξ direction. The inlet and outlet boundaries are given by $\xi = 1$ and $\xi = N$ respectively, $1 \le \eta \le M$ where M is the maximum number of nodes in the η direction.

5.4.2 Results and Discussion

The expected flow pattern for the scour hole is shown in Figure 5.12, taken from Li [70]. The experimental results of Bey [69] are shown in Figure 5.13. It should be pointed out that Bey's [69] results correspond to a turbulent flow at Reynolds number of 25,000 and, in the experimental setup, the upper surface is a free surface which is allowed to deform. The results obtained in this thesis, with a nondeformable upper surface and Re = 25, are shown in Figure 5.14. It is expected that a large vortex will develop above the hole and a separation zone will occur where the dune meets the initial bed level. The results obtained in this thesis agree very well with this expectation.

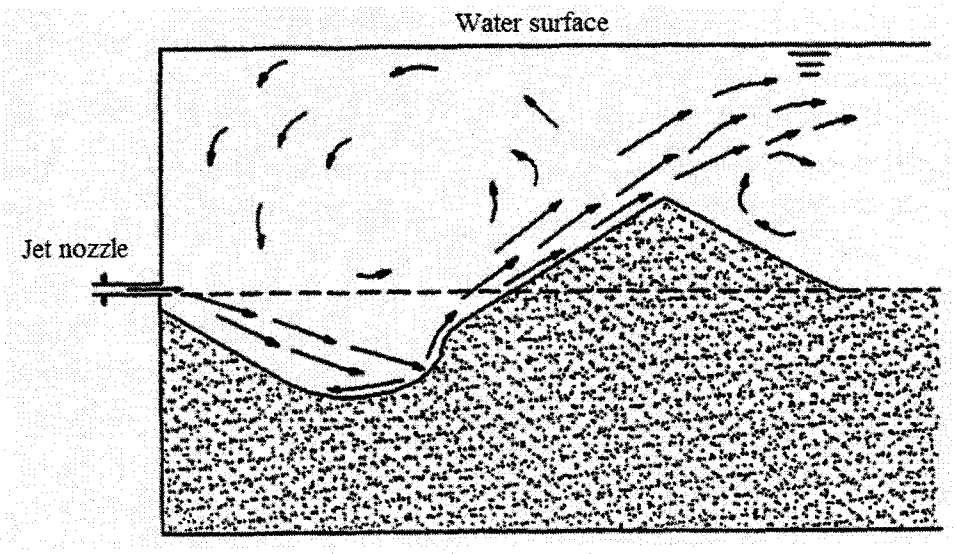

Figure 5.12 Velocity field, Li [70] (experimental)

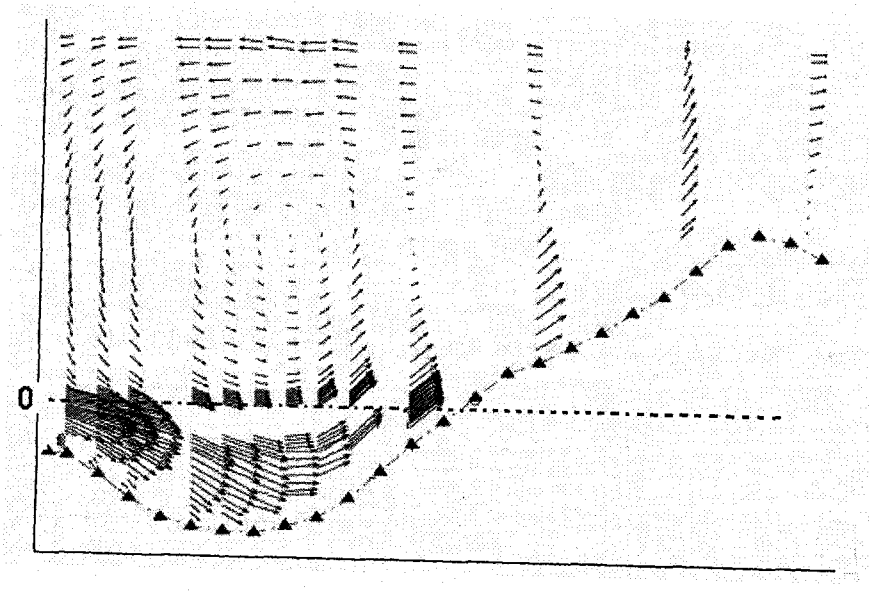

Figure 5.13 Velocity field, Bey [69] (experimental)

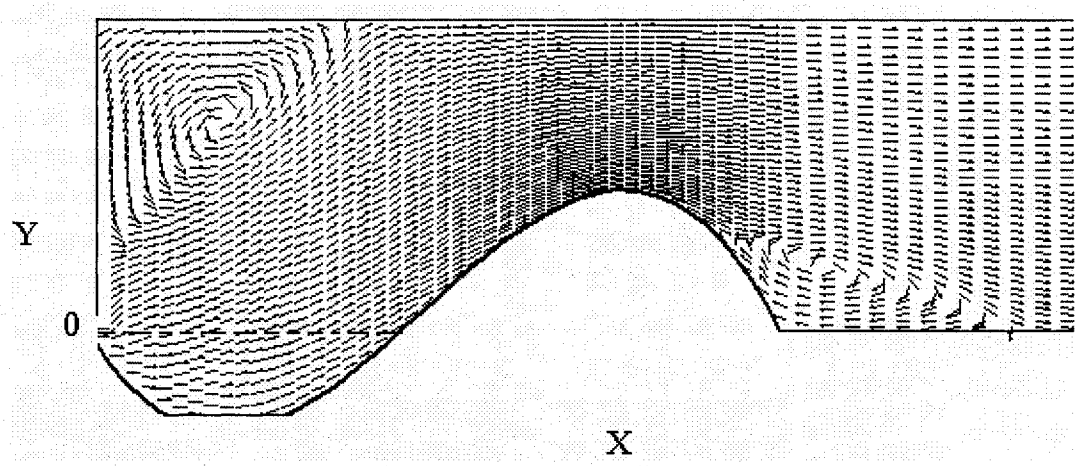

Figure 5.14 Velocity field, present method

5.4.3 Multiblock Solution for the Scour Hole Flow Problem

The development of a multiblock methodology for a non-rectangular physical domain is similar to that described in Section 3.3.3.2 for a Cartesian mesh. The computational domain is divided into two blocks as shown in Figure 5.15. The difference here originates from the continuity equation which, in discretized form, is given by

$$\xi_x \frac{u_{i+1,j} - u_{i-1,j}}{2} + \eta_y \frac{v_{i,j+1} - v_{i,j-1}}{2} = -\eta_x \hat{u}_\eta\Big|_{i,j} - \xi_y \hat{v}_\xi\Big|_{i,j}. \tag{5.1}$$

In block 1, the continuity equation is discretized at $i, \frac{J-1}{2}$, which corresponds to the grid line adjacent to the north boundary, as

$$\xi_x \frac{u_{i+1,\frac{J-1}{2}} - u_{i-1,\frac{J-1}{2}}}{2} + \eta_y \frac{v_{i,\frac{J+1}{2}} - v_{i,\frac{J-3}{2}}}{2} = -\eta_x \hat{u}_\eta\Big|_{i,\frac{J-1}{2}} - \xi_y \hat{v}_\xi\Big|_{i,\frac{J-1}{2}} \tag{5.2}$$

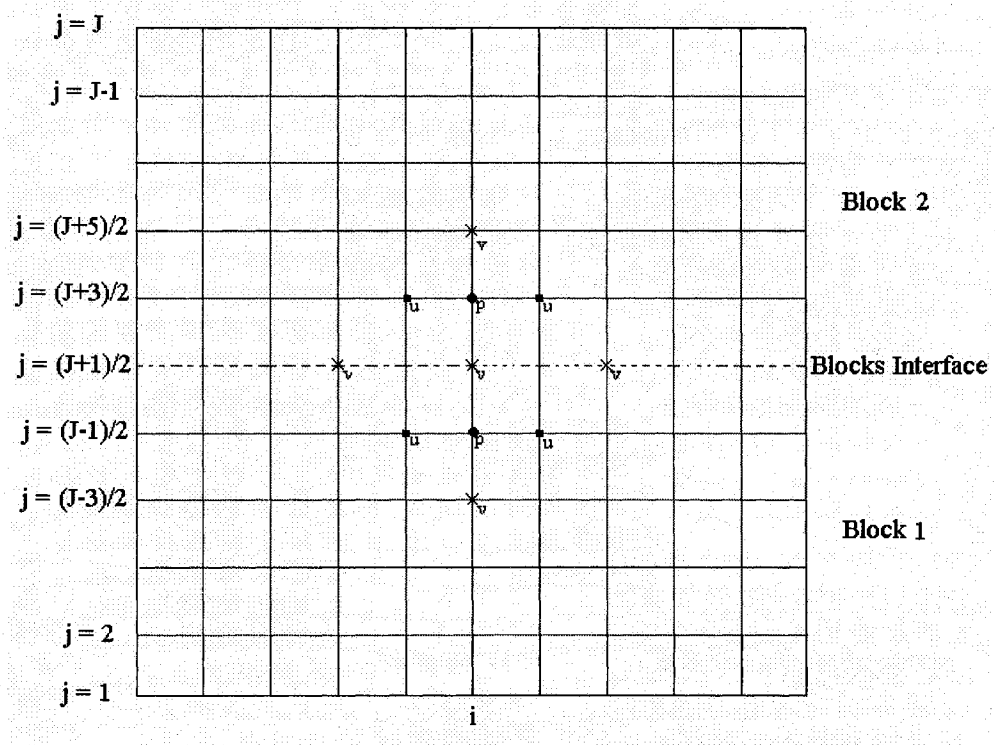

Figure 5.15 Multiblock mesh

Therefore, the relation between v stored at the interface and v at two grid lines south of the interface is

$$v_{i,\frac{J+1}{2}} = v_{i,\frac{J-3}{2}} + \left.\frac{\xi_x}{\eta_y}\right|_{i,\frac{J-1}{2}} \left(u_{i-1,\frac{J-1}{2}} - u_{i+1,\frac{J-1}{2}} \right) - \left. \frac{2}{\eta_y} \left(\eta_x \hat{u}_\eta + \xi_y \hat{v}_\xi \right) \right|_{i,\frac{J-1}{2}} \tag{5.3}$$

In block 2, the relation between v at the interface and v at two grid lines north of the interface is

$$v_{i,\frac{J+1}{2}} = v_{i,\frac{J+5}{2}} - \left.\frac{\xi_x}{\eta_y}\right|_{i,\frac{J+3}{2}} \left(u_{i-1,\frac{J+3}{2}} - u_{i+1,\frac{J+3}{2}} \right) + \left. \frac{2}{\eta_y} \left(\eta_x \hat{u}_\eta + \xi_y \hat{v}_\xi \right) \right|_{i,\frac{J+3}{2}} \tag{5.4}$$

The v-momentum equation at the north boundary in block 1 becomes

$$b_P^N v_{i,\frac{J-3}{2}} + b_S^N v_{i,\frac{J-7}{2}} + b_W^N v_{i-2,\frac{J-3}{2}} + b_E^N v_{i+2,\frac{J-3}{2}} = \eta_y \frac{\hat{p}_{i,\frac{J-5}{2}} - \hat{p}_{i,\frac{J-1}{2}}}{2\rho} + \hat{S}_v^N \tag{5.5}$$

where

$$b_P^N = \hat{u}_{i,\frac{J-3}{2}}\left(\frac{\xi_x}{2}+\frac{\eta_x}{4}\right)+\hat{v}_{i,\frac{J-3}{2}}\left(\frac{\xi_y}{2}+\frac{\eta_y}{4}\right)+\upsilon\left(\frac{\eta_x^2+\eta_y^2}{4}\right)+\upsilon\left(\frac{\xi_x^2+\xi_y^2}{2}\right)-\upsilon\left(\frac{\eta_{xx}+\eta_{yy}}{4}\right)$$

$$b_S^N = -\frac{\eta_x \hat{u}_{i,\frac{J-3}{2}}}{4} - \frac{\eta_y \hat{v}_{i,\frac{J-3}{2}}}{4} - \upsilon\left(\frac{\eta_x^2+\eta_y^2}{4}\right)+\upsilon\left(\frac{\eta_{xx}+\eta_{yy}}{4}\right)$$

$$b_W^N = -\frac{\xi_x \hat{u}_{i,\frac{J-3}{2}}}{2} - \frac{\xi_y \hat{v}_{i,\frac{J-3}{2}}}{2} - \upsilon\left(\frac{\xi_x^2+\xi_y^2}{4}\right)+\upsilon\left(\frac{\xi_{xx}+\xi_{yy}}{4}\right)$$

$$b_E^N = -\upsilon\left(\frac{\xi_x^2+\xi_y^2}{4}\right)-\upsilon\left(\frac{\xi_{xx}+\xi_{yy}}{4}\right) \tag{5.6}$$

$$\hat{S}_v^N = -\frac{\xi_y\left(\hat{p}_{i+2,\frac{J-1}{2}} + \hat{p}_{i+2,\frac{J-5}{2}} - \hat{p}_{i-2,\frac{J-5}{2}} - \hat{p}_{i-2,\frac{J-1}{2}}\right)}{8\rho}$$

$$+\upsilon\left(\frac{\xi_x\eta_x+\xi_y\eta_y}{8}\right)\left(\hat{v}_{i+2,\frac{J+1}{2}} - \hat{v}_{i-2,\frac{J+1}{2}} - \hat{v}_{i+2,\frac{J-7}{2}} + \hat{v}_{i-2,\frac{J-7}{2}}\right)$$

$$-\frac{2}{\eta_y}\left(\frac{\eta_x \hat{u}_{i,\frac{J-3}{2}}}{4} + \frac{\eta_y \hat{v}_{i,\frac{J-3}{2}}}{4} - \upsilon\left(\frac{\eta_x^2+\eta_y^2}{4}\right)-\upsilon\left(\frac{\eta_{xx}+\eta_{yy}}{4}\right)\right).$$

$$\left(-\frac{\eta_x}{8}\left(\hat{u}_{i+1,\frac{J+3}{2}} + \hat{u}_{i-1,\frac{J+3}{2}} - \hat{u}_{i+1,\frac{J-5}{2}} - \hat{u}_{i-1,\frac{J-5}{2}}\right) - \frac{\xi_y}{8}\left(\hat{v}_{i+2,\frac{J+1}{2}} + \hat{v}_{i+2,\frac{J-3}{2}} - \hat{v}_{i-2,\frac{J+1}{2}} - \hat{v}_{i-2,\frac{J-3}{2}}\right)\right.$$

$$\left. -\frac{\xi_x}{2}\left(\hat{u}_{i+1,\frac{J-1}{2}} - \hat{u}_{i-1,\frac{J-1}{2}}\right)\right).$$

Once v is known in block 1, equation (5.3) can be used to evaluate v at the interface. Block 2 can then be treated as discussed in Chapter 4 where v is known at the south boundary (interface).

This multiblock methodology has been applied to simulate the flow over the scour hole described in Section 5.4.1. Results obtained are almost identical to those obtained in the case of a single block, as shown in Figure 5.16.

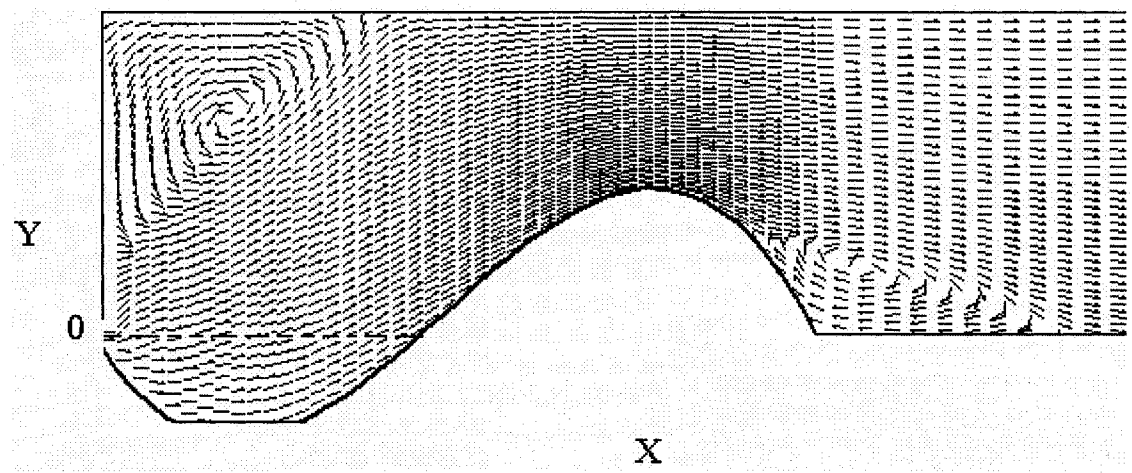

Figure 5.16 Velocity field, two blocks

5.5 Conclusions

In this chapter, the proposed method has been tested on three problems on a curvilinear mesh. Flow over a backward-facing step with a clustered mesh, flow in a complex channel, and the flow in a scour hole.

The results obtained for Re = 200 for a flow over a backward-facing step on a clustered mesh are identical to those obtained in Chapter 3.

The flow in a complex channel for Re = 10 and 100 is simulated using the proposed method. Numerical results are compared with benchmark solutions and FLUENT

solutions. In the case of Re = 10, the proposed method is found to give realistic flow predictions and the results found for pressure and vorticity along the lower wall are in very good agreement with the results presented by Cliffe et al [63] and Carson [66]. In the case of Re = 100, the circulation zone could not be captured even though the solution was stable and converged. FLUENT, Carson [66], and some researchers involved in the fifth meeting of the IAHR also failed to capture the circulation zone.

For the scour hole problem, the flow is simulated for Re = 25. The flow pattern (vortex above the scour hole and the separation zone where the dune meets the initial bed level) obtained is consistent with experimental observations reported in literature, see Bey [69] and Li [70].

CHAPTER VI

CONCLUSIONS AND RECOMMENDATIONS

6.1 Conclusions

This thesis presents a new numerical method for solving the two-dimensional, steady, incompressible, laminar viscous flow equations on a staggered grid. The proposed methodology is finite difference based, but essentially takes advantage of the best features of two well-established numerical formulations, the finite difference and finite volume methods. One of the major weaknesses of the finite difference approach, the difficulty in computing the pressure field, has been removed by exploiting the strengths of the finite volume method. In particular, the issue of velocity-pressure coupling is dealt with in the proposed finite difference formulation by developing a pressure correction equation in a manner similar to the SIMPLE approach commonly used in finite volume formulations. However, since this is purely a finite difference formulation, numerical approximation of fluxes is not required. Results obtained from the present method are based on the first order upwind scheme for the convective terms, but the methodology can easily be modified to accommodate higher order differencing schemes. For first order upwinding, an interesting feature is that the influence matrix obtained from the discretized equations is diagonally dominant which upon inversion gives stable numerical results. In the finite volume formulation, diagonal dominance is only guaranteed at final convergence.

This method is first tested on a simple problem that has an exact solution in part of the flow domain, developing flow in a duct. The results are in excellent agreement with the

exact solution in the fully developed region and with other numerical results in the developing region.

The two-dimensional lid-driven cavity flow and the flow over a backward facing-step with various Reynolds number are simulated using the proposed method. Numerical results are compared with the benchmark solutions and the experimental data when available. Moreover, some of the results are also compared to simulations using FLUENT. For the cavity flow, the simulations are conducted for Re = 100, 400, and 1000. The results for the velocity and pressure along the geometric centrelines are presented and show good agreement with published data. For the flow over a backward-facing step, the reattachment length predicted by the proposed method is in excellent agreement with the experimental and numerical data given by other researchers. The results were obtained for Re = 50, 100, 200, 400 and 500. It is also found that pressure contours obtained by this method are identical to those obtained by FLUENT.

The generality of the method is also tested by simulating fluid flows on curvilinear grids. The numerical results of three different fluid flows, flow over a backward-facing step, a scour hole problem and flow in a complex channel, are presented using the proposed numerical procedure. The numerical results are compared with the benchmark solutions and experimental results. FLUENT was also used to verify the results for flow in the complex channel.

To test the suitability of the proposed method in highly irregular flow domains, flow over a backward-facing step and flow in the scour hole channel are also simulated using a multiblock grid. The results obtained are identical to the case of single block.

6.2 Recommendations for Future Research

In this thesis, the convective terms are discretized using the first order upwind differencing scheme. To obtain more accurate results, it is recommended that a higher order upwind differencing scheme or any other scheme, like hybrid or exponential, be implemented.

One of the main achievements of this work has been to demonstrate the ability of the proposed method to simulate steady, two-dimensional, laminar incompressible flows. However, there is nothing inherent in the procedure that limits its applicability to these flows. A systematic plan should be developed to extend this new approach to unsteady flows, turbulent flows, three-dimensional flows, multiphase flows, etc.

REFERENCES

[1] I.G. Currie, "Fundamental Mechanics of Fluids", McGraw-Hill, New York, 1974.

[2] A.D. Gosman, W.M. Pun, A.K. Runchal, D.B. Spalding and M. Wolfstein, "Heat and Mass Transfer in Recirculating Flows", New York, Academic Press, 1969.

[3] W.R. Briley, "A Numerical Study of Laminar Separation Bubbles using the Navier-Stokes Equations", United Aircraft Research Laboratories Report JII0614-1, East Hartford, Connecticut, 1970.

[4] J.D. Bozeman and C. Dalton, "Numerical Study of Viscous Flow in a Cavity", J. Computational Physics, Vol. 12, 348-363, 1973.

[5] M. Napolitano and R.W. Walters, "An Incremental Block-Line Gauss-Seidel Method for the Navier-Stokes Equations", AIAA J., Vol. 24, No.5, 770-776, 1986.

[6] G.A. Osswald, K.N. Ghia and U. Ghia, "Study of Incompressible Separated Flow Using an Implicit Time-Dependent Technique", Proceedings of the AIAA Computational Fluid Dynamics Conference, Danvers, Mass., July 13-15, 1983.

[7] H.L. Stone, "Iterative Solution of Implicit Approximations of Multidimensional Partial Differential Equations", SIAM J. of Numerical Analysis, Vol. 5, 530-558, 1968.

[8] K.N. Ghia, G.A. Osswald and U. Ghia, "A Direct Method for the Solution of Unsteady Two-Dimensional Incompressible Navier-Stokes Equations", Second Symposium on Numerical and Physical Aspects of Aerodynamic Flows, California State University, Long Beach, California, 1983.

[9] A.J. Chorin, "A Numerical Method for Solving Incompressible Viscous Flow Problems", J. Computational Physics, Vol. 2, 12-26, 1967.

[10] J. Kim and P. Moin, "Application of a Fractional-Step Method to Incompressible Navier-Stokes Equations", J. Computational Physics, Vol. 59, 308-323, 1985.

[11] K.A. Hoffmann and S.T. Chiang, "Computational Fluid Dynamics", Vol. 1, Wichita, KS, 1998.

[12] A.J. Chorin, "Numerical Solution of the Navier-Stokes Equation", Mathematics of Computation, Vol. 22, 745-762, 1968.

[13] S.V. Patankar and D.B. Spalding, "A Calculation Procedure for Heat and Mass Transfer in Three Dimensional Parabolic Flows", Int. J. Heat and Mass Transfer, Vol. 15, 1787-1806, 1972.

[14] L.S. Caretto, A.D. Gosman, S.V. Patankar and D.B. Spalding, "Two Calculation Procedures for Steady Three-Dimensional Flows with Recirculation", Proceedings of the 3rd International Conference on Numerical Methods in Fluid Dynamics, Paris, Vol. 2, 60-68, 1972.

[15] S.V. Patankar, "Numerical Heat Transfer and Fluid Flow", Hemisphere, New York, 1980.

[16] J.P. Van Doormaal and G.D. Raithby, "An Evaluation of the Segregated Approach for Predicting Incompressible Fluid Flows", ASME Paper 85-HT-9, National Heat Transfer Conference, Denver, Colorado, August 4-7, 1985.

[17] B.R. Latimer and A. Pollard, "Comparison of Pressure-Velocity Coupling Solution Algorithms", Numerical Heat Transfer, Vol. 8, 635-652, 1985.

[18] G.D. Raithby and G.E. Schneider, "Numerical Solution of Problems in Incompressible Fluid Flow: Treatment of the Velocity-Pressure Coupling", Numerical Heat Transfer, Vol. 2, 417-440, 1979.

[19] W.R. Briley, "Numerical Methods for Computing Three-dimensional Flows in Ducts", J. Computational Physics, Vol. 14, 8-28, 1974.

[20] V.S. Pratap and D.B. Spalding, "Fluid Flow and Heat Transfer in Three Dimensional Duct Flows", Int. J. Heat and Mass Transfer, Vol. 19, 1183-1188, 1976.

[21] H.K. Versteeg and W. Malalasekera, "An Introduction to Computational Fluid Dynamics: The Finite Volume Approach", Pearson, UK, 1995.

[22] G.D. Thiart, "Finite Difference Schemes for the Numerical Solution of Fluid Flow and Heat Transfer Problems on Nonstaggered Grids", Numerical Heat Transfer, Part B, Vol. 17, 43-62, 1990.

[23] T.F. Miller and F.W. Schmidt, "Use of a Pressure-Weighted Interpolation Method for the Solution of the Incompressible Navier-Stokes Equations on a Non-Staggered Grid System", Numerical Heat Transfer, Vol. 14, 213-233, 1988.

[24] I.E. Barton and R. Kirby, "Finite Difference Scheme for the Solution of Fluid Flow Problems on Non-Staggered Grids", Int. J. for Num. Methods in Fluids, Vol. 33, 939-959, 2000.

[25] M. Peric, R. Kessler and G. Scheuerer, "Comparison of Finite-Volume Numerical Methods with Staggered and Colocated Grids", Computers and Fluids, Vol. 16, 389-403, 1988.

[26] K.C. Karki and S.V. Patankar, "Calculation Procedure for Viscous Incompressible Flows in Complex Geometries", Numerical Heat Transfer, Vol. 14, 295-307, 1988.

[27] W. Shyy, S.S. Tong and S. Correa, "Numerical Recirculating Flow Calculation Using a Body-Fitted Coordinate System", Numerical Heat Transfer, Vol. 8, 99-113, 1985.

[28] M. Reggio and R. Camarero, "Numerical Solution Procedure For Viscous Incompressible Flows", Numerical Heat Transfer, Vol. 10, 131-146, 1986.

[29] M. Peric, "Analysis of Pressure-Velocity Coupling on Nonorthogonal Grids", Numerical Heat Transfer, Part B, Vol. 17, 63-82, 1990.

[30] W. Shyy, S. Thakur and J. Wright, "Second-Order Upwind and Central Difference Schemes for Recirculating Flow Computation", AIAA J., Vol. 30, 923-932, 1992.

[31] H.H. Wong and G.D. Raithby, "Improved Finite-Difference Methods Based on a Critical Evaluation of the Approximation Errors", Numerical Heat Transfer, Vol. 2, 139-163, 1979.

[32] G.D. Raithby, "Skew Upstream Differencing Schemes for Problems Involving Fluid Flow", Computer Methods in Applied Mechanics and Engineering, Vol. 9, 153-164, 1976.

[33] B.P. Leonard, "A Stable and Accurate Convective Modeling Procedure Based on Quadratic Upstream Interpolation", Computer Methods in Applied Mechanics and Engineering, Vol. 19, 59-98, 1979.

[34] A. Pollard and A.L.W. Siu, "The Calculation of Some Laminar Flows Using Various Discretization Schemes", Computer Methods in Applied Mechanics and Engineering, Vol. 35, 293-313, 1982.

[35] B.P. Leonard, "Simple High-Accuracy Resolution Program for Convective Modeling of Discontinuities", Int. J. for Num. Methods in Fluids, Vol. 8, 1291-1318, 1988.

[36] C.W. Hirt, "Heuristic Stability Theory for Finite-Difference Equations", J. Computational Physics, Vol. 2, 339-355, 1968.

[37] T.J. Chung, "Computational Fluid Dynamics", Cambridge University Press, UK, 2002.

[38] J.C. Tannehill, D.A. Anderson and R.H Pletcher, "Computational Fluid Mechanics and Heat Transfer", 2nd Edition, McGraw Hill, USA, 1984.

[39] D.A. Anderson, "Computational Fluid Dynamics: The Basics with Applications", McGraw Hill, USA, 1995.

[40] J.H. Ferziger and M. Peric, "Computational Methods for Fluid Dynamics", 3rd Edition, Springer, USA, 2002.

[41] H. Schlichting, "Boundary Layer Theory", 8th Edition, McGraw-Hill, New York, 2000.

[42] I.J. Kim, "Investigation of Separation and Reattachment of a Turbulent Shear Layer: Flow over a Backward Facing Step", Ph.D. Thesis, Stanford University, USA, 1978.

[43] K. O'Malley, A.D. Fitt, T.V. Jones, J.R. Ockendon and P. Wilmott, "Models for High Reynolds Number Flow Down a Step", J. Fluid Mechanics, Vol. 222, 139-155, 1991.

[44] L.P. Hackman, G.D. Raithby and A.B. Strong, "Numerical Predictions of Flows over Backward Facing Steps", Int. J. for Num. Methods in Fluids, Vol. 4, 711-724, 1984.

[45] R.G. Goldstien, V.L. Eriksen, R.M. Olson and E.R.G. Eckert, "Laminar Separation, Reattachment and Transition of the Flow over a Downstream Facing Step", J. Basic Engg., ASME, Vol. 92, 732-741, 1970.

[46] S. Thangam and D.D. Knight, "Effect of Stepheight on the Separated Flow Past a Backward Facing Step", Physics of Fluids, Vol. 1, No. 3, 604-606, 1989.

[47] A.F. Ghoniem and Y. Gagnon, "Vortex Simulation of Laminar Recirculating Flow", J. Computational Physics, Vol. 68, 346-377, 1987.

[48] G. Guj and F. Stella, "Numerical Solutions of High Re Recirculating Flows in Vorticity-Velocity Form", Int. J. for Num. Methods in Fluids, Vol. 8, 405-416, 1988.

[49] I.E. Barton, "A Numerical Study of Flow over Confined Backward-facing Step" Int. J. for Num. Methods in Fluids, Vol. 21, 653-665, 1995.

[50] B.F. Armaly, F. Durst, J.C.F. Pereira and B. Schonung, "Experimental and Theoretical Investigation of Backward-facing Step Flow", J. Fluid Mechanics, Vol. 127, 473-496, 1983.

[51] R.W. Barber and A. Fonty, "Comparison of Vortex-element and Finite-volume Simulations of Low Reynolds Number Flow over a Confined Backward Facing Step", Proceedings of the 11th Annual Conference of the CFD Society of Canada, CFD2003, Vol. 2, 780-787, 2003, Vancouver, Canada.

[52] CFD Research Corporation, Cummings Research Park, 215 Wynn Drive, Huntsville, AL 35805, USA, User Manual: Version 6.4, 2000.

[53] E. Erturk, T.C. Corke and C. Gockol, "Numerical Solutions of 2-D Steady Incompressible Driven Cavity Flow at High Reynolds Numbers", Int. J. for Num. Methods in Fluids, Vol. 48, 747-774, 2005.

[54] M. Aydin and R.T. Fenner, "Boundary Element Analysis of Driven Cavity Flow for Low and Moderate Reynolds Numbers", Int. J. for Num. Methods in Fluids, Vol. 37, 45-64, 2001.

[55] M.M. Grigoriev and G.F. Dargush, "A Poly-Region Boundary Element Method for Incompressible Viscous Fluid Flows", Int. J. for Num. Methods in Engineering, Vol. 46, 1127-1158, 1999.

[56] U. Ghia, K.N. Ghia and C.T. Shin, " High-Re Solutions for Incompressible Flow Using the Navier-Stokes Equations and a Multigrid Method", J. Computational Physics, Vol. 48, 387-411, 1982.

[57] J.F. Thompson, F.C. Thames and C.W. Mastin, "Automatic Numerical Generation of Body-Fitted Curvilinear Coordinates System for Fields Containing any Number of Arbitrary Two-Dimensional Bodies", J. Computational Physics, Vol. 15, 299-319, 1974.

[58] J.L. Steger and R.L. Sorenson, "Automatic Mesh Point Clustering Near a Boundary in Grid Generation with Elliptic Partial Differential Equations", J. Computational Physics, Vol. 33, 405-410, 1979.

[59] P. Thomas and J. Middlecoff, "Direct Control of the Grid Point Distribution in Meshes Generated by Elliptic Equations", AIAA J., Vol. 18, 652-656, 1980.

[60] R. Barron, "Improvement to Grid Quality and Cost of Multiblock Structured Grid Generation", Proceedings of the 4th Annual Conference of CFD Society of Canada, CFD1996, 303-309, June 1996, Ottawa, Canada.

[61] K.A. Hoffmann and S.T. Chiang, "Computational Fluid Dynamics", Vol. 2, Wichita, KS, 1998.

[62] R. Peyret and D.T. Thomas, "Computational Methods for Fluid Flow", Springer-Verlag, New York, 1983.

[63] K.A. Cliffe, C.P. Jackson and A.C. Greenfield, "Finite Element Solutions for Flow in a Symmetric Channel with a Smooth Expansion", AERE-R, 10608, UK, 1982.

[64] P.J. Roache, "Scaling of High Reynolds Number Weakly Separated Channel Flows", Symposium on Numerical and Physical Aspects of Aerodynamic Flows, Springer-Verlag, 87-98, 1981.

[65] M. Napolitano and P. Orlandi, "Laminar Flow in Complex Geometry: A Comparison", Int. J. for Num. Methods in Fluids, Vol. 5, 667-683, 1985.

[66] P.S. Carson, "Computation of Laminar Viscous Flows Using Von Mises Coordinates", Ph.D. Thesis, University of Windsor, Canada, 1994.

[67] A.K. Rostagi, "Hydrodynamics and Mass Transport in Pipelines Perturbed by Welded Joint", DNV Technical Report No. 82.0152, 1982.

[68] A. Di Carlo, R. Piva and G. Guj, "Computational Schemes in General Curvilinear Coordinates for Navier-Stokes Flows", Notes on Numerical Fluid Mechanics, 2, Vieweg, Braunschweig, p. 36, 1980.

[69] A. Bey, "Two-dimensional Scour Hole Problem: Role of Fluid Structures", Masters Thesis, Department of Civil and Environmental Engineering, University of Windsor, Canada, 2005.

[70] W. Li, "Scour of Fine Sediment by a Turbulent Wall Jet", Ph.D. Thesis, Department of Civil Engineering, Lamar University, USA, 1993.

VITA AUCTORIS

NAME	Bashar Zogheib
PLACE OF BIRTH	Baalback, Lebanon
YEAR OF BIRTH	1975
EDUCATION	Beirut Arab University Beirut, Lebanon B.Sc. Mathematics 1998
	University of Windsor Windsor, Ontario M.Sc. Mathematics 2001
	University of Windsor Windsor, Ontario M.Sc. Statistics 2002
	University of Windsor Windsor, Ontario Ph.D. Mathematics 2006